ELECTRONIC PROPERTIES OF GRAPHITE

Johannes M. Schneider

UNIVERSITÉ DE GRENOBLE

THÈSE

Pour obtenir le grade de

DOCTEUR DE L'UNIVERSITÉ DE GRENOBLE

Spécialité Nanophysique

Arrêté ministériel : 7 août 2006

Présentée et soutenue publiquement par

Johannes SCHNEIDER

le 26 Octobre 2010

PROPRIÉTÉS ÉLECTRONIQUES DU GRAPHITE

Thèse dirigée par **Duncan Maude**

JURY

Thierry Ouisse	Professeur	Président
Kamran Behnia	Directeur de recherche	Rapporteur
Laurence Eaves	Professeur	Rapporteur
Piotr Kossacki	Professeur Associé	Examinateur
Duncan Maude	Directeur de recherche	Examinateur

Thèse préparée au sein du **Laboratoire National des Champs Magnétiques Intenses de Grenoble (LNCMI-GHMFL)** dans **l'Ecole Doctorale de Physique Grenoble**

Constant	Symbol	Value	Unit
elementary charge	e	1.602×10^{-19}	C
electron volts	eV	1.602×10^{-19}	J
		1.160×10^{4}	K
		8.066×10^{3}	cm^{-1}
		2.418×10^{14}	Hz
Planck constant	h	6.623×10^{-34}	Js
		4.136×10^{-15}	eVs
reduced Planck constant	$\hbar$	1.054×10^{-34}	Js
		6.582×10^{-16}	eVs
Boltzmann constant	k_B	1.381×10^{-23}	J/K
		8.617×10^{-5}	eV/K
Bohr magneton	$\mu_B = e\hbar/2m_e$	9.274×10^{-24}	J/T
		5.788×10^{-5}	eV/T
flux quantum	$\phi_0 = h/2e$	2.068×10^{-15}	Vs
speed of light	c	10^{8}	m/s
free electron g-factor	g_s	2.0023	
electron mass	m_e	9.109×10^{-31}	kg

Table 1: *Table of physical constants.*

Symbol	Value	Unit
effective g-factor	g^*	
effective mass	m^*	
quantum lifetime	τ	s
mobility	$\mu = e\tau/m^*$	m^2/Vs
cyclotron frequency	$\omega_c = eB/m^*$	
cyclotron energy	$\hbar\omega_c$	eV *or* J
charge carrier density	n	cm^{-3}
quantum number	N	
Fermi energy	E_F	eV *or* J
Fermi velocity	v_F	m/s
fundamental frequency	B_F	T
SWM-parameters	γ_i, $i = 0-6$	eV

Table 2: *Table of symbols used in this thesis.*

to my 'little'
brother Nils

colored version of the thesis online:
http://tel.archives-ouvertes.fr/tel-00544540/en/

Résumé de la thèse

1. Introduction

Le carbone, qui est certainement un des éléments les plus fascinants, est à la base de toute la chimie organique. Le nombre de ses composés chimiques différents dépasse celui de tous les autres éléments. Le carbone élémentaire a beaucoup de variétés allotropiques différentes avec des propriétés physiques et chimiques toutes aussi variées.

La variété allotropique du carbone élémentaire qui a le plus été étudié est le graphite monocristallin. Les premières études radiographiques de sa structure cristalline réalisées en 1924 par Bernal [1], montrent que le graphite est un matériaux feuilleté tridimensionnel. Les atomes de carbone dans une couche forment un feuillet de réseau hexagonal. Le modèle de la structure de bande du graphite a été élaboré dans les années cinquante par Slonczewski, Weiss et McClure [2, 3]. Leurs calculs sont connus sous le nom de *modèle SWM*.

En 2004, la forme cristallographique bidimensionnelle du carbone – baptisée *le graphène* [4] – a été découverte par Andre Geim et ses collègues à l'université de Manchester [5]. Jusqu'à cette année, il était supposé que le graphène n'existait pas à l'état libre. Toutefois le graphène a été étudié théoriquement depuis plus de soixante ans, car il constitue la base de tous les calculs de structure de bandes des systèmes graphitiques. Les propriétés prometteuses du graphène telles que sa conductivité électronique exceptionnelle et ses propriétés mécaniques remarquables ont déclenché un intérêt grandissant dans le domaine des matériaux à base de carbone. Avec le succès du graphène, sa contrepartie en trois dimensions, le graphite, a suscité un intérêt renouvelé. Du point de vue du graphène, le graphite peut être considéré comme un système quasi bidimensionnel, qui est composé de couches de graphène empilées. Néanmoins le couplage entre les couches mène à une structure de bande strictement tridimensionnelle, c'est-à-dire que la relation de dispersion dans le plan dépend de k_z, où z est la direction verticale au plan.

Des informations sur la structure de bande du graphite peuvent être déduites par l'effet de Haas-van Alphen et l'effet Shubnikov-de Haas. Les deux effets, prédits théoriquement par Landau en 1930 [6], mesurent la variation périodique de l'aimantation et la résistance électrique en fonction du champ magnétique. Une description théorique détaillée de ces deux effets en trois dimensions a été élaboré par Lifshitz et Kosevich pour l'effet de Haas-van Alphen et par Adams et Holstein pour l'effet Shubnikov-de Haas [7, 8].

Pour la surface de Fermi du graphite, calculée dans le modèle SWM, la théorie de Lifshitz et Kosevich prévoit deux oscillations de porteurs majoritaires, c'est-à-dire des électrons massifs provenant du point K ($k_z = 0$) de la zone de Brillouin hexagonale et des trous massifs avec $k_z \approx 0.3$ proches du

point H ($k_z = 0.5$) (Fig. 1). La validité du modèle SWM a été confirmée par diverses expériences effectuées au cours des cinquantes dernières années, par exemple le magnétotransport [9–12], l'effet de Haas-van Alphen [9, 13], la magnétoréflexion [14, 15], l'absorption de micro-ondes et la résonance cyclotron [16, 17], et l'effet Nernst [18]. Néanmoins, grâce aux avancées des systèmes de cryogénie et aux progrès informatiques de nos jours, il parait opportun de revisiter la physique du graphite.

2. Théorie - Propriétés magnétiques du graphite

Le graphite est un matériau feuilleté, avec un espacement d'atomes dans une couche faible (1.42 Å) comparé à l'espacement entre les couches (3.35 Å) [1, 19]. Une première approche vers la compréhension du graphite est donc l'analyse des propriétés d'une couche simple (graphène) et la prise en compte du couplage entre les couches de graphite comme une perturbation. Cette approche a été établie par Wallace en 1947 [20].

2.1 Le graphène

Dans le graphène, les atomes de carbone sont arrangés en nid d'abeille dans le plan. La première zone de Brillouin est donc un hexagone régulier avec deux points caractéristiques K et K' au bord de l'hexagone. L'attrait du graphène est dû à sa structure de bande particulière: Aux points K et K' la bande de conduction et la bande de valence se touchent. Le graphène est donc un semiconducteur à gap nul. De plus, à proximité des points K et K' la structure de bandes des électrons et des trous est linéaire ce qui signifie que les porteurs de charge se comportent comme des fermions relativistes sans masse avec une vitesse de Fermi de l'ordre de $v_F = 3\gamma_0 a_0/2 \approx 1 \times 10^6$ m/s, où γ_0 est le paramètre de couplage entre deux atomes de carbone voisins ($\gamma_0 = 3.2$ eV [21]) et $a_0 = 1.42$ Å est la distance entre eux.

2.1 Le graphite

Dans le graphite les couches du graphène sont empilées verticalement par rapport au plan. L'Hamiltonien qui décrit les bandes d'énergie du graphite a été élaboré par Slonczewski, Weiss et McClure dans les années 1950 [2, 3]. Leurs calculs sont connus sous le nom de *modèle SWM*. Dans le modèle SWM la structure de bande près de l'énergie de Fermi est décrite par sept paramètres, γ_0–γ_5 et $\gamma_6 \equiv \Delta$, qui définissent l'interaction entre les différents atomes de carbone dans le graphite.

La structure de bande du graphite est représentée dans la Fig. 1 b). Les bandes d'énergie sont données en fonction du vecteur d'onde dans la direction z, $k_z(\parallel c)$, entre les points K et H de la zone de Brillouin (Fig. 1 a)). Les quatre bandes sont dénommées E_1, E_2 et E_3 (deux fois dégénérée), respectivement. Le niveau de Fermi se trouve environ au milieu des bandes E_3. De plus, la structure de bande dans le plan est représentée. Au point H le couplage effectif entre les plans est nul, ce qui mène à une structure de bande similaire à celle du graphène, où l'énergie de bande est une fonction linéaire du vecteur d'onde. Au delà du point H, la structure de bande dans le plan est parabolique comme pour des porteurs de charge massifs conventionnels.

La surface de Fermi du graphite le long du bord K-H avec la poche d'électrons au point K et la

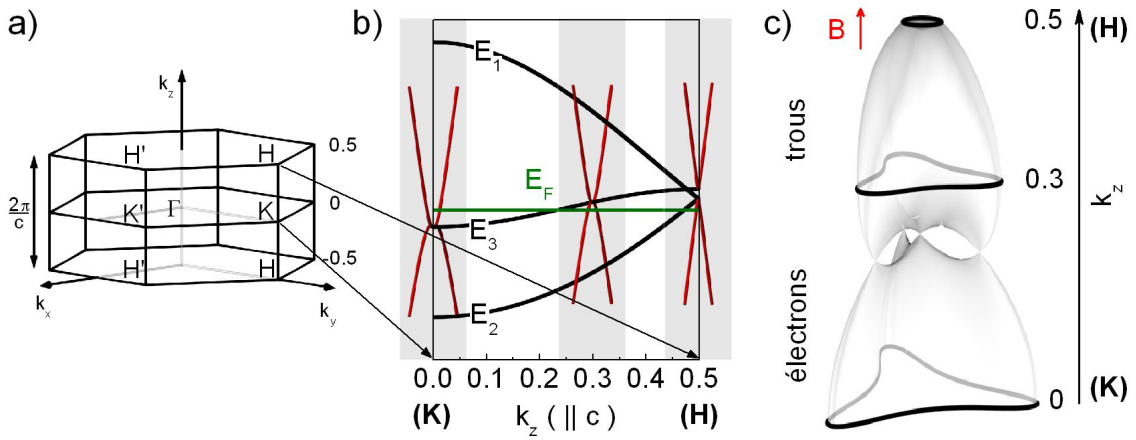

Fig. 1: ***a)*** *Zone de Brillouin du graphite avec ses points caractéristiques* Γ, $K(K')$ *et* $H(H')$. ***b)*** *Structure de bandes du graphite en fonction du moment* k_z *et du moment dans le plan* κ *pour* $k_z = 0,\ 0.3$ *et* 0.5. *Au point H l'énergie de bande est une fonction linéaire de* κ. ***c)*** *Surface de Fermi du graphite avec ses trois zones extrémales à* $k_z = 0,\ 0.3$ *et* 0.5.

poche de trous au point H est représentée dans la Fig. 1 c). Basées sur la surface de Fermi, les propriétés magnétiques du graphite peuvent être qualitativement comprises plus simplement en utilisant l'approximation semi classique, qui relie les zones extrémales de la surface de Fermi au champ magnétique par

$$S_N = \pi k_\perp^2 = (N+\gamma)\frac{2\pi eB}{\hbar}, \tag{1}$$

avec le nombre quantique N et la phase γ. Les porteurs de charge associés aux sections transversales de tailles maximales - dénommés électrons et trous majoritaires - ont des spectres d'énergie paraboliques $E = \hbar^2 k_\perp^2 / 2m^*$ comme on peut le voir dans la Fig. 1 b). Par conséquent le spectre d'énergie quantifiée en champ magnétique de ces porteurs de charge est donné par

$$E = \hbar\omega_c(N+\gamma), \tag{2}$$

avec la fréquence cyclotron $\omega_c = eB/m^*$. La phase γ dépend de la topologie de la structure de bande. Elle a la valeur $1/2$ pour les deux porteurs de charge majoritaires [22].

Le spectre d'énergie des porteurs de charge associés aux sections transversales de petite taille - dénommés les trous minoritaires - dépend linéairement du vecteur d'onde, $E = \pm v_F \hbar |\kappa|$ ce qui signifie

$$E = \pm v_F \sqrt{2\hbar eB(N+\gamma)}, \tag{3}$$

avec $\gamma = 0$ pour les trous minoritaires [22].

Qualitativement la structure de bande du graphite en champ magnétique a été dérivée par McClure [23] et Inoue [24] sur la base du modèle SWM. Pour un vecteur d'onde k_z donné, l'Hamiltonien dépendant du champ magnétique est de taille infinie, mais peut être réduit numériquement à une

taille finie. Dans cette thèse la taille des matrices utilisées est 600×600. L'énergie de bande est modifiée quand le champ magnétique est varié et les extrema locaux des bandes croisent l'énergie de Fermi les un après les autres. Le croisement des extrema locaux avec l'énergie de Fermi mène à l'observation des effets quantiques tels que l'effet Shubnikov-de Haas et l'effet de Haas-van Alphen.

3. Méthodes expérimentales

Deux types d'échantillons de graphite ont été étudiés dans cette thèse: Du graphite HOPG (Highly Oriented Pyrolytic Graphite) et du graphite naturel. Les dimensions des échantillons de HOPG sont de 9 mm $\times$ 2 mm $\times$ 0.5 mm, alors que les échantillons du graphite naturel ne dépassent pas quelques millimètres. L'épaisseur de ces échantillons est dans la gamme submillimétrique. Pour les mesures de magnétotransport des contacts ont été déposés sur ces échantillons en configuration de type "barre de Hall".

Pour les mesures deux systèmes d'aimants différents ont été employés: Deux aimants supraconducteurs avec des champs magnétiques maximaux de $B = 11$ T et $B = 16$ T à la température de l'hélium liquide ($T = 4.2$ K) et un aimant résistif de 20 MW, avec un champ magnétique maximum de $B = 28$ T.

Les mesures ont été effectuées dans trois systèmes cryogéniques différents: Un "anti-cryostat" (ou VTI = Variable Temperature Insert) avec une température de base de $T_b \approx 1.2$ K, un cryostat ^{3}He avec $T_b \approx 300$ mK et deux réfrigérateurs à dilution avec $T_b \approx 10$ mK (aimant supraconducteur) et $T_b \approx 30$ mK (aimant résistif).

Pour les mesures de magnétotransport en configuration de barre de Hall (Fig. 2 a)) un courant alternatif est injecté par les contacts de courants (1-2) aux extrémités de l'échantillon. Le courant dans l'échantillon est limité par une grande résistance de série R_1 ($R_1 = 10$ kΩ – 1 MΩ) beaucoup plus grande que la résistance de l'échantillon. Ceci assure que le courant dans l'échantillon reste approximativement constant (typiquement $I \approx 1$ μA) même si la résistance de l'échantillon varie pendant les mesures. Les chutes de tension longitudinales et transverses U_{xx} et U_{xy} causées par la résistivité de l'échantillon sont mesurées entre les contacts (3-4) et (4-5), respectivement. Les deux signaux sont amplifiés d'un facteur 100 en utilisant des préamplificateurs. Les signaux préamplifiés sont ensuite envoyés à la détection synchrone.

Les mesures de l'effet de Haas-van Alphen ont été effectuées en utilisant la *méthode de couple*. Cette méthode est basée sur le fait que si un échantillon possède une aimantation $\mathbf{M}$ lorsqu'il est exposé à un champ magnétique externe $\mathbf{B}$, un couple $\boldsymbol{\tau}$ est créé dans la direction perpendiculaire à $\mathbf{M}$ et à $\mathbf{B}$,

$$\boldsymbol{\tau} = \mathbf{M} \times \mathbf{B}. \tag{4}$$

Le couple sur l'échantillon a été mesuré en utilisant un couplemètre capacitif. Le montage expérimental principal du couplemètre capacitif est représentée dans la Fig. 2 b). Le condensateur est constitué d'une plaque circulaire avec un diamètre de 2.5 mm assemblée parallèlement à une plaque de cuivre. L'échantillon est monté sur la plaque circulaire avec de la graisse à vide. La

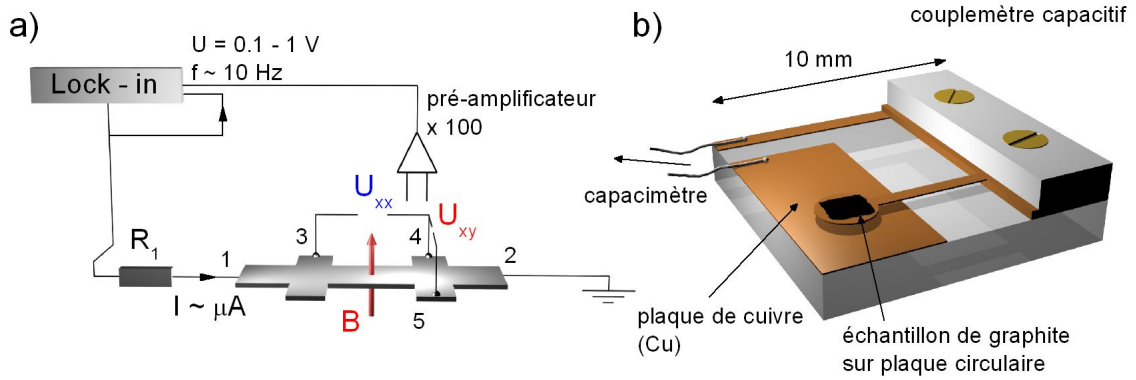

Fig. 2: *Montages expérimentaux pour les mesures de **a)** magnétotransport (barre de Hall) et **b)** l'effet de Haas-van Alphen (couplemètre capacitif).*

plaque circulaire elle-même est reliée par un cantilever effilé à une plaque rectangulaire.

Lorsqu'un champ magnétique est appliqué et l'échantillon est soumis à un couple, le cantilever se comporte comme un ressort. La déformation du ressort mène à un changement de la distance entre le ressort et la plaque de cuivre et par conséquent à un changement de la capacité. La capacité et donc le couple a été mesuré en utilisant un pont de capacité et une technique de détection synchrone standard.

4. Résultats

4.1 Magnétotransport à bas champ - Effets orbitaux

Dans cette thèse nous présentons les premières mesures de magnétotransport du graphite effectuées dans la gamme de température des mK ($T \approx 10$ mK). Le spectre du magnétotransport du graphite naturel mesuré à ces températures est extrêmement riche. Après l'extraction d'un large fond de magnétorésistance (MR), deux séries d'oscillations quantiques superposées peuvent encore être observées à des champs magnétiques très bas ($B_0 \approx 0.07$ T) (voir Fig. 3). Le nombre quantique pour les deux oscillations est proche de $N = 100$ ce qui est nettement plus grand que le nombre $N < 13$ observé dans les expériences précédentes [9]. Le gap Zeeman est observé pour dix structures (flèches), contre trois observés par Woollam [10].

La très grande qualité des données permet l'extraction précise de la phase et de la fréquence des oscillations et la déduction d'informations détaillées sur la topologie de la surface de Fermi du graphite. L'analyse de Fourier des oscillations donne $B_F = 4.75$ T et $B_F = 6.58$ T pour les deux fréquences fondamentales. Dans le modèle SWM les deux fréquences sont assignées aux trous et aux électrons majoritaires. Les valeurs de phase des deux oscillations sont très similaires, la valeur de phase de γ (voir équations (2) et (3)) étant à chaque fois $1/2$. Ces valeurs de phase pour les deux groupes de porteurs sont prédites par le modèle SWM du graphite.

Nous avons confirmé la validité du modèle SWM par des calculs numériques détaillés de la struc-

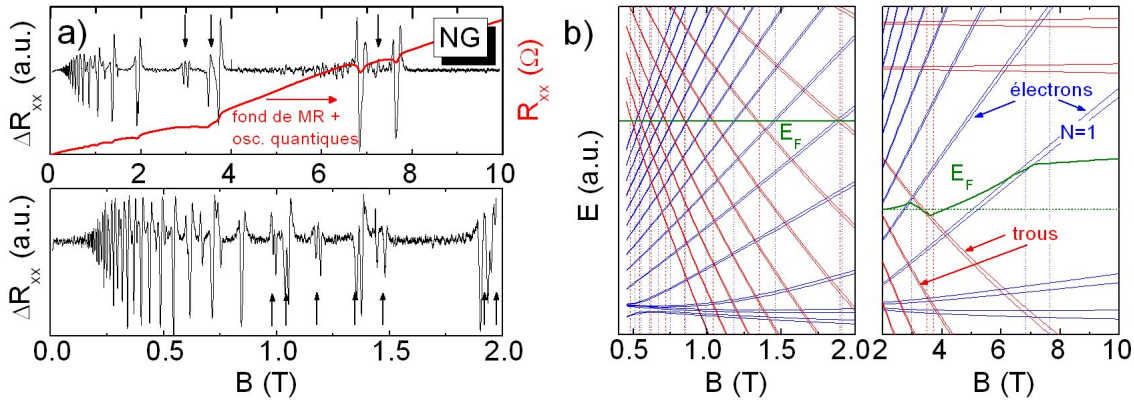

Fig. 3: ***a)*** *Echelle droite: R_{xx} mesurée à $T = 10$ mK en fonction du champ magnétique. Un fond de magnétorésistance (MR) et des oscillations quantiques sont superposés. Echelle gauche: Signal après l'extraction du fond de magnétorésistance, ΔR_{xx}. Les oscillations sont encore observables à très bas champ ($B_0 \approx 0.07$ T). La séparation Zeeman est observée pour dix motifs (flèches).* ***b)*** *Bandes de Landau en fonction du champ magnétique calculées en utilisant le modèle SMW. L'accord entre les calculs et les données (lignes verticales) est remarquable.*

ture de bande. Pour cela nous avons calculé la dépendance des extrema locaux des bandes de Landau (dE/dk_z) en fonction du champ magnétique. Les extrema locaux correspondent aux maxima dans la densité d'états. En conséquence, la conductivité étant proportionnelle à la densité d'états (relation d'Einstein), des motifs dans le magnétotransport sont observés lorsque ces bandes croisent l'énergie de Fermi E_F. Aux champs magnétiques $B < 2$ T, où l'énergie de Fermi peut être considérée comme constante ($\hbar\omega_c \ll E_F$), l'accord entre les calculs et les données (lignes verticales) est remarquable (Fig. 3 b)). Aux champs magnétiques plus élevés l'approximation d'une énergie de Fermi constante n'est plus valable. Si l'énergie de Fermi constante est extrapolée aux champs magnétiques $B > 2$ T, les valeurs du champ magnétique auxquelles les bandes croisent l'énergie de Fermi diffèrent de manière significative de celles observées expérimentalement. Les déviations peuvent être expliquées par un mouvement de l'énergie de Fermi quand on approche la limite quantique. Le mouvement de l'énergie de Fermi a été calculé d'une manière auto-cohérente en supposant que la somme des concentrations des électrons et des trous est constante. Le mouvement de l'énergie de Fermi décale le croisement de l'énergie de Fermi avec les bandes de Landau vers des champs magnétiques plus élevés. Cela est également observé expérimentalement et se manifeste dans l'apériodicité des oscillations en $1/B$ aux champs magnétiques élevés. L'accord entre les calculs et les données est de nouveau remarquable.

La recherche systématique des oscillations de porteurs minoritaires aux faibles champs magnétiques ($B < 0.3$ T) s'est avéré infructueuse. Même si une troisième série d'oscillations est observée pour $B < 0.3$ T, elle ne peut pas être attribuée aux oscillations des porteurs minoritaires, car les oscillations ne sont pas périodiques en $1/B$. Leur origine reste incertaine.

En ce qui concerne le fond de magnétorésistance nous avons effectué quelques mesures en fonction de la température à champ magnétique fixe pour confirmer la transition métal-isolant récemment découverte dans le graphite [25]. Pour des champs magnétiques très faibles ($B \leq 8$ mT), on observe un comportement métallique ($dR/dT > 0$) en fonction de la température entre $T = 1.5$ K et $T = 200$ K. Quand le champ magnétique est augmenté, l'état métallique est supprimé et à $B = 0.131$ T, $R_{xx}(T)$ se comporte comme un isolant ($dR/dT < 0$). Lorsque le champ magnétique est de nouveau augmenté ($B > 0.2$ T), l'état métallique réapparaît. $R_{xx}(T)$ exhibe donc une transition métal-isolant-métal en fonction du champ magnétique.

4.2 Magnétotransport à haut champ - Effet Zeeman

Nous avons effectué des mesures de magnétotransport sur le graphite en champ magnétique intense incliné ($0 < B < 28$ T) pour étudier l'effet Zeeman. Puisque le mouvement orbital des porteurs de charge ne dépend que de la composante perpendiculaire du champ magnétique $B_\perp$, le champ magnétique dans le plan peut être utilisé pour modifier l'énergie de Zeeman $g^*\mu_B B$. g^* est le facteur de Landé effective, μ_B est le magnéton de Bohr et $B = B_\perp/\cos(\theta)$ est le champ magnétique total où θ est l'angle entre le champ magnétique et l'axe normal à l'échantillon.

La séparation des motifs ΔB en fonction du champ magnétique est représentée dans la Fig. 4 b). $\Delta B(B)$ n'est pas une fonction quadratique attendue pour une énergie de Fermi constante. Il s'agit donc d'une preuve expérimentale directe que l'énergie de Fermi n'est pas constante, mais se déplace en fonction du champ magnétique. Le mouvement de l'énergie de Fermi a été discuté précédemment pour expliquer les déviations des motifs orbitaux de la périodicité en $1/B$ aux champs magnétiques $B > 2$ T. Ici nous employons les calculs du mouvement de l'énergie de Fermi pour expliquer le comportement de $\Delta B(B)$. Avec le facteur de Landé effective g^* comme seul paramètre libre dans ce processus, les valeurs de g^* ont pu être extraites pour chaque angle. Le résultat est presenté dans l'encart de la Fig. 4 b). Nous trouvons la valeur $g^* = 2.5 \pm 0.1$ pour $1.5 \leq B \leq 22$ T ce qui est plus grand que la valeur de $g = 2.0023$ pour des électrons libres. La valeur nettement plus grande trouvée ici est attribuée aux interactions multi-corps (interaction d'échange).

4.3 Magnétotransport à haut champ - Onde de densité de charge

Des mesures de magnétotransport du graphite en champ magnétique intense ($0 < B < 28$ T) ont été également employées pour étudier l'onde de densité de charge pour des températures différentes entre $T = 50$ mK et $T = 0.9$ K. L'onde de densité de charge se révèle par une augmentation suivie d'une réduction de la magnétorésistance aux champs magnétiques élevés [26, 27] (voir aussi Fig. 4 c) (flèche)). En accord avec la Réf. [27], le champ magnétique B_{CDW} auquel l'onde de densité de charge apparait diminue à température décroissante. B_{CDW} et la température sont liés par une équation de type Bardeen-Cooper-Schrieffer (BCS)

$$T_c(B) = T^* \exp\left(-\frac{B^*}{B_{\mathrm{CDW}}}\right). \tag{5}$$

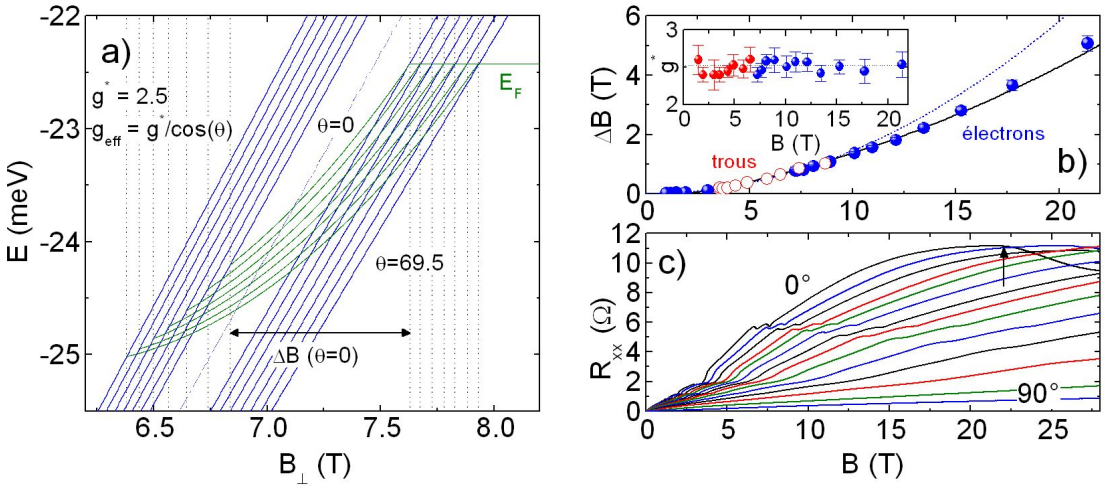

Fig. 4: ***a)*** *Energie de la bande de Landau $N = 1$ (voir Fig. 3 b)) en fonction du champ magnétique perpendiculaire au plan, $B_\perp$, et de l'angle θ. L'angle θ permet de modifier l'énergie de Zeeman $g^*\mu_B B$ avec $g^* = 2.5$. Le mouvement de l'énergie de Fermi a été calculé pour $\theta = 0$ d'une manière auto-cohérente en supposant que la somme des concentrations des électrons et des trous est constante. Pour $\theta > 0$, l'énergie de Fermi a été extrapolée aux champs magnétiques inférieurs.* ***b)*** *Séparation des motifs ΔB en fonction du champ magnétique. La ligne pointillée est attendu théoriquement si l'énergie de Fermi est une constante. La ligne continue correspond aux calculs montrés en a). Encart : Facteur de Landé pour chaque angle calculé dans le modèle SWM en utilisant les données $\Delta B(B)$. $g^* = 2.5 \pm 0.1$.* ***c)*** *R_{xx} en fonction du champ magnétique pour des angles différents ($T \approx 300$ mK). Le champ magnétique auquel l'onde de densité de charge apparait est repéré par une flèche ($\theta = 0$).*

4.4 L'effet de Haas-van Alphen

Enfin nous avons étudié l'effet de Haas-van Alphen dans le graphite à $T = 400$ mK en utilisant la méthode de couple. Par analogie avec des mesures de magnétotransport nous avons effectué quelques mesures de Haas-van Alphen en haute résolution aux champs magnétiques faibles, ce qui est presenté dans la Fig. 5 a) ($dB/dt = 0.002$ T/min, $\theta = 16°$). De même que les oscillations Shubnikov-de Haas dans le magnétotransport, les oscillations de Haas-van Alphen peuvent être mieux observées après l'enlèvement du fond de l'aimantation, ce qui est montre dans la Fig. 5 b) pour $B = 0 - 0.21$ T. Le champ magnétique auquel les oscillations quantiques commencent est $B_0 = 66$ mT ce qui correspond à $B_0 \cdot \cos(\theta) \approx 63$ mT dans la configuration $\theta = 0°$. En ce qui concerne les fréquences et les phases on trouve les valeurs $B_{F,h} = 4.62$ T, $\varphi_{0,h} = -0.56 \pm 0.05$ et $B_{F,e} = 6.32$ T, $\varphi_{0,e} = -0.48 \pm 0.05$.

Nous avons également effectué des mesures en champs magnétiques inclinés ($\theta = 4° - 56°$ et $-3 \leq B \leq 3$ T) pour sonder la surface de Fermi. La limitation aux angles $\theta \geq 4°$ résulte du

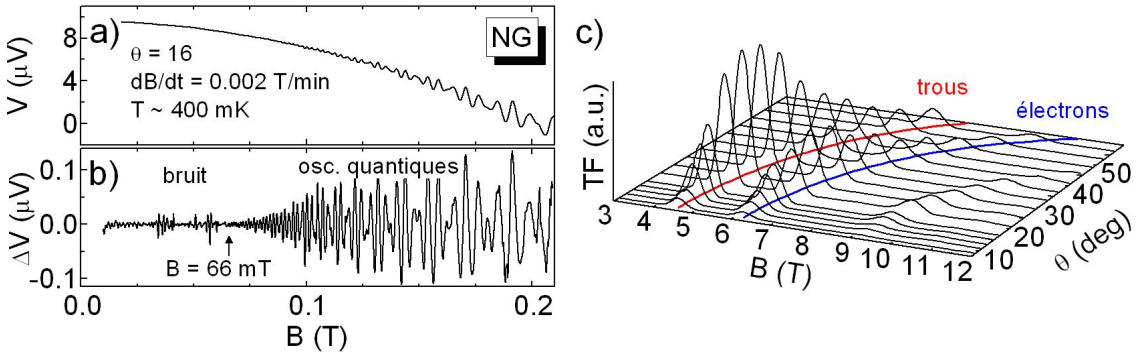

Fig. 5: ***a)*** *Effet de Haas-van Alphen dans le graphite naturel.* ***b)*** *Le signal après l'extraction du fond d'aimantation est similaire à celui du magnétotransport.* ***c)*** *L'intensité spectrale en fonction du champ magnétique et des différents angles pour sonder la surface de Fermi. Le déplacement des motifs en* $1/\cos(\theta)$ *montre que la surface de Fermi du graphite est quasi-bidimensionelle dans les régions des électrons et trous majoritaires.*

fait que le couple sur le cantilever $\boldsymbol{\tau} = \mathbf{M} \times \mathbf{B} = MB \cdot \sin(\theta)$ devient très faible pour des angles petits. La limitation aux angles d'inclinaison $\theta \leq 56^\circ$ est liée à la construction du porte-échantillon prototype, qui ne permettait pas de mesurer des angles plus grands au moment où les mesures ont été effectuées.

La Fig. 5 montre l'intensité spectrale en fonction du champ magnétique pour différents angles. L'augmentation de l'intensité spectrale pour $\theta < 30^\circ$ est liée au fait que le signal de couple est une fonction de $\sin(2\theta)$. La série des trois motifs observés entre $B = 3 - 12$ T (trous, électrons et première harmonique des motifs de trous) se déplace comme $1/cos(\theta)$ vers des champs magnétiques plus élevés (lignes continues dans le plan $B - \theta$). Le comportement quasi-bidimensionel peut être expliqué par l'extrême anisotropie du graphite, le couplage dans le plan étant beaucoup plus grand que le couplage entre les plans ($\rho_c \gg \rho_{ab}$) [28]. Le comportement quasi-bidimensionnel est en accord avec le modèle SWM, qui prédit des surfaces de Fermi quasi-cylindriques pour $\theta < 60^\circ$ dans les régions des électrons et trous majoritaires. Pour des angles plus grands, des écarts à la dépendance $1/\cos(\theta)$ sont attendus. Pour observer cet écart, des mesures de Haas-van Alphen à des angles plus grands sont nécessaires.

Contents

1 Introduction

Résume du chapitre

Le graphite est un matériaux feuilleté tridimensionnel. Les atomes de carbone dans une couche forment un feuillet de réseau hexagonal. Le modèle de la structure de bande du graphite a été élaboré dans les années cinquante par Slonczewski, Weiss et McClure [2, 3]. Leurs calculs sont connus sous le nom de modèle SWM. Des informations sur la structure de bande du graphite peuvent être déduites par l'effet de Haas-van Alphen et l'effet Shubnikov-de Haas. Les deux effets mesurent la variation périodique de l'aimantation et la résistance électrique en fonction du champ magnétique. Une description théorique détaillée de ces deux effets en trois dimensions a été élaboré par Lifshitz et Kosevich pour l'effet de Haas-van Alphen et par Adams et Holstein pour l'effet Shubnikov-de Haas [7, 8].

Pour la surface de Fermi du graphite, calculée dans le modèle SWM, la théorie de Lifshitz et Kosevich prévoit deux oscillations de porteurs majoritaires, c'est-à-dire des électrons massifs provenant du point K ($k_z = 0$) de la zone de Brillouin hexagonale et des trous massifs avec $k_z \approx 0.3$ proches du point H ($k_z = 0.5$). La validité du modèle SWM a été confirmée par diverses expériences effectuées au cours des cinquantes dernières années. Néanmoins, grâce aux avancées des systèmes de cryogénie et aux progrès informatiques de nos jours, il parait opportun de revisiter la physique du graphite.

Carbon, which is certainly one of the most fascinating elements known, forms the basis of all organic chemistry. Its number of different chemical compounds exceeds any other element. Elementary carbon appears as many different allotropes with often very different physical and chemical properties. Graphite for example is soft, an electrical conductor and impervious to visible light (gapless semi-metal), while diamond, the hardest material which exists, is an electrical insulator and transparent to light (wide bandgap).

The allotrope of elementary carbon which has been the most widely studied is mono-crystalline *graphite* (see Fig. 1.1). The first X–ray studies of the crystal structure were made in 1924 by Bernal [1], who showed that graphite is a three-dimensional layered material, with a spacing of atoms within the layer which is small (1.42 Å) compared to the spacing of the lattice planes

(3.35 Å) [1, 19]. The carbon atoms within a layer are arranged in a planar, hexagonal lattice. The band structure model of graphite was elaborated in the 1950s by Slonczewski, Weiss and McClure [2, 3] on the basis of earlier work by Wallace [20] and is referred to as the *SWM-model*.

With the C_{60} molecule, the first so-called *fullerene* was discovered in 1985 [29]. Fullerenes are molecules which are composed entirely of carbon and have the form of hollow spheres, ellipsoids, or tubes. The C_{60} molecule can be viewed as a zero-dimensional structure. The discovery of carbon nanotubes, i.e., one-dimensional fullerenes, was made by Iijima in 1991 [30].

In 2004, the two-dimensional crystallographic form of carbon – baptised *graphene* [4] – was discovered by Andre Geim and co-workers at the university of Manchester [5]. Until that year, it was assumed that graphene does not exist in the free state [31]. Theoretically, however, graphene has been studied for over sixty years, as it is the basis for all band structure calculations of graphite-like systems [20]. Apart from being the first two-dimensional crystal ever discovered, the fact which makes graphene unique is that in the vicinity of the Fermi energy the energy-momentum dispersion relation is linear. This implies a zero effective mass of its charge carriers[1]. Consequently, the quasi particles in graphene are described by the relativistic Dirac equation rather than the Schrödinger equation. The linear energy-momentum dispersion relation results in the unique physical properties of graphene.

With the rise of graphene, its three-dimensional counterpart, graphite, has attracted renewed interest. From the viewpoint of graphene, graphite can be considered as a quasi-two-dimensional system consisting of stacked graphene layers. Nevertheless, the coupling between the layers leads to a band structure of graphite with resolutely three-dimensional origins, i.e., it has a k_z depen-

[1] The general energy momentum relation $E(q) = c\sqrt{q^2 + m^2c^2}$ becomes $E(q) = cq$ for $m = 0$. c is the speed of light, q and m are the momentum and the mass of the particle, respectively.

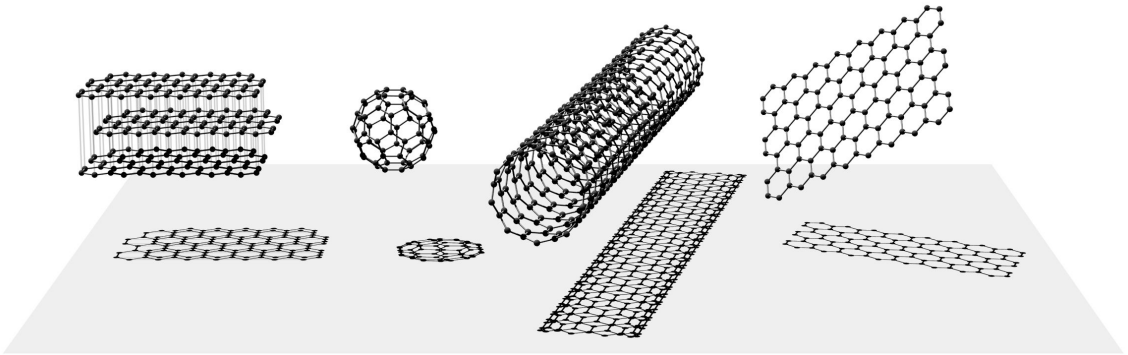

Fig. 1.1: *Graphitic materials in order of their discovery: Graphite, C_{60} molecule (buckminsterfullerene), carbon nanotube and graphene. Graphene, a flat monolayer of carbon atoms packed into a two-dimensional honeycomb lattice, is the basic building block of the other graphitic materials. It can be wrapped up into zero-dimensional fullerenes, rolled into one-dimensional nanotubes or stacked into three-dimensional graphite.*

dent in-plane dispersion relation, with z being the direction perpendicular to the layers. The previously introduced SWM-model predicts that at the K point ($k_z = 0$) of the hexagonal Brillouin zone the inter-plane coupling has a maximum. The coupling results in a "conventional" parabolic dispersion relation of massive charge carriers[2]. At the H point ($k_z = 0.5$) the effective inter-plane coupling is zero, which leads to a graphene-like linear dispersion relation (massless Dirac fermions). A clear signature of Dirac fermions at the H point of graphite has been reported for magnetoreflectance, far-infrared magnetoabsorption and angle-resolved photoemission spectroscopy measurements [15,32,33]. Such measurements probe optical transitions very close to the H and K points.

Other methods to deduce information about the band structure of graphite are for example the de Haas-van Alphen effect and the closely related Shubnikov-de Haas effect. In 1930 Landau predicted that the magnetization of a metal should vary periodically in the inverse magnetic field [6]. The physical principle of the periodic variation is that in the presence of a magnetic field the electronic states of a solid are condensed onto Landau cylinders due to the quantized motion of the charge carriers perpendicular to the magnetic field. When the magnetic field is increased, the Landau cylinders in momentum space grow in diameter and successively cross the Fermi surface, which leads to oscillations of the magnetic field dependent total energy of the electrons and therefore to oscillations in the magnetization and the resistance. A few months after Landau's prediction the periodic behaviour of both the magnetization and the resistance as a function of the inverse magnetic field was indeed observed in a study of bismuth single crystals [34, 35]. It took more than 20 years until Onsager (1952) pointed out the relation between the observed periodicity and the area of an extremal Fermi surface cross section perpendicular to the applied magnetic field [36]. A few years later, in 1956, Lifshitz and Kosevich worked out a detailed theoretical description for isotropic three-dimensional systems, which not only describes the frequency but also the phase and the amplitude of the de Haas-van Alphen oscillations [7]. A similar theory was established by Adams and Holstein (1959) for the Shubnikov-de Haas effect [8].

For the Fermi surface of graphite, calculated within the SWM-model, the Lifshitz Kosevich theory predicts the occurrence of two majority carrier oscillations, i.e., *massive* electrons originating from the K point ($k_z = 0$) and *massive* holes originating from $k_z \approx 0.3$ close to the H point ($k_z = 0.5$). The validity of the SWM-model has been confirmed in various experiments which have been performed over the last fifty years, e.g. magnetotransport [9–12], de Haas–van Alphen oscillations [9, 13], magneto reflection [14, 15], microwave absorption and cyclotron resonance [16, 17], and Nernst effect [18]. The renewed interest in graphite, coupled with advances in cryogenics and computing power, makes it timely to revisit this problem.

This thesis is devoted to the investigation of the electronic properties of *natural graphite* and *Highly Oriented Pyrolytic Graphite* (HOPG) by means of magnetotransport and de Haas-van Alphen measurements. The outline of the thesis is as follows: In Chapter 2 the *free electron gas in*

[2] For massive charge carriers with $mc \gg q$, the general energy dispersion relation becomes $E(q) = q^2/2m$.

magnetic field is discussed. Starting with the quantization of the electron movement in magnetic field as the origin of the de Haas-van Alphen and the Shubnikov-de Haas effect, the most important results of the Lifshitz Kosevich theory will be presented. In Chapter 3 the *electronic and magnetic properties of graphite* are discussed. On the basis of the electronic properties of graphene, the influence of the coupling between the layers on the band structure, described by the SWM-model, is given. From the SWM-model the magnetic properties of graphite can be derived. It will be shown that the magnetotransport properties are dominated by two groups of carriers, electrons and holes. In Chapter 4 the *experimental methods* used in this thesis are presented. The preparation of the different graphite samples for magnetotransport measurements is explained. Then the experimental setup - magnets and cryogenics - are briefly discussed. Finally the measurement techniques for magnetotransport and magnetisation measurements are presented. Chapter 5 deals with *orbital effects in low field magnetotransport*. An essential part of this chapter is the phase/frequency analysis of high quality magnetotransport data measured at mK temperatures. Both parameters are crucial for the understanding of the topology of the Fermi surface. It will be shown by comparing theory and experiment that the SWM-model perfectly predicts the occurrence of the observed features. Moreover, temperature dependent magnetotransport measurements are presented. Chapter 6 is devoted to *spin splitting and the charge density wave (CDW) phase in high field magnetotransport*. Preliminary *de Haas-van Alphen* data measured with a capacitive torquemeter are presented in Chapter 7. It is shown that this data can be used for high precision measurements of the Fermi surface of graphite. In Chapter 8 a *summary* of the main results presented in this thesis is given.

2 Theory - Electron gas in magnetic field

Résume du chapitre

Dans ce chapitre, les propriétés d'un gaz d'électrons dans un champ magnétique sont discutées. Ces propriétés sont à la base de la compréhension du comportement du graphite sous champ magnétique, qui est discuté en détail dans le chapitre suivant. Le traitement en mécanique quantique du gaz d'électrons bidimensionnel dans un champ magnétique montre que les électrons sont confinés dans des niveaux de Landau avec des énergies discrètes. Si le spin des électrons est pris en compte, les spins up et les spins down des électrons d'un niveau de Landau sont séparés énergétiquement. Le spin splitting est décrit par l'énergie Zeeman et – selon le système – l'énergie de couplage spin-orbite et de l'énergie d'échange. Dans un gaz d'électrons tridimensionnel, le mouvement des électrons dans la direction selon k_z n'est pas affecté par le champ magnétique $B\|z$ et les électrons se condensent sur des cylindres de Landau plutôt que sur des niveaux de Landau.
Une extension du modèle de gaz d'électrons libres aux électrons dans un cristal peut être réalisée par des équations quasi-classiques en utilisant la quantification de Bohr-Sommerfeld. Les parties essentielles de ce chapitre sont les descriptions théoriques de l'effet de Haas-van Alphen et de l'effet Shubnikov-de Haas données par Lifshitz et Kosevich et par Adams et Holstein, respectivement [7, 8]. Ces deux effets sondent la quantification des énergies des électrons en champ magnétique et sont des outils efficaces pour obtenir des informations de la surface de Fermi d'un cristal. À la fin du chapitre, l'effet Hall quantique est brièvement discuté.

In this chapter the properties of an electron gas in a magnetic field are discussed. These properties form the basis for the understanding of the magnetic field behaviour of graphite, which is analysed in the subsequent chapter. It is well known that the magnetic field forces charged particles to move on circles (Lorentz force), whose radii diminish for increasing magnetic field. For high magnetic fields[1], i.e., small cyclotron radius of the charge carriers, the wave nature of the electrons has to

[1] $B \gg m_e/e\tau$ with $\omega_c\tau \gg 1$. τ is the quantum lifetime.

be considered. A quantum mechanical treatment of the two-dimensional electron gas (2DEG) in magnetic field shows that the electrons are confined in Landau levels with discrete energies. If the spin of the electrons is taken into account, the spin up and spin down electrons of a given Landau level are energetically separated. The spin splitting is described by the Zeeman energy and – depending on the system – spin orbit coupling and exchange energy. In a three-dimensional electron gas, the electron movement in k_z-direction is not affected by the magnetic field $B \| z$ and the electrons condense onto Landau cylinders rather than Landau levels.
An expansion of the free electron gas model to crystal electrons can be made on the basis of quasi-classical equations using the Bohr-Sommerfeld quantization.
Essential parts of this chapter are the theoretical descriptions of the de Haas-van Alphen and the Shubnikov-de Haas effect given by Lifshitz and Kosevich, and Adams and Holstein, respectively [7, 8]. Both effects probe the quantization of electron energies in magnetic field and are effective tools to caliper the Fermi surface of a crystal.
At the end of the chapter, the quantum Hall effect is briefly discussed.

2.1 The two-dimensional free electron gas in magnetic field

We begin our discussion with the *two-dimensional free electron gas* (2DEG) in magnetic field. When no magnetic field is applied, the electrons are equidistantly spaced in the planar **k** space, separated by $\delta k_x = 2\pi/L_x$ and $\delta k_y = 2\pi/L_y$, as shown in Fig. 2.1 a). L_x and L_y are the sample dimensions. If a magnetic field is applied, the stationary Schrödinger equation reads

$$\frac{1}{2m_e}\left(\frac{\hbar}{i}\boldsymbol{\nabla} - e\mathbf{A}\right)^2 \psi = E\psi \,, \tag{2.1}$$

where $\hbar/i\boldsymbol{\nabla} - e\mathbf{A}$ is the operator of the canonical momentum. $\mathbf{A}$ is the magnetic vector potential, which is $\mathbf{A} = Bx\,\mathbf{u}_y$ for a magnetic field in z-direction (Landau gauge) so that $\mathbf{B} = \boldsymbol{\nabla}\times\mathbf{A} = (0,0,B)$. $\mathbf{u}_y$ is the unit vector in y-direction. In the Landau gauge, the Schrödinger equation reads

$$\frac{\partial^2}{\partial x^2}\psi + \left(\frac{\partial}{\partial y} + \frac{ieB}{\hbar}x\right)^2 \psi + \frac{2m_e E}{\hbar^2}\psi = 0 \,. \tag{2.2}$$

With the ansatz of the form $\psi = \tilde{\psi}(x)e^{-ik_y y}$ the above equation is reduced to the one-dimensional Schrödinger equation of a simple harmonic oscillator,

$$-\frac{\hbar^2}{2m_e}\frac{\partial^2\tilde{\psi}}{\partial x'^2} + \frac{1}{2}m_e\omega_c^2 x'^2\tilde{\psi} = E'\tilde{\psi} \,,$$

where the cyclotron frequency ω_c and the centre of the harmonic oscillator $x_0 = x' - x$ are defined as

$$x_0 = \hbar k_y eB \quad \text{and} \quad \omega_c = \frac{eB}{m_e} \,. \tag{2.3}$$

The eigen energies of the above equation are given by

$$E_N = \hbar\omega_c\left(N + \frac{1}{2}\right) \,, \tag{2.4}$$

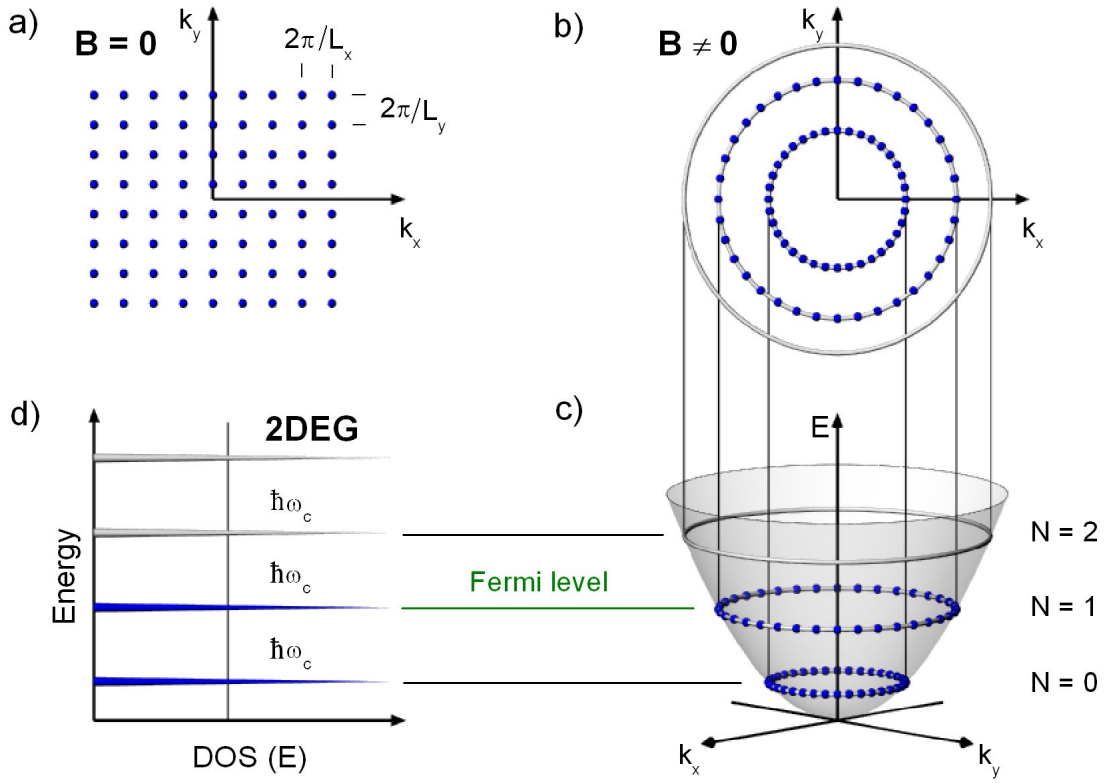

Fig. 2.1: ***a)*** *For $B = 0$ the electrons of a 2DEG are equidistantly spaced in* $\mathbf{k}$ *space, separated by $\delta k_x = 2\pi/L_x$ and $\delta k_y = 2\pi/L_y$. L_x and L_y are the sample dimensions.* ***b)*** *and* ***c)*** *For $B \neq 0$ the motion of two-dimensional charge carriers is confined to discrete circles, which are referred to as Landau levels. The energies of the Landau levels are given by $E = \hbar\omega_c(N + 1/2)$, with N being a non-negative integer number.* ***d)*** *As the charge carriers condense onto Landau levels for $B \neq 0$, the two-dimensional density of states is given by a series of delta functions.*

with $N = 0, 1, 2, \ldots$.

The calculations show that the parabolic band of free electrons ($E = \hbar^2 k^2/2m_e$) splits into sub-bands for $B \neq 0$. The sub-bands are referred to as ***Landau levels***. The electronic states are given by the quantized energies of the circular movement normal to the magnetic field, $E_N = \hbar\omega_c(N + 1/2)$. This is illustrated in the Figs. 2.1 b) and c). The energy eigenvalues differ by the cyclotron energy $\Delta = \hbar\omega_c$. The Landau level with the smallest energy ($N = 0$) is referred to as the *zero Landau level*.

The quantization of the electron movement in magnetic field leads to a considerable change of the two-dimensional electronic density of states. While for $B = 0$, the density of states as a function of the energy is a constant, $m_e/\pi\hbar^2$, it is completely quantized in magnetic field given by a series of delta functions as depicted in Fig. 2.1 d).

2.1.1 Degeneracy of the Landau levels

The degeneracy of the Landau levels corresponds to the number of states per unit area, ζ, in each Landau level. In a sample with the dimensions L_x and L_y the quantization of the wave vectors k_i due to the boundary conditions is given by $\delta k_i = 2\pi/L_i$. The variable x (Eq. (2.3)) of the field dependent Schrödinger equation has to fulfil the condition $0 < x(k_y) < L_x$. Under the assumption that the centres of the Landau levels are far from the edges of the sample, k_y is given by

$$k_y \leq \frac{eB}{\hbar} L_x = \frac{m_e \omega_c}{\hbar} L_x \, .$$

If we neglect spin splitting, each state is occupied by both a spin up and a spin down electron. The number of states per unit area in a given Landau level equals

$$\zeta = 2\frac{1}{L_x L_y}\frac{k_y}{\delta k_y} = \frac{2eB}{h} = \frac{B}{\Phi_0} \, , \tag{2.5}$$

with the flux quantum $\Phi_0 = h/2e$. The degeneracy is a linear function of the magnetic field, i.e., the number of electrons in a given Landau level N increases linearly with the magnetic field.

2.1.2 Electron energy and Fermi energy movement of a two-dimensional system

With the linear magnetic field dependence of the number of states in a Landau level, $\zeta = 2eB/h$, all charge carriers are in the $N = 0$ Landau level at $B > hn/2e$, where n is the total number of electrons in the system. At zero temperature the Fermi energy is therefore given by $E_F = \hbar\omega_c/2$.

When the magnetic field is decreased, the degeneracy of the zero Landau level decreases so that the level is increasingly populated. At the magnetic field $B_F = hn/2e$, the Landau level $N = 0$ is

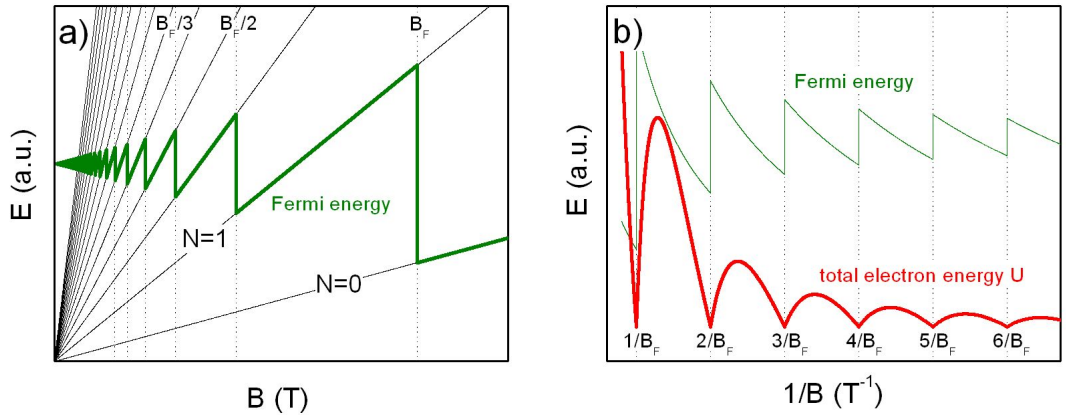

Fig. 2.2: ***a)*** *Landau level energies of a 2DEG in arbitrary units as a function of the magnetic field. Due to the degeneracy $\zeta = 2eB/h$ of the Landau levels the Fermi energy jumps at $B_F/(N+1)$ from the level N to the level $N+1$. $B_F = hn/2e$ depends on the total number of electrons n in the system.* ***b)*** *Total electron energy U as a function of the inverse magnetic field.*

fully populated. When the magnetic field is further decreased, the Landau level $N = 1$ is filled and the Fermi level jumps to $E_F = 3/2\hbar\omega_c$. This behaviour is repeated when going to lower and lower magnetic fields, i.e., the Fermi energy jumps at $B_F/(N+1)$ with $N = 0, 1, 2, \ldots$ to the next level. The diagrams in Fig. 2.2 a) (fan-chart) and b) show the evolution of the Fermi energy as a function of the magnetic field and the inverse magnetic field, respectively. The jumps of the Fermi energy are periodic in $1/B$.

The linear dependence of the number of electrons in a Landau level on the magnetic field leads to a periodic variation of the total electron energy U as demonstrated in the following. For $B > B_F$ all electrons n are in the $N = 0$ Landau level so that the total electron energy is given by $n\hbar\omega_c/2$. For $B_F/2 < B < B_F$, $\zeta = 2eB/h$ electrons are in the $N = 0$ Landau level and $n - \zeta$ electrons are in the $N = 1$ Landau level, i.e., $U = \zeta\hbar\omega_c/2 + (n-\zeta)\hbar\omega_c 3/2$. If this procedure is repeated for lower magnetic fields, one finds

$$U = \hbar\omega_c \left[\zeta \frac{M^2}{2} + (n - M\zeta)\,(M + \frac{1}{2})\right], \tag{2.6}$$

where $M = \lfloor B_F/B \rfloor$, with $\lfloor B_F/B \rfloor$ being the floor function which rounds the element B_F/B to the nearest integer less than or equal to B_F/B. Eq. (2.6) can be rewritten as

$$U = \hbar\omega_c \left[n\left(M + \frac{1}{2}\right) - \frac{eB}{4h} M\,(M+1)\right]. \tag{2.7}$$

The total electron energy U is periodic in $1/B$, as shown in Fig. 2.2 b).

The oscillatory period $\Delta(1/B)$ can be linked to the Landau level surface S_N in the k_x-k_y plane, $S_N = \pi k_{\perp,N}^2$, where $k_{\perp,N}^2$ is the radius of the Landau levels. $k_{\perp,N}^2$ can be found by rewriting the energies of the electron states as

$$E = \frac{\hbar^2}{2m_e} k_{\perp,N}^2. \tag{2.8}$$

For $B \neq 0$ this energy must be equal to the quantized electron energy, $E_N = \hbar\omega_c(N + 1/2)$, so that

$$k_{\perp,N} = \sqrt{\frac{2eB}{\hbar}\left(N + \frac{1}{2}\right)}. \tag{2.9}$$

The surface between two consecutive Landau levels is therefore

$$\Delta S = S_{N+1} - S_N = \pi k_{\perp,N+1}^2 - \pi k_{\perp,N}^2 = \frac{2\pi eB}{\hbar}, \tag{2.10}$$

i.e., for a given magnetic field ΔS is constant. As

$$\Delta\frac{1}{B} = \frac{2\pi e}{\hbar S}, \tag{2.11}$$

the cross section of the Landau level surface perpendicular to the applied magnetic field can be mapped out by measuring the period $\Delta(1/B)$ of quantum oscillations.

2.1.3 Spin effects

Until now the intrinsic angular momentum of the electrons, the spin, has been neglected as far as the electron energy is concerned. Electrons with different spin quantum numbers $S = \pm 1/2$ were assumed to have identical energies. However, an external magnetic field leads to a lifting of the spin degeneracy, as the spins interact with the external magnetic field. This effect is referred to as the *(normal) Zeeman effect*. The energy corrections to the free electron Hamiltonian (2.1) are given by the Zeeman terms

$$\Delta E_{Z,\downarrow} = -\frac{1}{2} g_s \mu_B B \quad \text{and} \quad \Delta E_{Z,\uparrow} = \frac{1}{2} g_s \mu_B B$$

for electrons with spin $S = -1/2$ ($\downarrow$) and $S = +1/2$ ($\uparrow$), respectively. $g_s = 2.0023$ is the free electron g-factor, μ_B is the Bohr magneton and B is the external magnetic field.

In a crystal, the energy difference of two electrons with opposite spins can be different than the free electron Zeeman energy $\Delta E_Z = g_s \mu_B B$. This difference can be explained by *spin orbit* and *exchange interaction* effects.

Spin orbit coupling describes interaction of a particle's spin with its motion. The interaction is described by the spin orbit Hamiltonian,

$$\mathbf{H_{SO}} = \frac{\hbar}{4 m_e^2 c^2} (\nabla \mathbf{V} \times \mathbf{p}) \cdot \boldsymbol{\sigma},$$

where $\boldsymbol{\sigma}$ are the Pauli matrices and $\mathbf{L} = \hbar / 4 m^2 c^2 (\nabla \mathbf{V} \times \mathbf{p})$ transforms as the angular momentum. A proper derivation of the spin orbit Hamiltonian requires a relativistic treatment of the electron motion. Qualitatively the spin orbit interaction can be explained in the following way. We consider that an electron moves due to an external electric field in an environment containing electrostatic charges. In a 2DEG, the electrostatic charges are the other electrons. In the referential of the electron, the electron itself does not move but the charge carriers around it. The movement of the charge carriers can be translated into an effective magnetic field, which interacts with the spin of the electron. In graphite the spin orbit coupling is quite small, leading to a correction of the free electron Zeeman energy of about 5% [37, 38].

A third correction to the spin splitting may arise from the repulsive Coulomb interaction between electrons in a 2DEG. It was shown in Refs. [39] and [40] that if the numbers of electrons with spin up $n_\uparrow$ and spin down $n_\downarrow$ are different from each other, the many body Coulomb interaction gives rise to the following energy correction,

$$\Delta_s = \frac{n_\uparrow - n_\downarrow}{n_\uparrow + n_\downarrow} \frac{e^2}{\varepsilon \ell_B}. \tag{2.12}$$

$(n_\uparrow - n_\downarrow)/(n_\uparrow + n_\downarrow)$ is the spin polarization, $\ell_B = \sqrt{\hbar / eB}$ is the magnetic length and ε is the dielectric function.

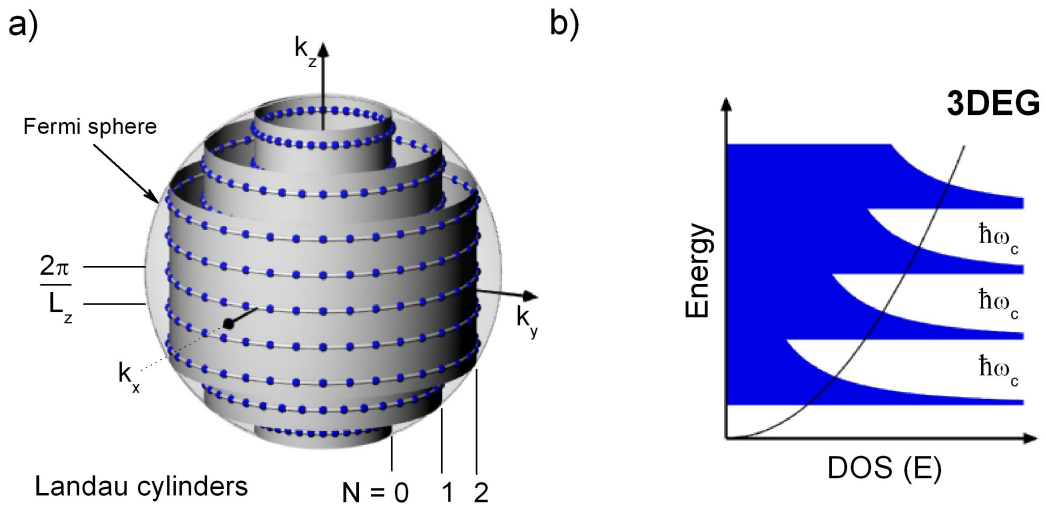

Fig. 2.3: ***a)*** *In a three-dimensional electron gas, the electrons are confined in Landau cylinders for $B \neq 0$. Only states within the Fermi sphere are occupied.* ***b)*** *The density of states of a three-dimensional electron gas in magnetic field is given by a combination of delta functions (2DEG in the k_x–k_y-plane) with the $1/\sqrt{E}$ dependence of a one-dimensional electron gas (k_z-direction).*

2.2 The three-dimensional free electron gas in magnetic field

2.2.1 Landau cylinders

We now discuss what happens when we add the third dimension, z, and go from a two-dimensional to a three-dimensional electron gas. Adding the z-direction, the Hamiltonian (2.2) reads

$$\frac{\partial^2}{\partial x^2}\psi + \left(\frac{\partial}{\partial y} + \frac{ieB}{\hbar}x\right)^2 \psi + \frac{\partial^2}{\partial z^2}\psi + \frac{2m_e E}{\hbar^2}\psi = 0\,.$$

With $\psi = \tilde{\psi}(x)e^{-i[k_y y + k_z z]}$, the additional term $(\partial^2/\partial^2 z)\psi$ leads to the modified eigen energy term

$$E_N = \hbar\omega_c\left(N + \frac{1}{2}\right) + \frac{\hbar^2}{2m_e}k_z^2\,. \tag{2.13}$$

The electronic states are therefore given by the sum of the quantized energy of the circular movement normal to the magnetic field, $E_N = \hbar\omega_c(N + 1/2)$, and the translation energy of the free electron movement in the direction of the field z, $E_z = \hbar^2 k_z^2/2m_e$. With the electron movement in k_z-direction not being affected by the magnetic field $B\|z$, the electrons condense onto *Landau cylinders*, which is depicted in Fig. 2.3 a). Only states within the Fermi sphere are occupied.

2.2.2 Density of states

For $B = 0$, the densities of states of a one-dimensional, a two-dimensional and a three-dimensional electron gas are proportional to $1/\sqrt{E}$, constant and proportional to $\sqrt{E}$, respectively. The quanti-

zation of the electron movement in magnetic field leads to a considerable change of the electronic density of states. We have seen previously that the density of states of a 2DEG is completely quantized in magnetic field, given by a series of delta functions, as depicted in Fig. 2.1 d). For a three-dimensional electron gas, the movement of the electrons in the field direction has to be taken into account. As shown in Fig. 2.3 b), the three-dimensional density of states in magnetic field is given by the superposition of the quantized density of states of a two-dimensional system perpendicular to the field direction with that of a one-dimensional system parallel to the field direction. The density of states is therefore described by the combination of the delta function series of the 2DEG with the $1/\sqrt{E}$ dependence of a one-dimensional electron gas.

2.3 Crystal electrons

An expansion of the free electron gas model to the general case of electrons in a crystal would be quite complicated as we would have to establish similar calculations to those discussed previously, which additionally take into account the interaction of the electrons with the crystal ions. Onsager, however, showed that the behaviour of crystal electrons can be described by quasi-classical equations, based on the Bohr-Sommerfeld quantization [36],

$$\oint \mathbf{p} \cdot d\mathbf{r} = 2\pi\hbar(N+\gamma), \tag{2.14}$$

where N is a non-negative integer number. γ is a phase term, which has the value $\gamma = 1/2$ for the harmonic oscillator. Integrating the canonical momentum $\mathbf{p} = \hbar\mathbf{k} + e\mathbf{A}$, using the semi classical equation

$$\hbar\frac{d\mathbf{k}}{dt} = e\frac{d\mathbf{r}}{dt} \times \mathbf{B},$$

one obtains the so-called *Lifshitz-Onsager* formula

$$S_N = \frac{2\pi eB}{\hbar}(N+\gamma). \tag{2.15}$$

This formula relates the surface, which is enclosed by the electron movement in $\mathbf{k}$ space, S_N, to the strength of the magnetic field B and the quantum number N. In a crystal S_N corresponds to the Fermi surface cross section area in the plane perpendicular to the magnetic field.

The difference between two consecutive surfaces is

$$\Delta S = S_{N+1} - S_N = \frac{2\pi eB}{\hbar}. \tag{2.16}$$

Concerning the quantization of the cross section surfaces S_N, the same result as for free electrons is obtained (Eq. (2.10)). The result, however, is not only valid for circular orbits as in the case of free electrons, but as well for non circular Landau orbits. The effect of the magnetic field is

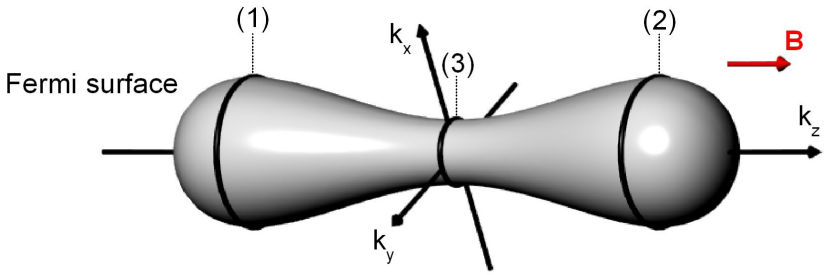

Fig. 2.4: *Illustration of the Fermi surface extremal orbits which contribute to the oscillatory behaviour of a signal. For the magnetic field directed along the k_z-axis, (1) and (2) are maximum extremal orbits and (3) is a minimum extremal orbit.*

that the electrons, which at $B = 0$ are equidistantly distributed in the Fermi body, now move on concentric Landau orbits perpendicular to the direction of the magnetic field.

For a three-dimensional Fermi surface, there exists an infinite number of cross sections perpendicular to the direction of the magnetic field. Those cross sections have different surface areas and therefore lead to different periodicities. One can show, however, that only extremal orbits contribute to the oscillatory behaviour of a signal [41]. This can be illustrated by the fact that for non-extremal orbits the orbital period and therefore the phase factors of neighbouring orbits are different so that their contributions to the signal are cancelled out by interference. Only in the vicinity of extremal orbits, the orbital periods and the phase factors remain constant. An illustration of extremal orbits of a Fermi surface which contribute to the oscillatory behaviour of a signal is given in Fig. 2.4.

2.4 de Haas-van Alphen and Shubnikov-de Haas effect

The free electron picture allows a qualitative understanding of the Shubnikov-de Haas effect and the de Haas-van Alphen effect, which describe the behaviour of the conductivity along the direction of the current and the magnetization of a sample, respectively. A detailed theoretical description for crystal electrons is given by *Lifshitz and Kosevich* [7] for the de Haas-van Alphen effect and by *Adams and Holstein* [8] for the Shubnikov-de Haas effect.

2.4.1 de Haas-van Alphen effect

In Section 2.1.2 it was shown that the total energy U of a free electron gas is a periodic function of the inverse magnetic field $1/B$. The magnetization of a sample is given by

$$M = -\frac{1}{V}\left(\frac{\partial F}{\partial B}\right)_{T,V} \tag{2.17}$$

with the free energy $F = U - TS$, where S is the entropy. As $F = U$ for $T = 0$, the magnetization is as well a periodic function of $1/B$. The oscillations of the magnetization as a function of the (inverse) magnetic field are referred to as the de Haas-van Alphen effect.

A detailed theoretical description of the de Haas-van Alphen effect is given by Lifshitz and Kosevich [7]. The starting point of the calculations is the thermodynamic potential $\Omega = F - N \cdot E_F$ rather than the free energy. The thermodynamic potential is linked to the magnetization by

$$\mathbf{M} = -\left.\frac{\partial \Omega}{\partial \mathbf{B}}\right|_{\mu}, \tag{2.18}$$

where the chemical potential μ (equal to the Fermi energy for $T = 0$) is kept constant.

For a system obeying the Fermi-Dirac statistic and having discrete states of energy E_N, the thermodynamic potential gives the expression

$$\Omega = -k_B T \sum_N \ln\left[1 + \exp\left(\frac{\mu - E_N}{k_B T}\right)\right]. \tag{2.19}$$

k_B is the Boltzmann constant and T is the temperature of the system. To carry out the summation of the thermodynamic potential, only a two-dimensional projection of the $\mathbf{k}$ space perpendicular to the magnetic field is considered in a first step. The summation is performed taking the degeneracy of the Landau levels into account. When going from two to three dimensions in $\mathbf{k}$ space, the states in the out of plane direction have to be considered. As discussed in Section 2.3 only extremal Fermi surface cross sections give rise to the measured signal, as the contributions of the other parts of the Fermi surface interfere destructively and thus cancel each other. The oscillatory part of the magnetization, known as the *Lifshitz-Kosevich formula* reads

$$M_{osc}^{\parallel} = -\sqrt{\frac{e^5}{2\pi^5\hbar}}\frac{B_F\sqrt{B}}{m^* m_e\sqrt{\left|S''_{extr}\right|}} \cdot \sum_{p=1}^{\infty}\frac{1}{p^{3/2}} R_T(p) R_D(p) R_s(p) \sin\left[2\pi p\left(\frac{B_F}{B} - \gamma + \delta\right)\right] \tag{2.20}$$

for the magnetization parallel to the magnetic field and

$$M_{osc}^{\perp} = -\frac{1}{F}\frac{dF}{d\theta} \cdot M_{osc}^{\parallel} \tag{2.21}$$

for the magnetization perpendicular to the magnetic field.

m^* is the effective cyclotron mass, S''_{extr} is the second derivative of the Fermi surface cross section with respect to the k component parallel to the magnetic field. p is an integer number. $B_F = \Delta(1/B)$ is the fundamental frequency of the oscillations. The phase factor δ reflects the curvature of the Fermi surface in z-direction. It has the value $\delta = \pm 1/8$ for a three-dimensional corrugated Fermi surface. The plus and minus signs correspond to minimum and maximum cross sections, respectively (see Fig. 2.4). For a cylindrical Fermi surface it has the value $\delta = 0$. The indexed factors R are amplitude factors, which are briefly explained in the following.

The temperature factor R_T takes the effect of a finite temperature into account. $T \neq 0$ leads to a smearing out of the electronic energy distribution, described by the Fermi-Dirac distribution function

$$f(E) = \frac{1}{1 + \exp\left(\frac{E-\mu}{k_B T}\right)}.$$

The thermal broadening of the electronic distribution function gives rise to contributions, which do not originate from electrons at the exact Fermi energy. The temperature factor reads

$$R_T(p) = \frac{\alpha \frac{m^*}{m_e}\frac{T}{B}}{\sinh\left(\alpha p \frac{m^*}{m_e}\frac{T}{B}\right)} \quad \text{with} \quad \alpha = \frac{2\pi^2 k_B m_e}{\hbar e}. \tag{2.22}$$

The factors R_D and R_S are referred to as Dingle factor and spin factor, respectively. The Dingle factor describes the effect of electron scattering, leading to a broadening of the otherwise sharp Landau levels, which is described by the quantum lifetime τ. The Dingle factor reads

$$R_D(p) = \exp\left(-\alpha p \frac{m^* T_D(\tau)}{m_e B}\right) \quad \text{with} \quad T_D = \frac{\hbar}{2\pi k_B \tau}. \tag{2.23}$$

T_D has the dimension of a temperature and is referred to as *Dingle temperature*.

The spin factor describes the effect of Zeeman splitting, i.e., each Landau cylinder is split into two sets of cylinders separated by the energy $g^*\mu_B B$. Thus, instead of one Landau cylinder passing through the Fermi surface, two sets of levels consecutively cross the Fermi surface. This gives rise to an additional phase factor, which leads to the spin factor

$$R_S(p) = \cos\left(\frac{\pi}{2} p g \frac{m^*}{m_e}\right). \tag{2.24}$$

For a more detailed discussion of those factors, the reader is referred to Ref. [42].

The Lifshitz-Kosevich formula (2.20) has been remarkably successful in describing the observed properties of normal metals and semimetals. Together with band structure calculations it allows the reconstruction of the Fermi surface by investigating the phase/frequency spectrum as a function

of the crystallographic orientation. The effective mass m^* of the charge carriers can be extracted from the temperature dependence of the oscillation amplitude at a given magnetic field by fitting the data using the thermal damping factor. With the knowledge of m^*, a plot of

$$\ln\left[A \times \sinh\left(\alpha \frac{m^* T}{B}\right) B^{-\frac{1}{2}} T^{-1}\right] \tag{2.25}$$

vs. $1/B$, with A being the amplitude of the oscillations, provides information about the Dingle temperature T_D and therefore the quantum lifetime τ. This kind of plot is referred to as *Dingle plot*.

2.4.2 Shubnikov-de Haas effect

The appearance of oscillatory effects in the electrical conductivity or resistivity due to Landau level quantization is referred to as the Shubnikov-de Haas effect [35]. Contrary to the de Haas-van Alphen effect, which is a pure thermodynamic effect, the Shubnikov-de Haas effect is a transport property. It can be understood qualitatively by the following argument [43]. The probability for an electron to be scattered is proportional to the number of states into which it can be scattered. The number of accessible states varies with the magnetic field. It is given by the convolution of the density of states as a function of the energy and the Fermi-Dirac distribution. Thus, the number of states and therefore the scattering is greatly increased when a Landau band crosses the Fermi surface. On the other hand, if there are no Landau states at the Fermi surface, the number of available states for scattering is low.
As scattering is the main origin for electrical resistivity (or conductivity), it is affected by the change of the scattering probability. With the scattering probability oscillating with a frequency of B_F in $1/B$, the resistivity is expected to follow the same oscillatory behaviour.

A quantitative discussion of the scattering processes is given by Adams and Holstein [8]. The total conductivity as a function of the magnetic field is given by the sum of the classical conductivity $\sigma_0(B)$ and two quantum correction terms $\Delta\sigma_1(B)\sigma_0(B)$ and $\Delta\sigma_2(B)\sigma_0(B)$ containing the oscillatory contributions,

$$\sigma_{xx}(B) = \sigma_0(B)\left[1 + \Delta\sigma_1(B) + \Delta\sigma_2(B)\right]. \tag{2.26}$$

The term $\Delta\sigma_1(B)$ describes scattering from the highest occupied Landau level at the Fermi surface to levels above the Fermi surface, and is referred to as *inter–level scattering*. The term $\Delta\sigma_2(B)$ describes scattering within the highest occupied Landau level, so-called *intra–level scattering*. Far away from the quantum limit $B_F/B \gg 1$ the effect of the intra-level scattering term is much smaller than the inter-level scattering term and is therefore usually neglected.

The oscillatory part of the conductivity can be written in a form analogous to the Lifshitz-Kosevich formula (2.20),

$$\frac{\Delta\sigma_{osc}}{\sigma_0} = \frac{5}{2}\sqrt{\frac{\pi e\hbar B}{E_F m^* \left|S''_{extr}\right|}} \cdot \sum_{p=1}^{\infty} \frac{1}{p^{1/2}} R_T(p) R_D(p) R_s(p) \cos\left[2\pi p\left(\frac{B_F}{B} - \gamma + \delta\right)\right]. \tag{2.27}$$

σ_0 is the conductivity measured at zero magnetic field. Note the phase shift of $\pi/2$ between the de Haas-van Alphen and the Shubnikov-de Haas oscillations.

2.5 The quantum Hall effect

The quantum Hall effect occurs in two-dimensional systems. It manifests itself by plateau like features in the transverse resistance $R_{xy}(B)$, i.e., the resistance perpendicular to the direction of the current and the magnetic field (see Fig. 4.2). If spin splitting is not resolved, the quantized resistivity of the plateaus is given by,

$$\rho_{xy} = \frac{1}{N+1} \cdot \frac{h}{e^2} , \quad N = 0,1,2,\ldots \tag{2.28}$$

which can be derived by replacing the charge carrier density n in the classical Hall resistivity $\rho_{xy} = B/ne$ (Eq. (A.3) in the Appendix) by $n = (N+1)\xi = (N+1)eB/h$ (spin splitting resolved). Contrary to the classical Hall resistance, which depends on the charge carrier density of the sample, the quantized resistance is independent of the sample properties.

To understand the quantum Hall effect, we first discuss the electrostatic potential in y-direction, $V(y)$. Basic considerations show that at the centre of the sample, the electrostatic potential is nearly constant. At the edges of the sample, however, the potential diverges, as the quantum mechanical wave functions must vanish in this region [44]. Hence, a simple model of the electrostatic potential

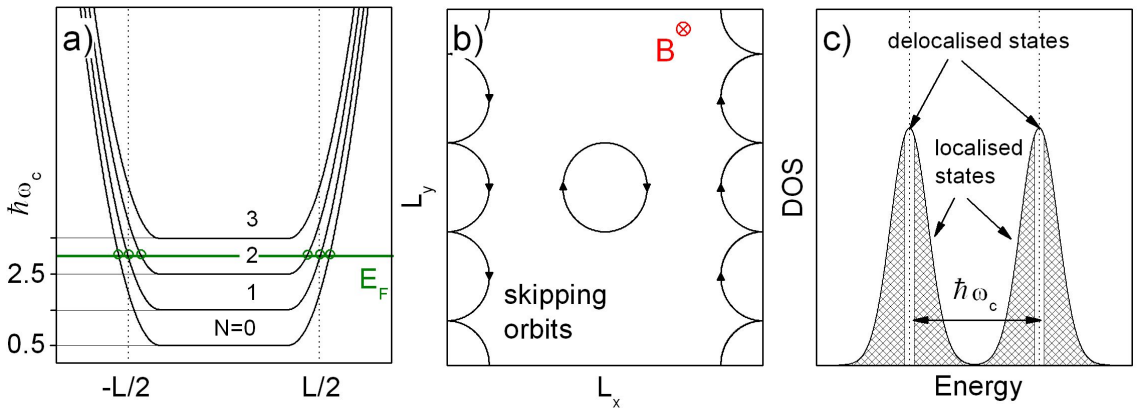

Fig. 2.5: ***a)*** *Landau level energies in a two-dimensional sample, which diverge at the edges of the sample. This leads to the formation of ballistic edge current states.* ***b)*** *Classically, the edge current states correspond to skipping orbits along the edges of the sample, at which the electrons are reflected.* ***c)*** *The existence of localized and delocalized states in the density of states (DOS) is crucial for the explanation of the quantum Hall effect.*

is given by a quantum well,

$$\mathrm{V(y)} = \begin{cases} 0 & y \in (-L_y/2, L_y/2) \\ +\infty & \text{else} \end{cases} .$$

In this model, the energies of the Landau levels at the centre of the sample are given by $E_N = \hbar\omega_c(N+1/2)$. The confinement potential results in a divergence of the Landau level eigen energies at the edges of the sample. Fig. 2.5 a) shows this behaviour as a function of the width of the sample.

Impurities in the sample lead to a broadening of the Landau levels, as charge carries can scatter inelastically at these impurities. An inelastic scattering mechanism means that the Landau quantization energy is not sharply defined, and the energies of the states can be different than $E_N = \hbar\omega_c(N+1/2)$. Aoki and Kamimura [45] proposed the existence of Anderson-localized and delocalized states in the density of states, as displayed in Fig. 2.5 c). According to their theory, the delocalized states are found in the vicinity of the Landau level quantization energy. The delocalized states are unbound and can therefore contribute to the conductivity. The localized states lie in the tails of the density of states. They do not contribute to the electronic transport.

As the Fermi energy for a given magnetic field is constant, there are for $B < B_F$ always some free electron states at the edges of the sample, where the Landau levels cross the Fermi energy (circles in Fig. 2.5 a)). These free electron states, called *edge states*, allow electronic transport even if the Fermi energy does not lie in the centre of the Landau level. Classically, they correspond to skipping orbits along the edges of the sample, at which the electrons are reflected (Fig. 2.5 b)). Electrical conduction is therefore possible by electronic transport through these channels. The number of the transport channels depends on the number of occupied Landau levels and therefore on the magnetic field.

With the picture of the edge states, it is possible to describe the electrical transport within the *Landauer-Büttiker* formalism, which supposes a ballistic transport mechanism in the transport channels. In the Landauer Büttiker formalism, the electric current through transport channels is given by

$$I_i = \frac{2e}{h}\left[(N_i - R_i)\mu_i - \sum_{j\neq i} T_{ij}\mu_j\right] . \tag{2.29}$$

μ_i is the chemical potential of a contact, R_i the reflection coefficient of the channel i and T_{ij} is the transmission coefficient from the channel i to the channel j. For ideal contacts, R_i is zero and $T_{ij} = 1$. Applying this formalism to the Hall bar configuration (Fig. 4.2), the result of Eq. (2.28) is obtained. The Landauer Büttiker formalism gives a possible explanation for the appearance of the Landau plateaus. If the Fermi energy is in the localized states of the Landau levels, only the transport channels contribute to the current. As the electronic transport through the transport channels is ballistic, the resistance remains constant when the magnetic field is changed. If the Fermi energy equals the energy of the delocalised states of a Landau level, the delocalised charge carriers contribute to the current. This is a diffusive transport mechanism and the resistance changes.

3 Theory - Electronic and magnetic properties of graphite

Résume du chapitre

Dans ce chapitre, les propriétés électroniques et magnétiques du graphite sont discutées. Le graphite étant un matériau feuilleté très anisotrope, une première approche vers la compréhension du graphite est l'analyse des propriétés d'une couche simple (graphène) et la prise en compte du couplage entre les couches de graphite comme une perturbation. Cette approche a été établie par Wallace en 1947 [20]. L'Hamiltonien qui décrit les bandes d'énergie du graphite a été élaboré par Slonczewski, Weiss et McClure dans les années 1950 [2,3]. Leurs calculs sont connus sous le nom de modèle SWM. Le couplage entre les couches mène à une structure de bande strictement tridimensionnelle, c'est-à-dire que la relation de dispersion dans le plan dépend de k_z, où z est la direction verticale au plan. Au point K ($k_z = 0$) de la zone de Brillouin hexagonale la relation de dispersion des électrons dans le plan est parabolique (fermions massifs), tandis qu'au point H ($k_z = 0,5$) la relation de dispersion des trous dans le plan est linéaire (fermions de Dirac sans masse). Les propriétés magnétiques du graphite peuvent être dérivées du modèle SWM. On peut montrer que les propriétés de magnétotransport et l'effet de Haas-van Alphen sont dominés par deux groupes de porteurs, des électrons et des trous.

In this chapter the electronic and magnetic properties of graphite are discussed. Since graphite is a highly anisotropic layered material, a first approach towards the understanding of graphite is the analysis of the characteristics of a single layer treating the coupling between the graphite layers as a perturbation [20].

The first part of this chapter deals with the electronic properties of graphene. Even though the band structure of graphene has been known for a long time [20], it was only recently that it was investigated experimentally [5,46]. In the second part of the chapter, the influence of the coupling between the graphene layers on the band structure is discussed. The calculations are given by the so-called Slonczewski, Weiss and McClure model (*SWM-model*). It will be shown that the in-plane dispersion depends upon the momentum k_z in the direction perpendicular to the layers. At

the K point ($k_z = 0$) the in-plane dispersion of the electrons is parabolic (massive fermions), while at the H point ($k_z = 0.5$) the in-plane dispersion of the holes is linear (massless Dirac fermions). From the SWM-model the magnetic properties of graphite can be derived. It will be shown that the magnetotransport properties and the de Haas-van Alphen effect are dominated by two groups of carriers, electrons and holes.

3.1 The graphite lattice

3.1.1 Graphene

The structural features of the graphene lattice result from the character of the bonding between carbon atoms. The neutral carbon atom contains six electrons with the ground state configuration $1s^2 2s^2 2p^2$. An excited state with the electron configuration $1s^2 2s^1 2p_x^1 2p_y^1 2p_z^1$ is formed by the transition of a single electron from the 2s to the 2p state. The energy required to form the excited state is compensated by the formation of chemical bonds. In graphite the states of the $2p_x$ and $2p_y$ electrons are mixed with the remaining 2s state (sp^2 hybridization). The sp^2 hybridization leads to the formation of three equivalent bonds, which are referred to as σ bonds. The σ bonds, having the shape of asymmetrical eights, lie in the x-y plane and form an angle of 120° (Fig. 3.1 b)). They are the origin of the hexagonal structure of the graphene layer. The electron density distribution of the forth electron, given by the $2p_z$ state, has the form of a symmetric eight elongated in z-direction. In case the spins of neighbouring carbon atoms are antiparallel, the p_z electrons overlap and give rise to so-called π bonds. The electrical properties of graphite, i.e., high mobility and high conductivity, are associated with the π electrons, which are only very loosely bound.

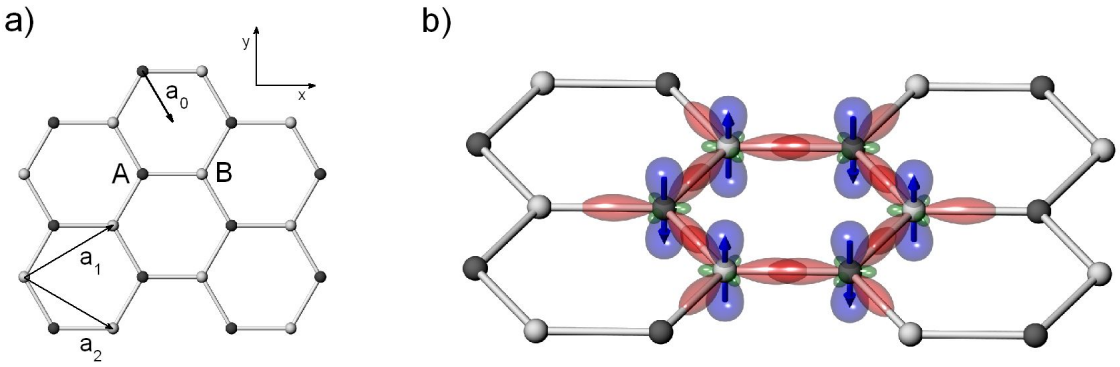

Fig. 3.1: ***a)*** *Graphene lattice. The non-equivalent carbon atoms, A and B, are arranged in a two-dimensional hexagonal lattice. The unit cell of the lattice is described by the two vectors* $\mathbf{a_1}$ *and* $\mathbf{a_2}$*. The distance between carbon atoms is* $a_0 = 1.42$ *Å.* ***b)*** *Atomic orbitals of the carbon atoms, hybridized in* sp^2 *configuration. The orbitals within the plane give rise to* σ *bonds. The* p_z *orbitals build up the* π *bonds, which requires the spins of the neighbouring carbon atoms to be antiparallel (arrows).*

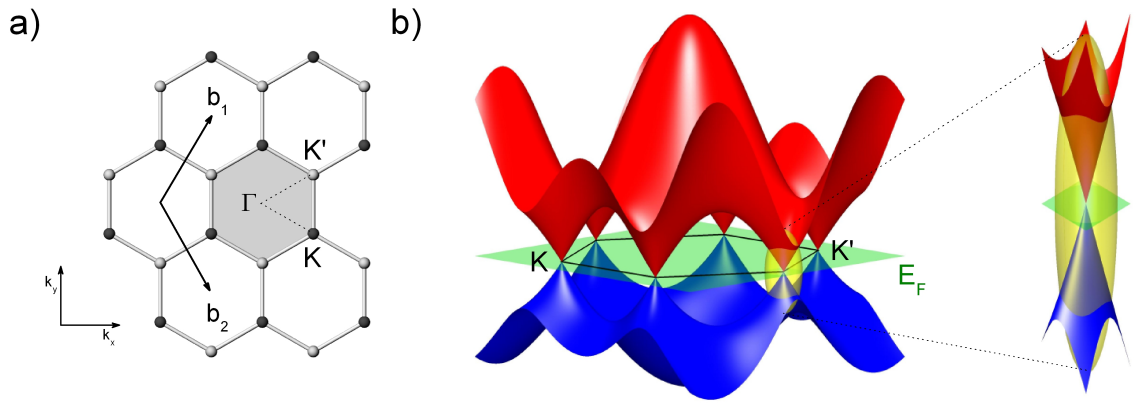

Fig. 3.2: ***a)*** *The graphene lattice in momentum space with its characteristic points Γ, K and K'.* ***b)*** *π band energy spectrum of graphene, calculated with Matlab using the tight-binding Hamiltonian of graphene [47]. The Fermi energy E_F lies in-between the upper and lower band. At the crossing points, the band energy depends linearly on the momentum, which is characteristic for relativistic particles with zero rest mass.*

Fig. 3.1 a) shows the hexagonal lattice of graphene. There are two non-equivalent carbon atoms per unit cell, labelled A and B. The unit cell of the lattice is described by two vectors

$$\mathbf{a_1} = \frac{a_0}{2}\left(\sqrt{3},1\right), \quad \mathbf{a_2} = \frac{a_0}{2}\left(\sqrt{3},-1\right),$$

where $a_0 = 1.42$ Å is the distance of neighbouring carbon atoms.

In Fig. 3.2 a), the first Brillouin zone of the graphene lattice is depicted, its characteristic points being the centre Γ and the corner points K and K', which are referred to as K points. For the understanding of the electrical properties of the graphene layer, only the π bonds have to be considered, since the σ bonds form an insulating-type band structure with an energy gap of several electron volts between the last completely filled and the first empty band [20]. Fig. 3.2 b) shows the π-electron band structure, obtained from tight binding calculations taking nearest neighbour (γ_0) and next nearest neighbour hopping (γ_0') into account [47]. The Fermi energy E_F is found at the touching points of the upper and lower π bands, i.e., at the points K and K'. To show the situation in the vicinity of the degeneracy points, a zoom in on the band structure close to the K points is given. Here the band structure depends linearly on the momentum $\mathbf{q}$, which is measured relatively to the K points,

$$E_\pm \approx \pm v_F |\mathbf{q}| + O\left[\left(\frac{q}{k}\right)^2\right]. \tag{3.1}$$

v_F is the Fermi velocity which is given by $v_F = 3\gamma_0 a/2 \approx 1\times10^6$ m/s for $\gamma_0 = 3.2$ eV [21].
The linear energy momentum dispersion relation in the vicinity of the Fermi energy is particular for graphene. Bands which linearly depend on the momentum q describe massless quasi-particles. This can be derived from the general energy momentum relation $E(q) = c\sqrt{q^2+m^2c^2}$, where c is the speed of light and m is the mass of the particle. For massive charge carriers with $mc \gg q$

the dispersion relation is parabolic, $E(\mathbf{q}) = q^2/(2m)$, which is common for "conventional" two-dimensional electron systems. Massless charge carriers on the other hand have a linear energy momentum dispersion relation $E(q) = cq$. In quantum mechanics, relativistic particles are described by the Dirac equation rather than the Schrödinger equation. The band structure in the vicinity of the Fermi energy is therefore often referred to as *Dirac cone* and the K points as *Dirac points*.

3.1.2 The three-dimensional graphite lattice

The lattice of graphite is built up of graphene sheets, which represent the structural units of graphite. They are stacked in the out of plane direction along the c-axis. The distance between two neighbouring layers is $c_0 = 3.35$ Å. X-ray studies reveal that monocrystalline graphite has most typically a hexagonal lattice, which is shown in Fig. 3.3 b) [1, 19]. In "hexagonal graphite" a row of atoms in a given layer is placed exactly above and below the centres of the hexagons of the neighbouring layers, i.e. consecutive layers are shifted relative to the preceding ones by the vector $\mathbf{a_0}$ given in Fig. 3.1 a). Consequently there are two inequivalent lattice sites in each layer, with atoms which have other atoms directly above and below them, and atoms which have no atoms above and below them in neighbouring layers. "Hexagonal graphite" is either referred to as AB stacked graphite, since the stacking order is repeated after every second layer, or to Bernal stacked graphite, since Bernal was the first who proposed the lattice in 1924 [1]. In Bernal stacked graphite, there are four atoms per unit cell.

The first Brioullin zone of the hexagonal graphite lattice is shown in Fig. 3.3 a). It represents a regular hexadron. Its most characteristic points are the centre Γ, the centres of the edges K and K' at $k_z = 0$, and the corner points of the top and bottom faces H and H' at $k_z = \pm 0.5$. Note that k_z is given in units of $c_0/2\pi$.

3.1.3 The band structure of graphite

Since the bonding between carbon atoms in the plane of a graphite layer is much stronger than the bonding between atoms in neighbouring layers, the behaviour of the electrons in graphite can be treated as being two-dimensional, including the interaction between layers as a perturbation. An early work by Wallace in 1947 [20] had shown that the charge carriers in AB stacked graphite occupy only small fractions of the first Brillouin zone (which is schematically shown in Fig. 3.3 a)) and that only the π bands near the vertical edges of the zone are important for the determination of the electronic properties of graphite. These facts were considered for the derivation of the effective mass Hamiltonian by Slonczewski, Weiss and McClure in the 1950s [2, 3], which describes the energy bands in the vicinity of the vertical edges, using the $\mathbf{k} \cdot \mathbf{p}$ method.

In the SWM-model the band structure near the Fermi energy is described by including seven binding parameters: γ_0–γ_5 and $\gamma_6 \equiv \Delta$. These parameters, also referred to as SWM- or γ-parameters, have the dimensions of energies. They define the interaction between various carbon atoms in the graphite lattice. The correspondence between these SWM-parameters and the interaction between the carbon atoms is shown in Figure 3.3 b). The parameter γ_0 is the only parameter which de-

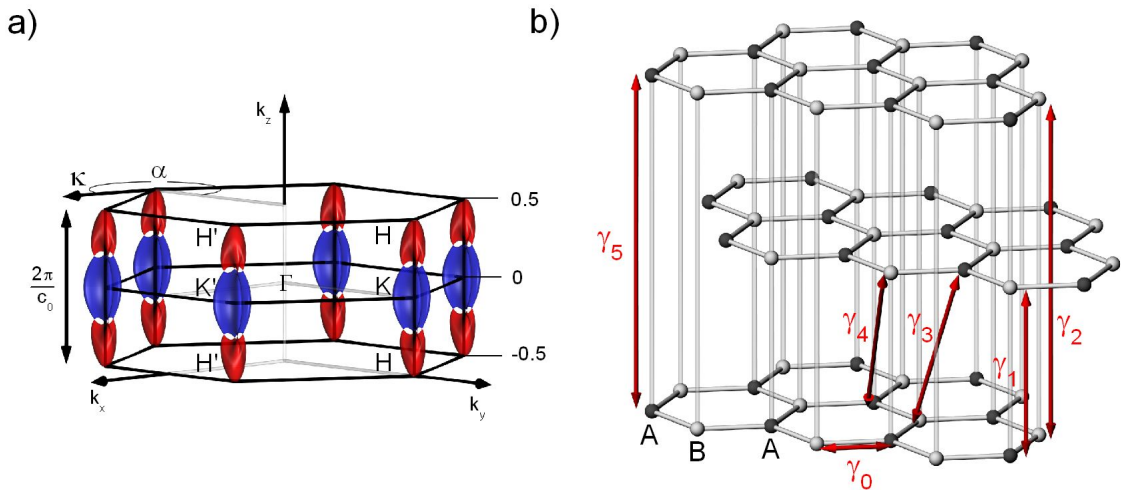

Fig. 3.3: ***a)*** *First Brillouin zone of graphite. It represents a regular hexadron. The characteristic points are the centre* Γ*, the edge points K and K', and the corner points H and H'. Note that* k_z *is given in units of* $c_0/2\pi$*. The carriers occupy only a small region along the H-K-H edge, which is schematically indicated by the pockets.* ***b)*** *Bernal stacked graphite. Consecutive layers are shifted by the vector* $\mathbf{a_0}$ *given in Fig. 3.1 a). The interaction between the carbon atoms are described by so-called* γ*-parameters.*

scribes the interaction of carbon atoms within a graphite layer. The remaining parameters describe interactions between atoms in various layers. The parameter γ_1 corresponds to the interaction of A and B atoms stacked directly above each other. γ_2 describes the interaction between B-type atoms in second nearest lattices. γ_3 and γ_4 describe the interaction between B-A atoms and A-B atoms, respectively, which are not stacked directly one above the other. γ_5 determines the interaction between two second nearest A atoms. The parameter $\gamma_6 \equiv \Delta$ reflects the inequivalence between the atoms A and B once the presence of neighbouring layers is taken into account. The values of the γ-parameters used throughout this thesis are given in Table 5.1 (page 63).

Taking into account the symmetry of the graphite lattice and the coupling between the carbon atoms, the SMW Hamiltonian is given by [2],

$$H = \begin{pmatrix} \varepsilon_1^0 & 0 & H_{13} & H_{13}^* \\ 0 & \varepsilon_2^0 & H_{23} & -H_{23}^* \\ H_{13}^* & H_{23}^* & \varepsilon_3^0 & H_{33} \\ H_{13} & -H_{23} & H_{33}^* & \varepsilon_3^0 \end{pmatrix}, \tag{3.2}$$

where

$$\begin{aligned} \varepsilon_1^0 &= \Delta + \gamma_1\Gamma + \frac{1}{2}\gamma_5\Gamma^2, \qquad \varepsilon_2^0 = \Delta - \gamma_1\Gamma + \frac{1}{2}\gamma_5\Gamma^2, \qquad \varepsilon_3^0 = \frac{1}{2}\gamma_2\Gamma^2 \\ H_{13} &= \frac{1}{\sqrt{2}}(-\gamma_0 + \gamma_4\Gamma)\sigma e^{i\alpha}, \quad H_{23} = \frac{1}{\sqrt{2}}(\gamma_0 + \gamma_4\Gamma)\sigma e^{i\alpha}, \quad H_{33} = \gamma_3\Gamma\sigma e^{i\alpha}, \end{aligned} \tag{3.3}$$

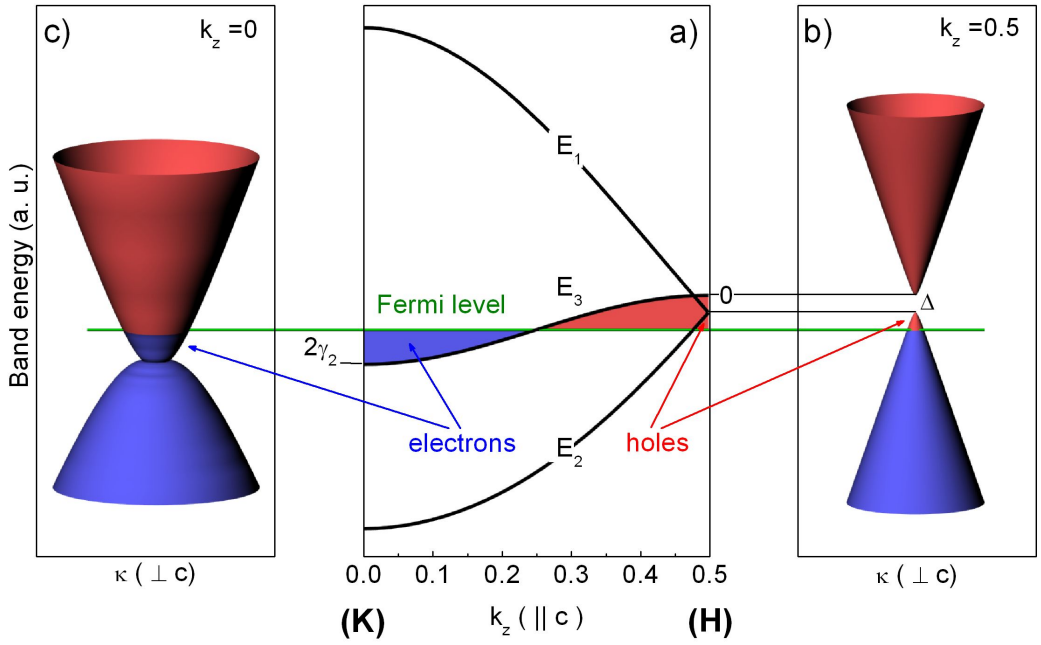

Fig. 3.4: ***a)*** *Band structure of graphite as a function of $k_z(\|c)$ obtained from diagonalizing the SWM Hamiltonian (3.2) using Matlab. The parameters γ_2 and Δ have been multiplied by a factor of four and seven, respectively, for illustration reasons. Two of the bands, labelled E_3 bands, are degenerate along the edge H-K-H. The Fermi energy lies in the middle of those bands.* ***b)*** *For $k_z = 0$, the in-plane dispersion relation ($\kappa(\perp c) \neq 0$) is given by two parabolas, which describe massive charge carriers with an effective mass m^*.* ***c)*** *The in-plane band structure at the H point resembles that of graphene, since at $k_z = 0.5$ the intra-layer coupling is zero (see Eqs. (3.3) and (3.4)).*

with

$$\Gamma = 2\cos(\pi k_z),\ \sigma = \sqrt{3}a_0\kappa/2 \text{ and } \kappa = \sqrt{k_x^2 + k_y^2}. \tag{3.4}$$

α is the angle between the momentum $\boldsymbol{\kappa}$ and the ΓK direction (see Fig. 3.3 a)). a_0 is the in-plane lattice parameter. k_x and k_y are measured with respect to the H-K-H edge of the Brillouin zone.

The eigenvalues for the energy spectrum of graphite are found by diagonalizing the SMW Hamiltonian. The result of such a calculation is sketched in Fig. 3.4. The parameters γ_2 and Δ have been multiplied by a factor of four and seven, respectively, for illustration reasons. In Fig. 3.4 a) the band energies are given as a function of the momentum in z-direction, $k_z(\| c)$, between the K and H points. Two of the four solutions of the eigenvalue problem are nondegenerate at $k_z \neq 0.5$. They are referred to as E_1 and E_2 bands, respectively. The two other solutions are degenerate along the H-K-H edge and are referred to as E_3 bands. The band overlap of the E_3 bands is $2|\gamma_2|$. The Fermi level is found to be approximately in the middle of these bands ($E_F \approx -|\gamma_2|$) which comes from the fact that in electrically neutral graphite the densities of electrons and holes are equal. The band

structure reveals that graphite is a semimetal. The small carrier density is linked to the smallness of the parameter γ_2.

At the K point, the degeneracy of the E_3 bands is lifted if one departs from the H-K-H edge ($\kappa(\perp c) \neq 0$). This is shown on the left hand side of Fig. 3.4. The in-plane band structure for $k_z = 0$ is given by two parabolas which overlap at the K point[1]. The curvature of these bands define the effective mass m^* of the K point electrons[2]. At the H point, the bands E_1 and E_2 are degenerate, separated from the two fold degenerate E_3 bands by the energy Δ, which corresponds to the γ-parameter $\gamma_6 \equiv \Delta$. This degeneracy persists for $\kappa(\perp c) \neq 0$. The in-plane dispersion at $k_z = 0.5$ resembles the band structure of graphene, with the energy having a linear dependence on the momentum vector $\boldsymbol{\kappa}$. This behaviour arises from the fact that the strength of the interlayer coupling is zero at the H point, as the interlayer coupling parameters always enter the SWM Hamiltonian in the combination $\gamma_i \cdot \cos(\pi k_z)$, which becomes zero for $k_z = 0.5$ (see Eqs. (3.3) and (3.4)). There are three major differences with respect to the graphene layer. First, the Fermi energy is not found exactly between the two cones. Second, the two cones do not overlap, and third, the two bands are twofold degenerate with respect to graphene, i.e., each graphene layer state corresponds to two states in the three-dimensional graphite lattice.

The Fermi surface of graphite along the edge K-H with the electron pocket at the K point and the hole pocket at the H point is depicted in Fig. 3.5. It was constructed by computing the crossing points of the bands $E_i(\kappa)$ with the Fermi energy for given values of k_z. For illustration reasons, the k_x-k_y-plane has been magnified by a factor of 5. The trigonal symmetry of the Fermi surface in the k_x-k_y plane is due to the parameter γ_3 which is therefore also often referred to as the *trigonal warping* parameter. Trigonal warping is particularly distinct at the K points ($k_z = 0$) at which $\cos(\pi k_z) = 1$. If γ_3 is neglected, the Fermi surface has a perfect cylindrical symmetry. Indeed, cylindrical symmetry is observed at the H point, at which the effect of the inter-plane parameters is zero, and the Fermi surface has a circular cross section.
At the H point, two hole surfaces overlap. The hole pocket with the larger cross section for $k_z < 0.5$ is associated with the band E_1, as shown in the upper inset of Fig. 3.5. The hole pocket with the smaller cross section is due to the band E_2. The charge carriers associated with the two bands are referred to as majority and minority holes, respectively. A more detailed discussion is given in the following section.
In the regions where the electron pocket is in contact with the hole pocket, the Fermi surface has a complicated structure. Here, the SWM-model predicts so-called "outriggered pieces", also referred to as "leg" and "centre" pieces [48]. The "centre" and the three "leg" pieces have their origin in the overlap of the E_3 bands, as depicted in the lower inset of Fig. 3.5.

[1] Triganol warping, discussed subsequently, is not seen for this set of parameters (γ_2 multiplied by four, Δ multiplied by seven.)
[2] $m^* = \frac{\hbar^2}{\partial^2 E/\partial \kappa^2}$

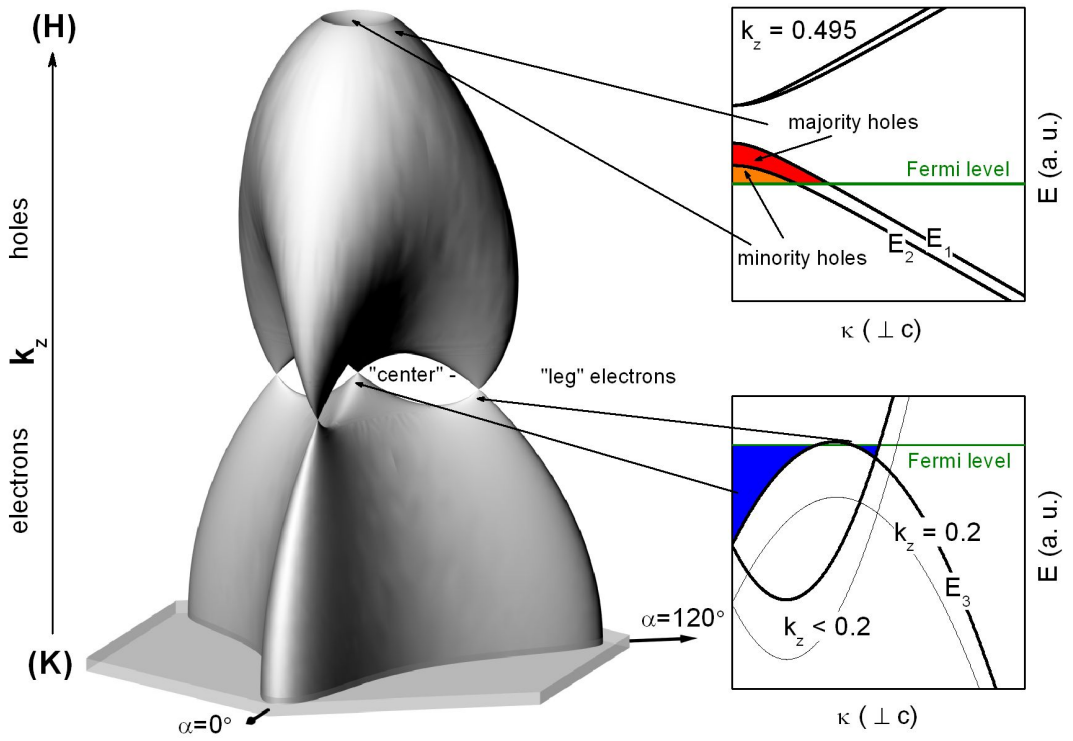

Fig. 3.5: *Fermi surface of graphite along the edge K-H with the electron pocket at the K point and the hole pocket at the H point calculated using Matlab. It has a trigonal symmetry, which is particularly distinct at the K point. The electron and hole pockets are connected by so-called "centre" and "leg" pieces, which originate from the overlap of the E_3 bands (see lower inset). At the H point, an additional hole pocket, which is associated with the E_2 band, is found (see upper inset). For illustration reasons the k_z values have been divided by a factor of ≈ 5.*

3.2 Magnetic properties of graphite

3.2.1 Semi classical approximation

A qualitative understanding of the magnetic field behaviour of charge carriers in graphite can be found most simply using the semi classical approximation. In order to quantize the electron spectrum, one can then make use of the Lifshitz-Onsager formula (Eq. (2.15)),

$$S_N = \pi k_\perp^2 = (N+\gamma)\frac{2\pi eB}{\hbar}, \tag{3.5}$$

where S_N are the extremal cross section areas of the closed electron and hole orbits in k space perpendicular to the direction of the magnetic field.

Fig. 3.6 a) shows the extremal orbits of the Fermi surface of graphite along the edge H-K-H, with the magnetic field being applied in the direction of the k_z-axis. For illustration reasons, the value

of k_z has been divided by a factor of 2.5. The extremal orbits at the K point ($k_z = 0$) and at $k_z \approx 0.3$ close to the H point ($k_z = 0.5$) are due to electrons and holes, respectively. Because of the extent of their cross section areas S_N, they are referred to as *majority electrons* and *majority holes*. Figs. 3.6 c) and d) show the parabolic in-plane ($\kappa \perp c$) dispersion relation for both k_z values. At the H point, where the in-plane dispersion relation is linear (see Fig. 3.6 b)) there exists an additional small extremal orbit, referred to as *minority holes*. The additional hole pocket is shown in Fig. 3.7 a) in more detail. Directly at the H point the majority and the minority hole surfaces overlap. This means that in principal minority holes can only be observed if the magnetic field is tilted with respect to the H-K-H edge, since only in this case there exist extremal orbits. When spin orbit coupling is included in the SWM Hamiltonian (Fig. 3.7 b)), the degeneracy of the surfaces at the H point is lifted, and minority carriers should be observed even for magnetic fields perpendicular to the sample plane. Theoretically, the "central" and "leg" levels give rise to additional groups of minority carriers. However, due to their extremely small cross section areas, they have never been observed experimentally [28].

With the knowledge of the k_z positions of the extremal orbits of the Fermi surface of graphite, the magnetic field properties of these carriers can be investigated. In Section 3.1.3 it was shown that the topology of the band structure is fundamentally changed along the H-K-H axis of the Brillouin zone. This has consequences for the magnetic field behaviour of the Landau bands.

The majority electrons at the K point and the majority holes at $k_z \approx 0.3$ have a parabolic energy-momentum in-plane dispersion relation $E = \hbar^2 \kappa^2 / 2m^*$ which leads with Eq. (3.5) to

$$E = \hbar \omega_c (N + \gamma). \tag{3.6}$$

This result was derived in Section 2.1 and it was shown that $\gamma = 1/2$ for free electrons. The phase term, however, can as well depend on the topology of the Fermi surface, i.e., differ from the usual value of $\gamma = 1/2$. This is taken into account by introducing the so-called *geometrical* or *Berry phase* Φ_B so that [22]

$$\gamma = \frac{1}{2} - \frac{\Phi_B}{2\pi}.$$

From a topological point of view, a value of the Berry phase different than zero can be explained by the occurrence of degenerate electron states at band-contact lines, with the Brillouin zone playing the role of the parameter space [49].

At the H point of graphite, the location of the minority holes, the band energy depends linearly on the momentum κ. If the energy gap Δ between the two cones at the H point of graphite is neglected, $E = \pm v_F \hbar |\kappa|$, so that with the semi classical Eq. (3.5)

$$E = \pm v_F \sqrt{2\hbar e B (N + \gamma)}. \tag{3.7}$$

This means that in contrast to the usual Landau bands whose energy depends linearly on the magnetic field and which are equally spaced for a given magnetic field, the energy of the Landau bands at the H point of graphite has a square root dependence on the magnetic field and on the quantum number N. Moreover, the Berry phase is $\Phi_B = \pi$, so that the phase term vanishes, i.e.,

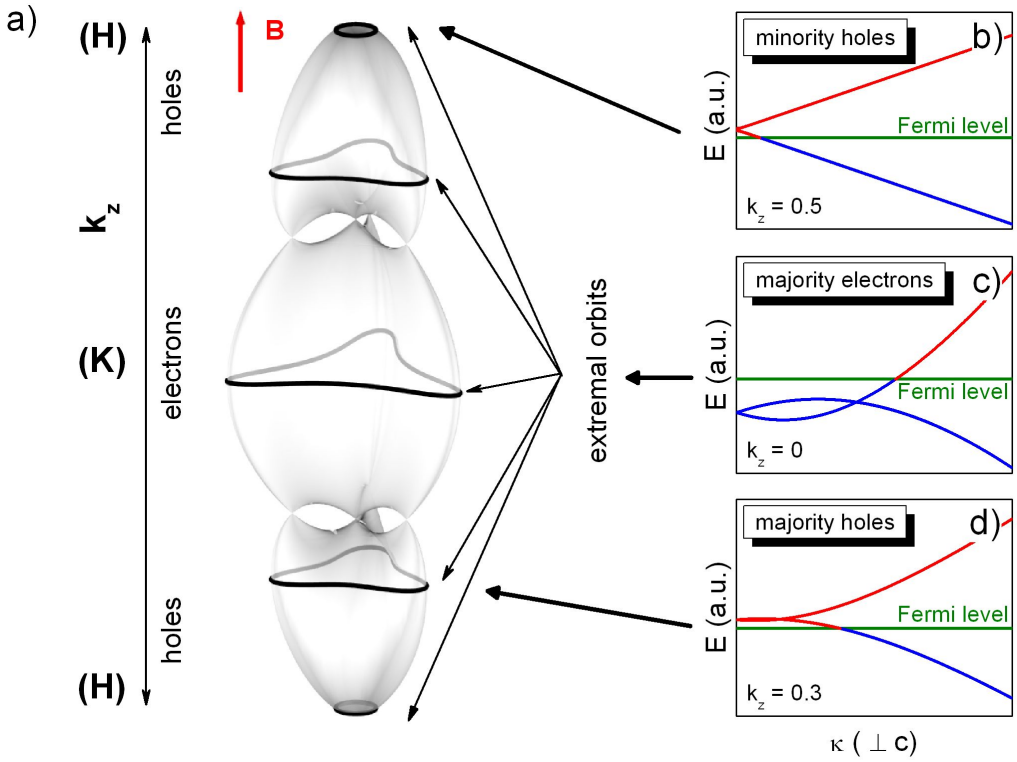

Fig. 3.6: ***a)*** *Fermi surface of graphite along the edge H-K-H with its electron and hole pockets. For illustration reasons the value of k_z has been devided by a factor of 2.5. The extremal orbits at the K point ($k_z = 0$) and at $k_z \approx 0.3$ close to the H point ($k_z = 0.5$) are due to majority electrons and holes, respectively. At the H point an additional extremal orbit, referred to as minority holes, is observed.* ***b)-d)*** *In-plane dispersion relation at $k_z = 0$ (majority electrons), $k_z = \pm 0.3$ (majority holes) and $k_z = \pm 0.5$ (minority holes). While the in-plane dispersion relation is parabolic for the majority carriers, it is linear for the minority holes.*

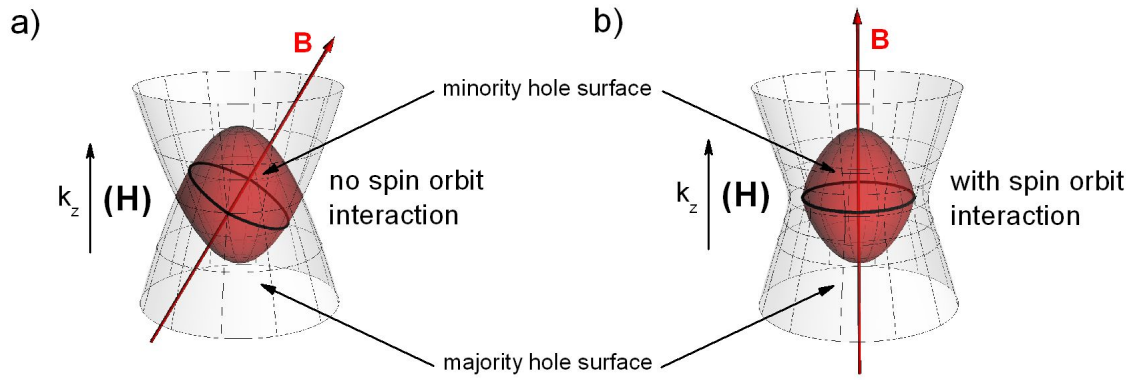

Fig. 3.7: ***a)*** *Zoom in on the Fermi surface of graphite in the region of the H point ($k_z = 0.5$). An additional hole pocket is observed. Due to its small cross section, its carriers are referred to as minority holes. In principle minority holes can only be observed in tilted field configuration, due to the degeneracy of the bands directly at the H point.* ***b)*** *If spin orbit coupling is included in the SWM model, the degeneracy in the k_z plane is lifted, and minority carriers should as well be observed for magnetic fields perpendicular to the sample plane.*
The Fermi surfaces were calculated using Matlab. The SWM-Hamiltonian including the spin orbit interaction was taken from Ref. [50].

$\gamma = 0$ [22]. In the next section it will be shown that this result can be directly derived from the energy spectrum of the magnetic field Hamiltonian of graphite.

The energies of the Landau bands at the H point of graphite resemble the unusual energy spectrum of the Landau levels in graphene as a function of the magnetic field, as shown in Fig. 3.8. In graphene, the $N = 0$ Landau level is two times spin degenerate and two times so-called valley degenerate, which comes from the fact that there are two inequivalent points K and K´ at the edges of the hexagonal Brillouin zone. The $N > 0$ and $N < 0$ Landau levels are referred to as electron and hole levels, respectively. Whereas for an undoped system the Fermi level is placed at the crossing point of the two cones, it can be shifted to higher or lower energies by doping, which adds or removes charge carriers. To illustrate the movement of the Fermi energy, it is assumed to have an excess of electrons. The periodicity in $1/B$ of the Fermi energy jumps is the same as for the free electron Landau levels.

3.2.2 The magnetic field Hamiltonian

On the basis of the SWM-model, the Hamiltonian defining the energy bands in magnetic field was derived by McClure [23] and Inoue [24] assuming that the magnetic field is directed along the c-axis, i.e., parallel to the direction of k_z. In matrix form the Hamiltonian is given by

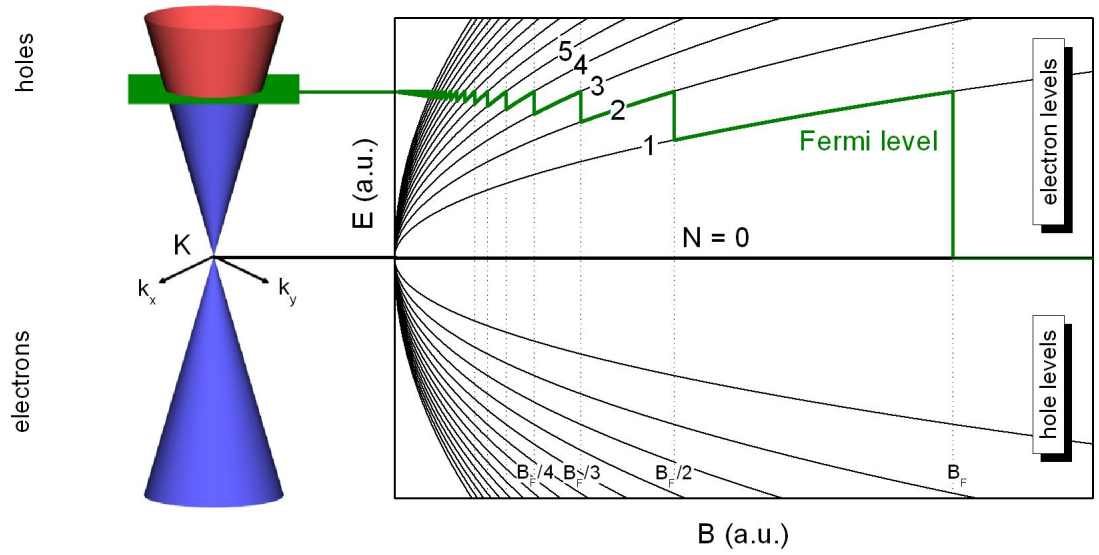

Fig. 3.8: *Energy dispersion relation of graphene as a function of the magnetic field. The Fermi energy in graphene is governed by the degeneracy of the Landau levels and jumps for magnetic fields $B_F/(N+1)$ to the next level. For the illustration of the Fermi energy movement it is assumed to have an excess of electrons, i.e., the Fermi energy is found above the K point.*

$$H = \begin{pmatrix} \varepsilon_1^0 & 0 & \sqrt{\frac{\xi}{2}}(1-\nu)\sqrt{N+1} & -\sqrt{\frac{\xi}{2}}(1-\nu)\sqrt{N} \\ 0 & \varepsilon_2^0 & \sqrt{\frac{\xi}{2}}(1+\nu)\sqrt{N+1} & -\sqrt{\frac{\xi}{2}}(1+\nu)\sqrt{N} \\ -\sqrt{\frac{\xi}{2}}(1-\nu)\sqrt{N+1} & \sqrt{\frac{\xi}{2}}(1-\nu)\sqrt{N} & \varepsilon_3^0 & \gamma_3\Gamma\sqrt{\xi}a \\ -\sqrt{\frac{\xi}{2}}(1-\nu)\sqrt{N} & -\sqrt{\frac{\xi}{2}}(1+\nu)\sqrt{N} & \gamma_3\Gamma\sqrt{\xi}a^\dagger & \varepsilon_3^0 \end{pmatrix},$$

where

$$\xi = \xi' B = 3a_0^2\gamma_0^2\left(\frac{e}{2\hbar}\right)B \quad \text{and} \quad \nu = \frac{\gamma_4\Gamma}{\gamma_0}. \tag{3.8}$$

N is an integer number with $N \geq -1$. $\Gamma = 2\cos(\pi k_z)$ has been defined in Eq. (3.4). a and $a^\dagger$ in the γ_3 terms are ladder operators with

$$a\Psi_N = \sqrt{N}\,\Psi_{N-1} \quad \text{and} \quad a^\dagger\Psi_N = \sqrt{N+1}\Psi_N.$$

For $\gamma_3 = 0$ the basis vectors of the Hamiltonian are $|\Psi_N>$, $|\Psi_N>$, $|\Psi_{N+1}>$, $|\Psi_{N-1}>$. In this basis $\gamma_3 \neq 0$ would couple the matrix elements

$$\begin{aligned} &<\Psi_{N+1}|H_{33}|\Psi_{N-1}> \propto <\Psi_{N+1}|\Psi_{N-2}> \quad \text{and} \\ &<\Psi_{N-1}|H_{33}^*|\Psi_{N+1}> \propto <\Psi_{N-1}|\Psi_{N+2}> \quad , \end{aligned}$$

i.e., terms with quantum numbers N would be coupled to those with quantum numbers $N \rightarrow N \pm 3$, which breaks the dipole selection rules $N \rightarrow N \pm 1$ [51]. The basis has therefore to be changed. The Hamiltonian taking the parameter γ_3 into account is of infinite size.

Choosing the basis $\chi = (\chi(-1),\ \chi(0),\ \chi(1),\ \chi(2),\ \ldots)$, with $\chi(N) = (\Psi(N),\ \Psi(N),\ \Psi(N+1),\ \Psi(N-1))$, the Hamiltonian can be rewritten as [52]

$$H = \begin{pmatrix} D_0(-1) & 0 & 0 & D_1 - 1 & 0 & \cdots \\ 0 & D_0(0) & 0 & 0 & D_1(0) & \cdots \\ 0 & 0 & D_0(1) & 0 & 0 & \cdots \\ D_1^+(-1) & 0 & 0 & D_0(2) & 0 & \ldots \\ 0 & D_1^+(0) & 0 & 0 & D_0(3) & \cdots \\ \vdots & \vdots & \vdots & \vdots & \vdots & \ddots \end{pmatrix},$$

where the submatrix $D_0(N)$ is the matrix (3.8), with $\gamma_3 = 0$. $D_1(N)$ contains the γ_3 parameter and is given by

$$D_1(N) = \begin{pmatrix} 0 & 0 & 0 & 0 \\ 0 & 0 & 0 & 0 \\ 0 & 0 & 0 & 0 \\ 0 & 0 & \gamma_3 \Gamma \sqrt{b} \sqrt{N+2} & 0 \end{pmatrix},$$

The matrixes $D_0(-1)$ and $D_0(0)$ have special forms, which are obtained from the matrix (3.8) by eliminating terms with negative quantum numbers.

Even though the SWM Hamiltonian in magnetic field has infinite dimensions, its eigenvalues can be obtained by truncating the infinite matrix into a finite one as the energies of the levels converge for large quantum numbers N. In this thesis we have used matrixes with 600×600 elements. The size of the matrixes was found to be sufficient since for higher order matrixes no noticeable differences in the eigenvalue spectra were observed. To simplify the discussion at this point, however, the parameter γ_3 is neglected and the eigenvalue problem is reduced to a four by four matrix. A detailed discussion of the implementation of the magnetic field SWM Hamiltonian in *Matlab* is given in the Appendix A.3.

Fig. 3.9 a) shows the evolution of the bands as a function of the wave vector k_z between the points K and H for $B = 8$ T (γ-parameters in Table 5.1 with $\gamma_3 = 0$). The bands E_1, E_2 and E_3 are split into Landau sub-bands with quantum numbers $N = -1, 0, 1, 2, \ldots$. The Fermi energy crosses the bands $N = 0$ and $N = -1$ approximately in the middle.

The Landau bands at the K point at low energies are quite accurately described by linear functions of the magnetic field, as illustrated in Fig. 3.9 b). According to Eq. (3.6), the linear magnetic field dependence of the Landau bands is expected, since the in-plane dispersion relation at the K point is to a first approximation parabolic (see Fig. 3.4). The simplest model describing the magnetic

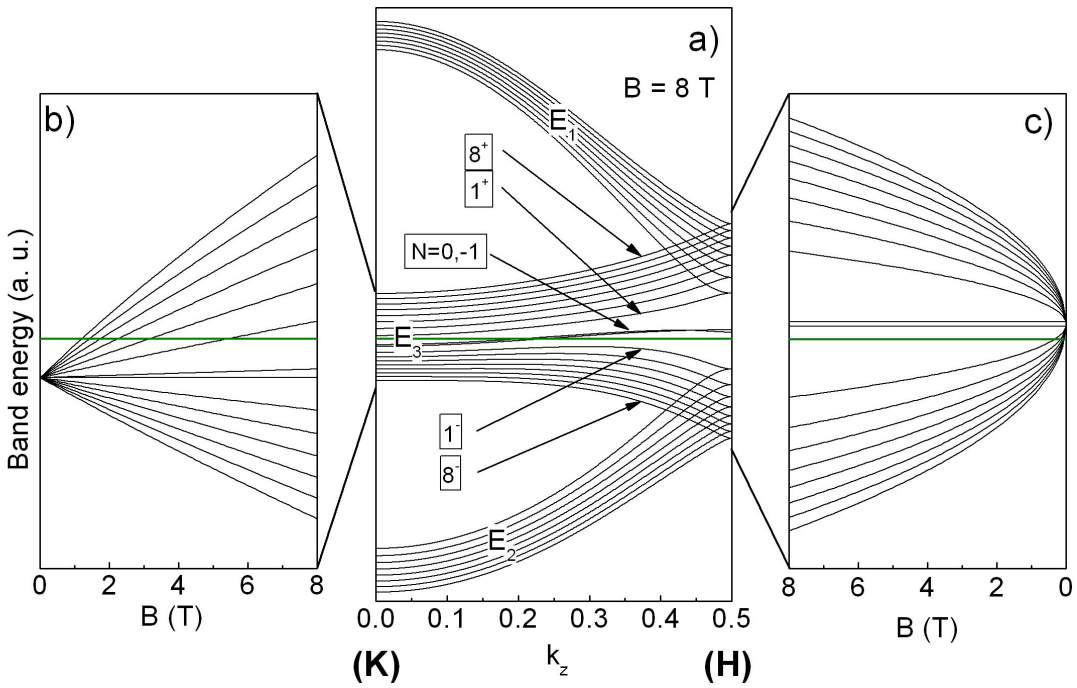

Fig. 3.9: ***a)*** *Evolution of the bands as a function of the wave vector k_z between the points K and H for $B = 8$ T (γ parameters in Table 5.1 with $\gamma_3 = 0$). The bands E_1, E_2 and E_3 are split into Landau sub-bands with quantum numbers $N = -1, 0, 1, 2, \ldots$. The Fermi energy lies approximately in the middle of the levels $N = -1$ and $N = 0$.* ***b)*** *Evolution of the bands at the K point as a function of the magnetic field. The Landau band energies are to a good approximation linear functions of the magnetic field, as expected for a parabolic potential (see Fig. 3.4). The Fermi energy as a function of the magnetic field is constant.* ***c)*** *Square root of B dependence of the energy bands at the H point, at which the inter-layer coupling is zero.*

field dispersion relation at the K point is given by a graphene bilayer with an effective interlayer coupling $2\gamma_1$ [21].

At the H point of the hexagonal Brillouin zone of graphite, the effect of the inter layer coupling parameters is zero, as they enter the Hamiltonian in the combination $\Gamma\gamma_i$ ($i = 1,\ldots,6$), with $\Gamma = 0$ for $k_z = 0.5$. The band structure of graphite corresponds therefore to a good approximation to that of a graphene layer. Neglecting all the inter layer coupling parameters, the magnetic field Hamiltonian (3.8) is radically simplified. The energy eigenvalues as a function of the magnetic field are given by

$$E = \frac{\Delta}{2} \pm \sqrt{\frac{\Delta^2}{4} + (N, N+1)\xi' B},$$

where $(N, N+1)$ is N or $(N+1)$, i.e., the counting of the quantum number N starts either at $N = 0$ or $N = -1$. The phase γ in the *Lifshitz-Onsager* relation (2.16) is zero. This means that the Berry phase is either $\Phi_B = \pi$ or $\Phi_B = -\pi$. Both values are equivalent. The square root of B dependence of the Landau bands at the H point is depicted in Fig. 3.9 c).

For $\Delta = 0$, the Landau band dispersion is the same as predicted by the Onsager quantization condition for a graphene layer with $\gamma = 0$ (see Eq. (3.7)). Several differences between the charge carriers in graphene and those at the H point of graphite for $B = 0$ T have been mentioned previously. The most striking difference in magnetic field concerns the position of the Fermi energy. While in three-dimensional graphite it remains to a good approximation constant when the magnetic field is changed, the Fermi energy in graphene is governed by the degeneracy of the Landau levels and jumps at the magnetic field $B_F/(N+1)$ to the level $N+1$ (see Fig. 3.8).

Finally the evolution of the k_z dependent Landau bands in magnetic field is illustrated in Fig. 3.10. The energies of the Landau bands are given as a function magnetic field in the range $B = 2.5$ - 8 T and the wave vector k_z along the K-H edge. For the calculation, the full Hamiltonian has been taken into account (parameters in Table 5.1). Spin splitting has been neglected. The Fermi level is given by the plane, which crosses the bands $N = -1$ and $N = 0$ roughly in the middle. In the magnetic field range depicted here, the value of the Fermi energy is not constant, but varies as a function of the magnetic field due to a considerable electron hole cross talk. A detailed discussion of the Fermi energy movement, crucial for the understanding of orbital and spin effects, will be given in Chapter 5.4. When the magnetic field is decreased, the energy of the bands $N = 1^-, 2^-, \ldots$ increases, while the energy of the bands $N = 1^+, 2^+, \ldots$ decreases. The notation N^+ and N^- labels the two different E_3 bands, which are doubly degenerate at $B = 0$ T. Local extrema of the bands $N = 1^+, 2^+, \ldots$ and $N = 1^-, 2^-, \ldots$ successively cross the Fermi energy at the K point ($k_z = 0$) and at $k_z \approx 0.3$, respectively. Those extrema correspond to the extremal cross sections of majority electrons and holes which were discussed previously. We will see in Chapter 5.4 that the crossing of the local extrema translates to maxima in the density of states at the Fermi energy. The maxima in the density of states can be probed directly by measuring either the resistivity ρ_{xx} as a function of the magnetic field (Shubnikov-de Haas oscillations) or the magnetic field dependent magnetization (de Haas-van Alphen effect).

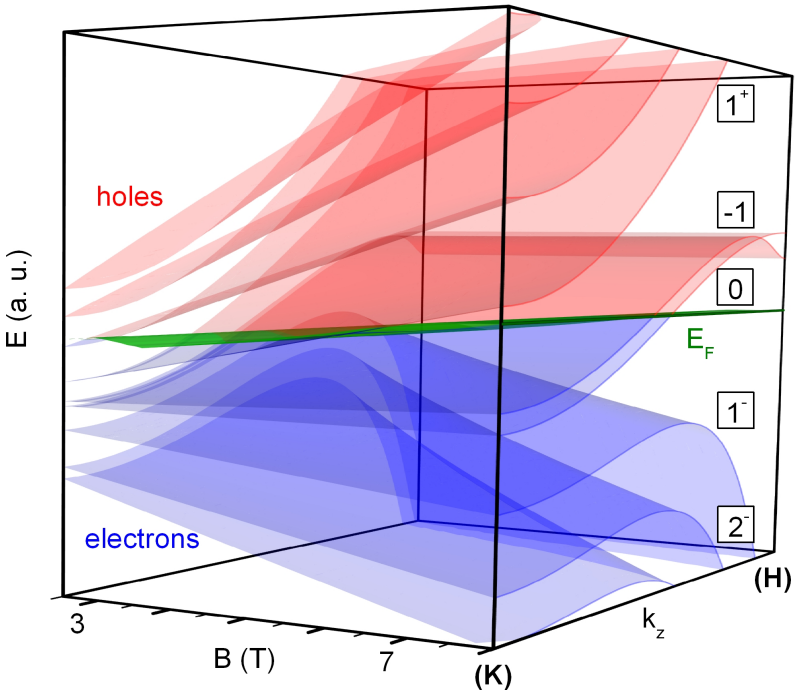

Fig. 3.10: *Landau band energies as a function of the magnetic field in the range $B = 2.5$ - 8 T and the wave vector k_z along the K-H edge calculated with the full Hamiltonian (parameters in Table 5.1). Spin-splitting was neglected. The Fermi level E_F is given by the plane which crosses the bands $N = -1$ and $N = 0$ at high magnetic fields. Local extrema of the bands $N = 1^+, 2^+, \ldots$ and $N = 1^-, 2^-, \ldots$ successively cross the Fermi energy at the K point and at $k_z \approx 0.3$, when the magnetic field is decreased.*

4 Experimental Methods

Résume du chapitre

Deux types d'échantillons de graphite ont été étudiés dans cette thèse: du graphite HOPG (Highly Oriented Pyrolytic Graphite) et du graphite naturel. Pour les mesures de magnétotransport des contacts ont été déposés sur ces échantillons en configuration de type "barre de Hall". Les mesures de l'effet de Haas-van Alphen ont été effectuées en utilisant la méthode de couple. Pour les mesures deux systèmes d'aimants différents ont été employés: deux aimants supraconducteurs avec des champs magnétiques maximaux de $B = 11$ T et $B = 16$ T à la température de l'hélium liquide ($T = 4.2$ K) et un aimant résistif de 20 MW, avec un champ magnétique maximum de $B = 28$ T. Les mesures ont été effectuées dans trois systèmes cryogéniques différents: Un "anti-cryostat" (ou VTI = Variable Temperature Insert) avec une température de base de $T_b \approx 1.2$ K, un cryostat ^{3}He avec $T_b \approx 300$ mK et deux réfrigérateurs à dilution avec $T_b \approx 10$ mK (aimant supraconducteur) et $T_b \approx 30$ mK (aimant résistif).

The present chapter is devoted to the experimental methods. To start with, the preparation of the different graphite samples for magnetotransport measurements is explained. Then the experimental setup - magnets and cryogenics - is briefly discussed. Finally the techniques to measure magnetotransport and the de Haas-van Alphen effect are presented.

4.1 The Graphite samples

Two types of graphite samples were studied in this work: Highly Oriented Pyrolytic Graphite (HOPG) and natural graphite (NG). HOPG is a synthetic form of graphite manufactured by decomposition of hydrocarbon gas at high temperature ($T \approx 3000$ K) and under high pressure. This treatment leads to a very pure material with well oriented horizontal planes. The HOPG material was bought commercially.

Natural graphite samples are single crystals showing a very high crystalline perfection with identically stacked planes. The samples studied in this work were provided through collaboration with

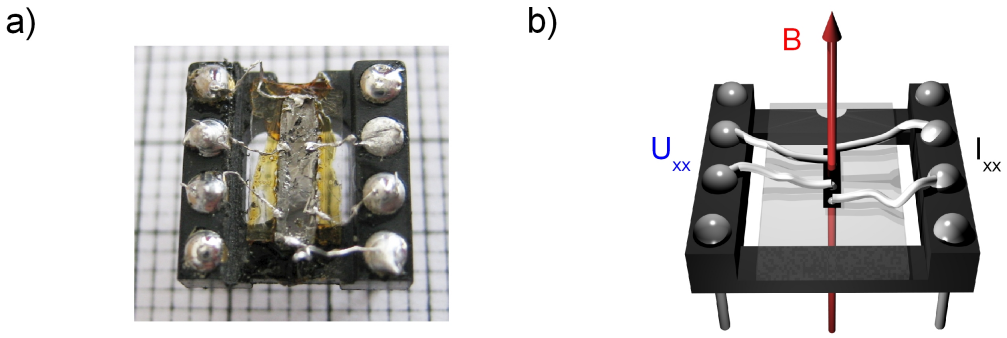

Fig. 4.1: ***a)*** *HOPG sample, cleaved from a larger piece of a bulk. The contacts for magnetotransport were soldered with indium in Hall bar configuration.* ***b)*** *Schematic of a natural graphite sample on an eight-pin socket. Four contacts for measurements of the longitudinal resistance R_{xx} are glued on the sample with silver paint.*

another research group, who also investigated this material [53].

Fig. 4.1 a) shows the HOPG sample used for the magnetotransport measurements in Hall-bar configuration. It was cleaved from a larger piece of a bulk HOPG. The cleavage process explains the non planar surface of the sample. Its dimensions are about 9 mm $\times$ 2 mm $\times$ 0.5 mm (length$\times$width$\times$height). The sample was first glued on an insulating support, which was then glued on an eight-pin socket for magnetotransport measurements. The connection between the soldering posts of the eight-pin socket and the surface were made under a microscope with thin gold coated copper wires. The wires were soldered with indium on the surface of the HOPG sample. For the natural graphite samples we applied contacts both in Hall-bar and in four-point configuration using the same gold coated copper wires and silver paint. A schematic representation of the natural graphite sample with contacts in four-point configuration mounted on an eight-pin socket is given in Fig. 4.1 b). The samples were quite small, their width and length not exceeding a few millimetres. The thickness of the sample was in the submillimetre range.

4.2 Magnets

For the measurements presented in this thesis, two kinds of magnet systems were used: Two superconducting magnets with maximum magnetic fields at liquid helium temperature ($T = 4.2$ K) of $B = 11$ T and $B = 16$ T, respectively, and a 20 MW resistive magnet with a maximum magnetic field of $B = 28$ T.

4.2.1 Superconducting magnet

The main advantage of a superconducting magnet is that only small amounts of electrical power are required to create relatively high magnetic fields. The maximum field is given by the critical field H_{c2} of the coil material. At H_{c2} the superconducting state is destroyed and the normal conducting

state is restored. The coil becomes resistive and dissipates power. To prevent this, the field of the magnet has to be kept below H_{c2}. Nowadays superconducting magnets with maximum fields up to $B = 22$ T are available.

Due to the high stability of the current in the coil which has a large induction, the coil provides a very good spatial and temporal homogeneity of the field. The absence of water cooling (which causes vibrations) leads to a much lower noise compared to resistive magnets.

Superconducting magnets are therefore suitable for experiments requiring high standards for the signal to noise ratio and the homogeneity of the field, without demanding too high magnetic fields. There is, however, the need for cryogenics at temperatures of liquid helium (≤ 4.2 K) to maintain the superconducting state of the coil.

4.2.2 Resistive magnets

The advantage of resistive magnets compared to superconducting ones are the higher magnetic fields which can be obtained using this technique. Limitations of the maximum magnetic field are mainly given by cooling and by mechanical stresses due to Lorentz forces in the magnet. Resistive magnets have the disadvantage of producing large amounts of heat at high magnetic fields due to the dissipation of power in the coils. An efficient water cooling has therefore to be employed. Resistive magnets are suitable for experiments which require high magnetic fields without having too high demands for the field homogeneity and the noise level, which is for the most parts induced by vibrations caused by the water cooling of the magnets.

At Grenoble High Magnetic Field Laboratory, two different kinds of coils are used, so-called *Bitter coils* and *polyhelix coils*. The *Bitter coil* was invented by F. Bitter [54]. It consists of copper discs which are stacked one above the other. Insulating sheets between the copper discs are arranged in such a manner that the electrical current passes on a helical path through the coil. For the water cooling of the coil, holes are drilled vertically through the whole construction. While Bitter magnets are mechanically stable, relatively easy to build and easy to cool efficiently, they are restricted by their design to a specific geometry. This disadvantage is overcome by the *polyhelix coil* [55], which is constructed by removing material of a copper tube along a helicoidal line by spark erosion. As this technique allows variations of the conductor thickness, the polyhelix coil allows to produce considerably higher magnetic fields than the Bitter coil for the same electric power and magnet volume. However, they are much more difficult to be designed and constructed than Bitter coils.

For the high field experiments described in this work (Chapter 6), we used a resistive magnet of the Grenoble High Magnetic Field Laboratory. The magnet consists of an outer Bitter magnet with a polyhelix insert. It produces a maximum field of $B = 28$ T, which is well above the state-of-the-art technology for superconducting magnets ($B \approx 22$ T). The nominal power consumption of this magnet at full field is 20 MW. Further technical information about this magnet can be found in Ref. [56].

4.3 Cryogenics

Measurements were performed in three different cryogenic systems: First, a variable temperature insert (VTI) with a base temperature of $T_b \approx 1.2$ K. Second, a ^{3}He cryostat with $T_b \approx 300$ mK. Third, two dilution fridges with $T_b \approx 10$ mK (superconducting magnet) and $T_b \approx 30$ mK (resistive magnet). A detailed discussion of the cryogenic systems is given in the Appendix A.2.

4.4 Magnetotransport measurements

A schematic sketch of the magnetotransport circuit is depicted in Fig. 4.2. The contacts are positioned in a Hall-bar configuration. An ac-current is passed through the current contacts (1 - 2) at each end of the sample. The current is generated using the oscillator of the lock-in amplifier. We typically used a voltage of $V = 0.1$-1 V with a frequency $f \approx 10$ Hz, which was also used as reference frequency for the phase sensitive detection of the signal. The current flow through the sample is controlled by a large-ohmic series-resistor R_1 ($R_1 = 10$ kΩ-1 MΩ), with R_1 being much bigger than the resistance of the sample. This assures that even if the magnetoresistance of the sample is changed considerably during the measurements, the current through the sample (typically $I \approx 1$ μA) does not change noticeably.
The longitudinal and transverse voltage drops U_{xx} and U_{xy} caused by the resistivity of the sample are measured between the contacts (3-4) and (4-5), respectively. Both signals are amplified by a factor of 100 using pre-amplifiers placed close to the top of the probe. The pre-amplified signals are then sent to the lock-in amplifier. The phase sensitive detection employed in the lock-in amplifier processes only signals with the reference frequency and a given phase θ ($\theta = 0$ for resistive signals and $\theta = \pm\pi/2$ for inductive or capacitive signals), i.e., noise signals which typically have different frequencies and phases are rejected. The lock-in signals are then read by the computer and converted to resistances.

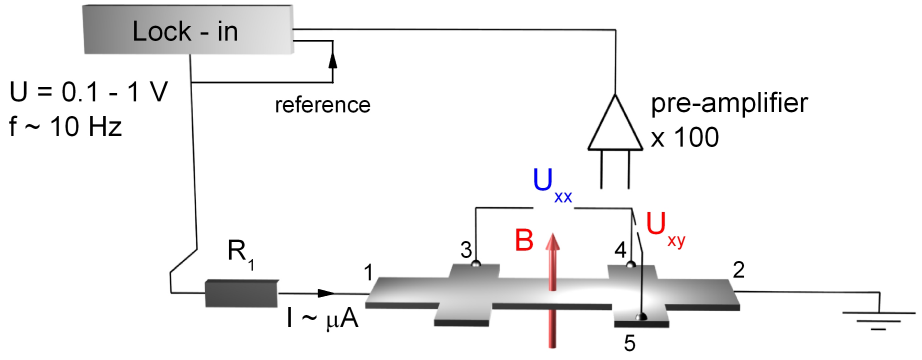

Fig. 4.2: *Schematic of the electrical setup used to measure magnetotransport.*

4.5 de Haas-van Alphen effect measurements

The de Haas-van Alphen effect measurements were carried out using the so-called *torque method*. The torque method is based on the fact that if a sample exhibits a magnetization **M** when exposed to an external magnetic field **B**, a torque $\boldsymbol{\tau}$ is created in the direction perpendicular to **M** and **B**,

$$\boldsymbol{\tau} = \mathbf{M} \times \mathbf{B}. \tag{4.1}$$

The dependence of the torque on the cross product of the magnetization and the magnetic field implies that the torque method requires a component of **M**, which is perpendicular to the magnetic field. Otherwise the torque $\boldsymbol{\tau}$ is zero.

With the oscillatory magnetization perpendicular to the magnetic field given by the Lifshitz-Kosevich formula (2.21) the absolute value of the torque $\tau = M_{\perp}B$ ($\tau = M_{\parallel}B = 0$) reads

$$\tau = -\frac{1}{B_F}\frac{dB_F}{d\theta}M_{\parallel}B, \tag{4.2}$$

with B_F being the fundamental frequency related to an extremal cross section of the Fermi surface. Eq. (4.2) implies that the detection of de Haas-van Alphen oscillations by means of the torque technique requires a non-spherical Fermi surface with $dB_F/d\theta \neq 0$. As discussed in Chapter 3.1.3 this condition is fulfilled by the Fermi surface of graphite.

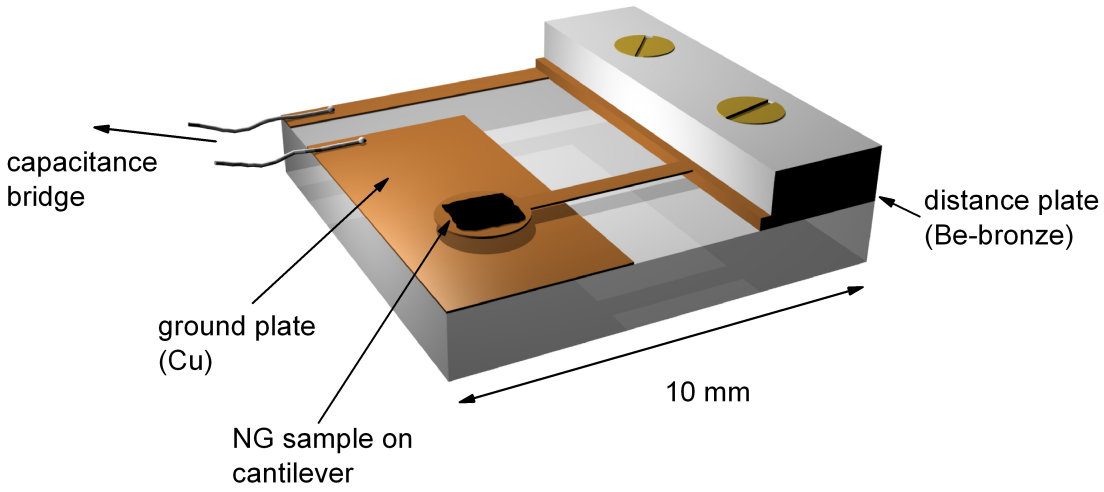

Fig. 4.3: *Sketch of the capacitive torquemeter. The graphite sample is mounted on the circular plate with vacuum grease. Changes of the magnetization of the sample lead to variations of the torque on the cantilever and therefore to changes of the distance between the spring and the ground plate. The induced variations of the capacitance are detected by a capacitance bridge (Fig. 4.4).*

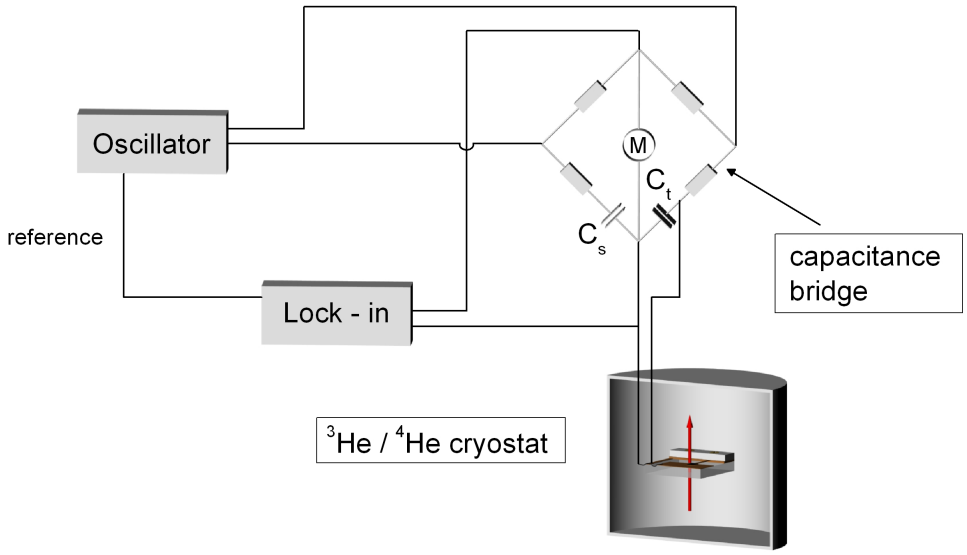

Fig. 4.4: *Schematic sketch of the electrical circuit used to measure the capacitance of the capacitive torquemeter, C_t. At zero magnetic field the capacitance bridge is balanced by changing the capacitance C_s until $M = 0$ V. The voltage induced in the circuit due to changes of the magnetization of the sample is sent to a lock-in amplifier.*

The torque of the sample was measured by using a capacitive torquemeter. The principal experimental setup is sketched in Fig. 4.3. The capacitor consists of a copper ground plate and a plane-parallel circular plate made of copper-beryllium with a diameter of 2.5 mm. The graphite sample is mounted on the circular plate with vacuum grease. The circular plate itself is connected by a narrow cantilever beam to the rectangular plate. Two different cantilevers with the dimensions (length×width×thickness) 5 mm × 125 μm × 125 μm (cantilever A) and 5 mm × 125 μm × 50 μm of (cantilever B) were used. The rectangular plate is fixed to the sample holder which is separated from the ground plate by a distance plate with a thickness of $d = 50$ μm.

When a magnetic field is applied and the sample is subject to a torque, the cantilever acts as a spring. The deformation of the spring leads to a change of the distance between the spring and the ground plate and hence to a change of the capacitance. For small excitations of the spring, the variation of the capacitance is proportional to the torque. The amplitude of the deformation depends on the dimensions of the cantilevers. With the cantilever A being more rigid, it is also less sensitive to small changes of the magnetization of the sample.

The capacitance and therefore the torque was measured using a precision capacitance bridge and standard lock-in technique. The setup is depicted in Fig. 4.4. A 5.27 kHz excitation voltage with an amplitude of 40 V generated by an oscillator is coupled to a circuit with the capacitance of the torquemeter C_t connected in series with a tunable capacitance C_s of the capacitance bridge. At the

beginning of each measurement at $B = 0$ T the bridge is balanced until a zero reading is seen on the meter M ($R_1 C_s = R_2 C_t$). In a magnetic field sweep the variations of the torquemeter capacitance are detected by measuring the amplitude of the voltage induced in the circuit. The induced voltage is sent to a lock-in amplifier, with the reference signal coming from the oscillator.

For the de Haas-van Alphen measurements in tilted field configuration, the torquemeter was mounted in a dilution fridge onto a rotation holder.

5 Low field magnetotransport: Orbital effects

Résume du chapitre

Dans cette thèse nous présentons les premières mesures de magnétotransport du graphite effectuées dans la gamme de température des millikelvin ($T \approx 10$ mK). Le spectre du magnétotransport du graphite naturel mesuré à ces températures est extrêmement riche. Après l'extraction d'un large fond de magnétorésistance, deux séries d'oscillations quantiques superposées peuvent encore être observées à des champs magnétiques très bas ($B_0 \approx 0.07$ T). L'analyse de Fourier des oscillations donne $B_F = 4.75$ T et $B_F = 6.58$ T pour les deux fréquences fondamentales. Dans le modèle SWM les deux fréquences sont assignées aux trous et aux électrons majoritaires. Les valeurs de phase des deux oscillations correspondent aux valeurs prédites par le modèle SWM du graphite. Nous avons confirmé la validité du modèle SWM par des calculs numériques détaillés de la structure de bande. Le mouvement de l'énergie de Fermi a été calculé d'une manière auto-cohérente en supposant que la somme des concentrations des électrons et des trous est constante.
La recherche systématique des oscillations de porteurs minoritaires aux faibles champs magnétiques ($B < 0.3$ T) s'est avéré infructueuse. En ce qui concerne le fond de magnétorésistance, nous avons effectué quelques mesures en fonction de la température à champ magnétique fixe pour confirmer la transition métal-isolant récemment découverte dans le graphite [25].

In this chapter we report on low field magnetotransport studies of graphite measured at various temperatures. To begin with, we present measurements on HOPG at $T \approx 1.2$ K, which are comparable to previously published data [9–11,57,58]. We then show that magnetotransport measurements performed at mK temperatures ($T = 10$ mK) reveal much richer magnetotransport spectra both for HOPG and natural graphite. The extremely high quality of the mK magnetotransport data of natural graphite allows a precise phase/frequency analysis and therefore the extraction of detailed information about the Fermi surface of graphite. By performing band structure calculations we demonstrate that the quantum oscillations can be consistently interpreted with the presence of majority electron and hole pockets within the three-dimensional SWM band structure model for

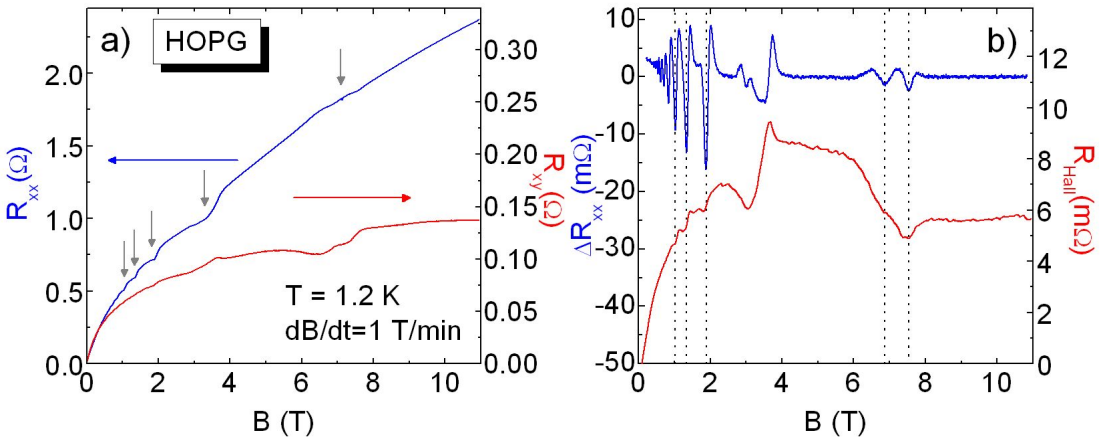

Fig. 5.1: ***a)*** *The longitudinal (R_{xx}) and transverse (R_{xy}) resistances of HOPG as a function of the magnetic field ($T = 1.2$ K). In the signal $R_{xx}(B)$ a large magnetoresistance background and small quantum oscillations (arrows) are superimposed. The similarity of $R_{xy}(B)$ and $R_{xx}(B)$ can be explained by a strong mixing of the Hall resistance $R_{Hall}(B)$ with $R_{xx}(B)$.* ***b)*** *(Upper curve) Background removed signal of R_{xx}, ΔR_{xx}. Two series of quantum oscillations are superimposed. (Lower curve) Hall resistance R_{Hall} with plateau like features at low magnetic field.*

graphite. The observed significant deviations of the quantum oscillations from the $1/B$ periodicity at high magnetic fields ($B > 2$ T) are explained by a movement of the Fermi energy as the quantum limit is approached. This seriously questions the validity of using the high field data to extract the phase of the Shubnikov-de Haas oscillations and hence the nature of the charge carriers [59]. At the end of the chapter the appearance of a possible minority carrier related series of features at low magnetic fields is discussed.
Some of the results presented in this chapter are published in [J. M. Schneider *et al.*, Phys. Rev. Lett., **102**, 166403 (2009)] and [J. M. Schneider *et al.*, Phys. Rev. Lett., **104**, 119702 (2010)].

5.1 Magnetoresistance measurements

5.1.1 Magnetotransport of HOPG at *T*=1.2 K

Fig. 5.1 a) shows typical magnetotransport data of the longitudinal (R_{xx}) and transverse (R_{xy}) resistances of HOPG measured at $T = 1.2$ K in the magnetic field range $B = 0 - 11$ T (sweep rate $dB/dt = 1$ T/min). The magnetic field was oriented perpendicular to the a-b plane ($B \,||\, c$).

Having a small value at $B = 0$ T, $R_{xx}(B)$ (blue curve) strongly increases with the magnetic field. At $B = 11$ T, the magnetoresistance is about two orders of magnitude larger than the zero-field value. The origin of the large magnetoresistance in graphite remains unclear and is subject of an ongoing

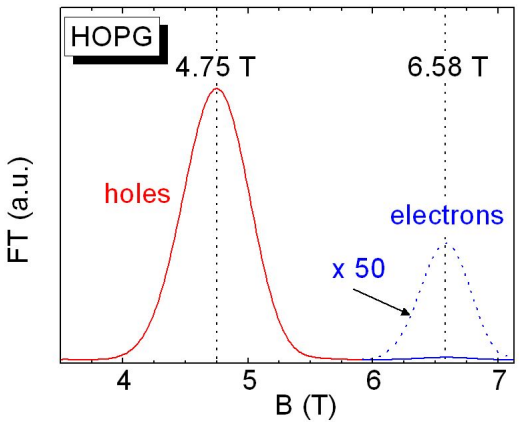

Fig. 5.2: *Spectral intensity of the Fourier transform $|F(B)|$ of the background removed data $\Delta R_{xx}(1/B)$. The two types of oscillations, ascribed to holes and electrons, have the frequency values $B_{F,h} = 4.75 \pm 0.1$ T and $B_{F,e} = 6.58 \pm 0.1$ T.*

debate [60–63].

For magnetic fields $B > 0.5$ T, small quantum oscillations are superimposed on the signal (arrows). In order to analyze these oscillations, the large magnetoresistance-background has to be removed. The background can be removed either by subtracting a smoothed (moving window average) data curve or by numerically calculating the second derivative d^2R/dB^2. Both techniques give similar results, and here we use averaging to remove the background. The background-removed resistance ΔR_{xx} is displayed in Fig. 5.1 b) (blue curve). At low magnetic fields, pronounced Shubnikov-de Haas oscillations are observed. At higher magnetic fields, a second series of smaller oscillations is found. The Shubnikov-de Haas oscillations are periodic as a function of the inverse magnetic field so that the fundamental frequencies of these oscillations can be obtained by making a Fourier transformation of $\Delta R_{xx}(1/B)$. The result is displayed in Fig. 5.2. It shows the spectral intensity of the Fourier transform $|F(B)|$ as a function of the magnetic field. The frequencies of the oscillations are given in units of the magnetic field, the intensity is given in arbitrary units. Two main features are observed. The feature with the larger amplitude is found at $B_F = 4.75 \pm 0.01$ T. The second feature with a much smaller amplitude (dotted line: multiplied by a factor of 50 for illustration reasons) is found at $B_F = 6.58 \pm 0.01$ T. In the SWM-model, the two frequencies at $B_F = 4.75$ T and $B_F = 6.58$ T are assigned to majority holes and electrons, respectively.

The transverse resistance in Fig. 5.1 b), R_{xy} (red curve), shows a similar behaviour as R_{xx}, i.e., it reveals a large magnetoresistance on which quantum oscillations are superimposed. The Hall resistance R_{Hall}[1] is mixed with R_{xx} due to the imperfect geometry of the contacts. This could mean that the contacts are not positioned in an exact Hall-bar geometry, as the indium dots are simply placed at the edges of the graphite sample. When the Hall contacts are slightly shifted in x-direction, there is always a contribution of R_{xx} in the measured Hall resistance. This is especially

[1] The Hall resistance is referred to as R_{Hall}, whereas the measured transverse resistance is called R_{xy}.

true in graphite, since $R_{xx} \gg R_{Hall}$ as shown in the following.

Nevertheless, since the resistance R_{xx} is an even function of the magnetic field and R_{Hall} is an odd function of the magnetic field (Appendix A.1), the contribution of R_{xx} to the Hall resistance can in principle be removed by subtracting the R_{xy} data measured for the two different polarizations of the magnetic field,

$$R_{Hall} = \frac{1}{2}\left(R_{xy}(B+) - R_{xy}(B-)\right) . \tag{5.1}$$

The Hall-resistance R_{Hall} (red curve) is plotted in Fig. 5.1 b) as a function of the magnetic field for $B = 0 - 10$ T. Oscillatory features are observed which for $B < 2$ T resemble quantum Hall plateaus. Indeed in Refs. [59, 64] these features were – in our opinion incorrectly – interpreted as quantum Hall plateaus. This interpretation follows from the "two-dimensional model" of graphite, i.e., graphite is considered to consist of uncoupled graphene layers. However it is in contradiction with the three-dimensional SWM-model, as for the observation of plateau like features a gap in the density of states is required which does not occur in three-dimensional systems. The "Hall plateaus" are probably a remaining artefact of oscillations observed in R_{xx}.
The fact that a Hall resistance is observed in graphite, leads to the conclusion that there is a difference in the charge carrier densities of electrons and holes. In the *extreme quantum* limit $(\mu_{e,h}B \gg 1)$ the non-diagonal component of the magnetic conductivity tensor is given by (see Eq. (A.6) in the Appendix)

$$\rho_{xy} = \frac{B}{e\,(n_h - n_e)}. \tag{5.2}$$

The value of ρ_{xy}/B is therefore determined only by the difference of the electron and hole concentrations, i.e., the magnitude of the imbalance $\Delta n = n_h - n_e$. Considering that in a perfect graphite crystal the electron and hole concentrations are equal, the imbalance occurs from ionized donor (n_s^+) and acceptor (n_s^-) scattering centres due to defects in the graphite lattice. However, there is no straightforward way to extract the density Δn from the Hall resistance in graphite [28].

At *low (non-quantizing) magnetic fields* $(\mu_{e,h}B \ll 1)$ the transverse resistivity is given by (Eq. (A.7) in the Appendix)

$$\rho_{xy} = \frac{B}{en}\frac{\mu_h - \mu_e}{\mu_h + \mu_e}. \tag{5.3}$$

Extracting the slope from $\rho_{xy} = R_{Hall} \cdot wt/l$ of the $B < 0.5$ T data in Fig. 5.1 b), with w, t and l being the sample dimensions (see Section 4.1), yields $\rho_{xy}/B \approx 0.85\ \mu\Omega m/T$, which is comparable to the value obtained in Ref. [65]. With the carrier density of $n = 3 \times 10^{18}$ cm^{-3} [66], we obtain $\mu_h \approx 2\mu_e$. The higher hole mobility explains the larger amplitude of the hole spectral intensity in Fig. 5.2.

5.1.2 Temperature dependence of quantum oscillations

Fig. 5.3 shows the result of temperature dependent magnetotransport measurements performed on HOPG. In Fig. 5.3 a) the background removed signal ΔR_{xx} is given as a function of the magnetic field from $B = 0.6 - 1.8$ T for different temperatures in the range $T = 1.17 - 10.1$ K. For each curve the background was removed as previously by subtracting a smoothed data curve, using every time the same number of points for the moving window averaging. The amplitudes of ΔR_{xx} are significantly larger for low temperatures than for high temperatures. The features which are further analyzed are labelled *f1*, *f2* and *f3*. The temperature dependence of the amplitudes of these three features is displayed in Fig. 5.3 b).

If the temperature dependence of the quantum lifetime τ is neglected, the temperature dependence of the quantum oscillations is given by the temperature factor $R_T(T)$ in the Lifshitz-Kosevich formula

$$R_T(T) = \frac{\alpha \frac{m^*}{m_e}\frac{T}{B}}{\sinh\left(\alpha \frac{m^*}{m_e}\frac{T}{B}\right)} \quad \text{with} \quad \alpha = \frac{2\pi^2 k_B m_e}{\hbar e}, \tag{5.4}$$

which arises from the smearing out of the Fermi Dirac distribution at finite temperature. The dotted lines in Fig. 5.3 show that the temperature dependence of the amplitudes can be well reproduced with $R_T(T)$ alone, confirming our *a priori* neglect of the temperature dependence of the quantum lifetime τ. The values of m^* obtained from the fitting procedure, given in the inset of Fig. 5.3 b), are $m^*_{f1} = 0.051 \pm 0.002$, $m^*_{f2} = 0.050 \pm 0.002$ and $m^*_{f1} = 0.053 \pm 0.005$. Within experimental

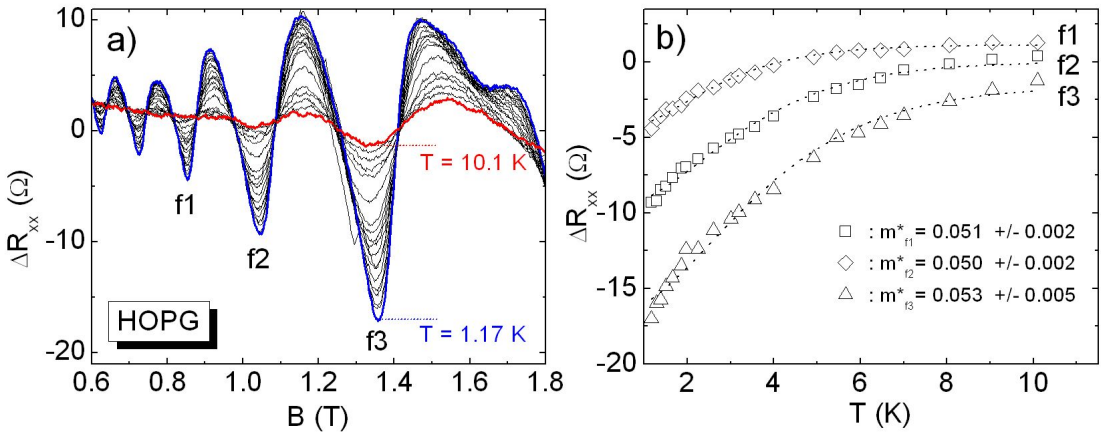

Fig. 5.3: ***a)*** *ΔR_{xx} as a function of the magnetic field in the range $B = 0.6 - 1.8$ T for different temperatures between $T = 1.17$ K and 10.1 K. The absolute values of the amplitudes of the quantum oscillations decrease with increasing temperatures.* ***b)*** *The amplitudes ΔR_{xx} of the features f1, f2 and f3 as a function of the temperature. The dotted curves correspond to fits with the temperature factor $R_T(T)$ of the Lifshitz-Kosevich formula. The fitting parameter effective mass has the value $m^* \approx 0.05$.*

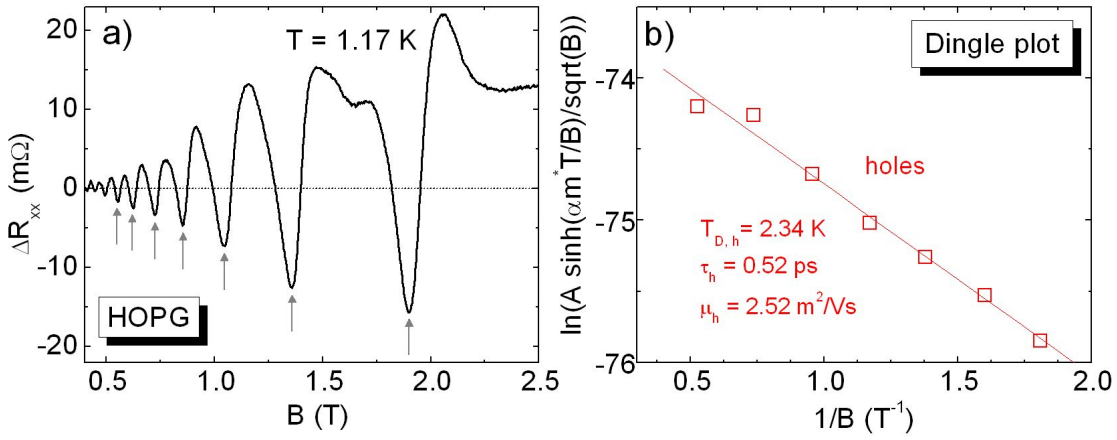

Fig. 5.4: ***a)*** *ΔR_{xx} measured at $T = 1.17$ K for $B = 0.4 - 2.5$ T. The features which are further analyzed are marked by arrows.* ***b)*** *Dingle plot using the effective mass of holes $m^* = 0.039$ [28]. The linear fit yields the Dingle temperature $T_{D,h} = 2.34 \pm 0.1$ K and the quantum lifetime $\tau_h = 0.52 \pm 0.1$ ps. The mobility value $\mu_h = 2.52 \pm 0.3$ m^2/Vs is similar to mK mobilities reported recently on HOPG [65].*

error these values are almost identical to the accepted value of $m^* = 0.054$ for electrons found by means of cyclotron resonance measurements [51]. The spectral intensity plot of the Fourier transform (Fig. 5.2), however, suggests that the investigated features are due to holes. Their effective mass is $m^* = 0.039$ [28], which is about 25% smaller than the value found here.

With the value of the effective mass m^*, the quantum lifetime τ can be extracted from the field dependence of the Shubnikov-de Haas oscillations. In Fig. 5.4 a) we show ΔR_{xx}, which was measured at $T = 1.17$ K. The features which are further analyzed are marked by arrows. In Fig. 5.4 b) we plot $\ln\left[A \times \sinh(\alpha m^* T/B) T^{-1} B^{-1/2}\right]$ vs. $1/B$, with A being the amplitudes of the oscillations. According to the Lifshitz Kosevich behaviour, the slope $a = -\alpha m^* T_D$ yields the Dingle temperature $T_D = \hbar/(2\pi k_B \tau)$ and is a measure of the quantum lifetime τ. Here we have used the accepted mass $m^* = 0.039$ for holes. The Dingle temperature and the quantum lifetime are $T_{D,h} = 2.34 \pm 0.1$ K and $\tau_h = 0.52 \pm 0.4$ ps. If we assume that the value of τ is the same as the momentum relaxation time, we can extract the hole mobility $\mu_h = e\tau/m_h^*$. The value $\mu_h = 2.52 \pm 0.3$ m^2/Vs is similar to the mK mobilities reported recently on HOPG [65]. Moreover, knowing that the oscillations start at $B_0 \approx 0.4$ T the mobility can be estimated using $\omega_c \tau = \mu B_0 = 1$, which is the condition for the oscillations to be observed. $\mu = 2.5$ m^2/Vs is nearly identical with the value extracted from the Dingle plot.

5.1.3 Temperature dependence of the magnetoresistance

For the sake of completeness, the temperature dependence of the large background magnetoresistance is presented in this section. In 1999 the magnetic field induced metal-insulator-transition

(MIT) was discovered in the magnetoresistance of graphite [25], i.e., the longitudinal resistance R_{xx} as a function of the temperature shows a transition from a metal-like behaviour ($dR/dT > 0$) at low magnetic fields to an insulator-like behaviour ($dR/dT < 0$) at higher magnetic fields. If the magnetic field is further increased, the metallic state reappears (reentrant metallic behaviour) [67].

The existence of the reentrant metallic behaviour of graphite is already observed in the raw data of the temperature dependence of the quantum oscillations (previous section). Fig. 5.5 a) shows the resistance R_{xx} of HOPG as a function of the magnetic field ($B = 0 - 10$ T) for temperatures from $T = 1.17$ K (blue curve) to $T = 14.15$ K (red curve). The insets show details of the temperature dependence at $B = 10$ T, $B = 5$ T and $B = 0.2$ T (marked by the vertical dotted lines). At these magnetic fields, no quantum oscillations are observed.

In Fig. 5.5 b) the amplitudes of R_{xx} for the magnetic fields $B = 10$ T, $B = 5$ T and $B = 0.2$ T are plotted as a function of the temperature. The temperature dependence of the $B = 10$ T features is given by open squares (□), that of the $B = 5$ T features (multiplied by a factor of 1.56) by triangles (△) and that of the $B = 0.2$ T features (multiplied by a factor of 15.6) is given by circles (○).

For low magnetic fields ($B = 0.2$ T), a pure insulator-like temperature dependence is observed ($dR/dT < 0$). For higher fields ($B = 5$ T and $B = 10$ T), the resistance increases ($dR/dT > 0$) and then decreases ($dR/dT < 0$) with increasing temperature, i.e., graphite reveals a reentrant metallic behaviour.

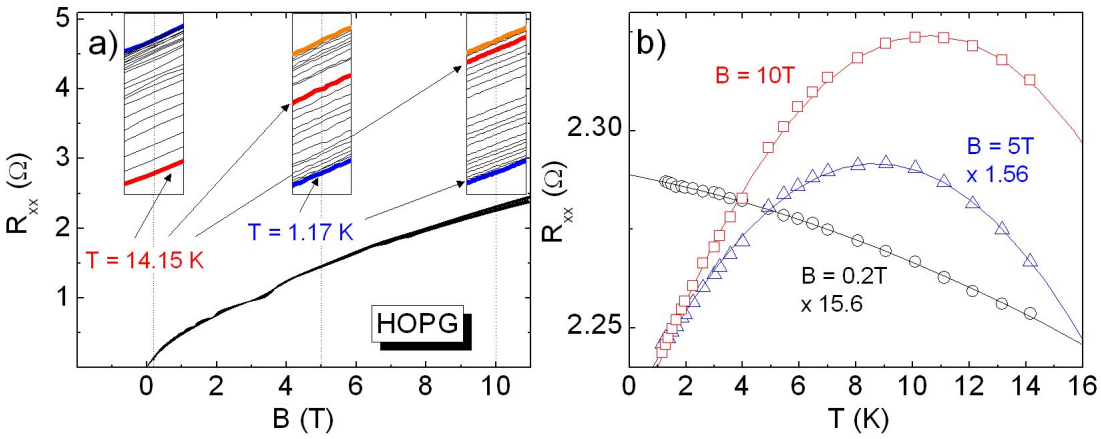

Fig. 5.5: ***a)*** *R_{xx} as a function of the magnetic field for temperatures from $T = 1.17$ K to 14.15 K. The magnetic fields, at which the temperature dependence of the magnetoresistance is further analyzed, are marked by vertical dotted lines ($B = 10$ T, $B = 5$ T and $B = 0.2$ T). Details of their temperature dependence are given in the insets.* ***b)*** *Temperature dependence of R_{xx} for given magnetic fields. The data of the $B = 0.2$ T and $B = 5$ T data points are multiplied by a factor of 15.6 and 1.56, respectively. For the high field features, $R_{xx}(T)$ reveals a reentrant metallic behaviour.*

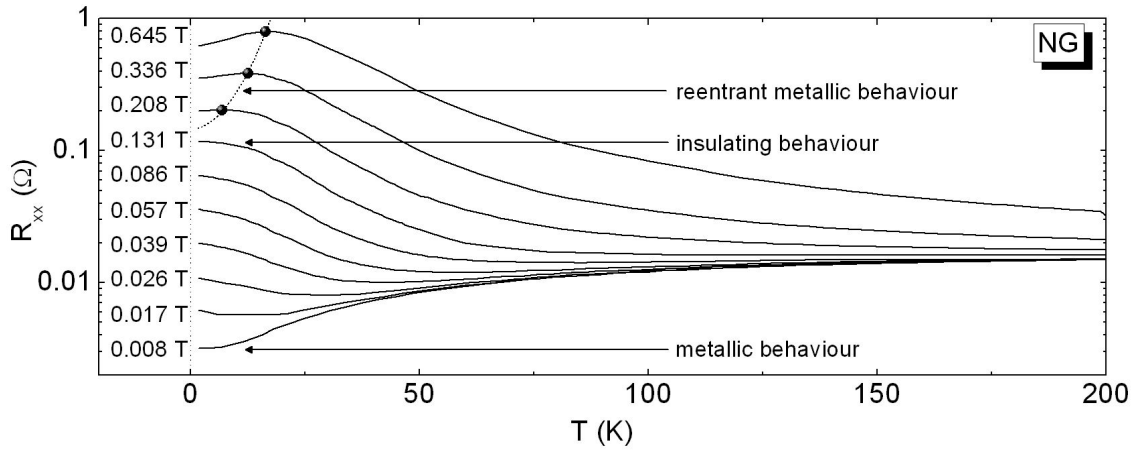

Fig. 5.6: *Longitudinal resistance R_{xx} (log-scale) as a function of the temperature ($T = 1.5 - 200$ K) measured for given magnetic fields. The metallic behaviour observed for low magnetic fields ($B = 8$ mT) is suppressed when the magnetic field is increased and for $B = 0.131$ T $R_{xx}(T)$ behaves like an insulator, i.e., between these two magnetic field values, graphite undergoes a metal-insulator-transition. For $B > 0.2$ T, $R_{xx}(T)$ reveals a reentrant metallic behaviour.*

The metal-insulator-transition is studied in detail for natural graphite at low magnetic field in the temperature range $T = 1.5$ - 200 K . The result is shown in Fig. 5.6. The resistance R_{xx} (note the log-scale) as a function of the temperature is plotted for given magnetic fields from $B = 8$ mT to $B = 0.645$ T. For $B = 8$ mT, $R_{xx}(T)$ reveals a pure metallic behaviour. When the magnetic field is increased, the metallic state is continuously suppressed and at $B = 0.131$ T, $R_{xx}(T)$ behaves like an insulator, i.e., between these two magnetic field values, graphite undergoes a metal-insulator-transition. When the magnetic field is further increased ($B > 0.2$ T), the metallic state reappears (indicated by dots (•) and the dotted line in Fig. 5.6).

The appearance of the metal-insulator-transition in graphite is poorly understood. According to Du *et al.* [62] the unusual temperature dependence can be described qualitatively by a two band model. Detailed theoretical discussions of the metal-insulator transition in graphite can be found in the literature and include the creation of a dynamical mass due to interactions between Dirac fermions, which can manifest itself as a metal-insulator-transition [68, 69], superconducting correlations in the quantum limit [70], and a field induced Luttinger liquid [71].

5.2 Ultra low temperature magnetotransport measurements

Before discussing the mK magnetotransport data, we show that the quality of the magnetotransport spectrum is considerably improved when cooling the sample from $T = 1$ K to mK temperatures. Fig. 5.7 a) shows R_{xx} of a natural graphite sample as a function of the magnetic field for different temperatures between $T = 10$ mK and $T = 1$ K. The different curves have been offset by $\Delta R = 1\ \Omega$ for clarity. The amplitudes of the quantum oscillations diminish with increasing temperature. This is clearly seen for the spin split features in the magnetic field range $B = 6 - 8$ T (marked by an arrow). The temperature dependence of the quantum oscillations can again be studied more systematically in the background removed data ΔR_{xx}, which is shown in Fig. 5.7 b). For illustration reasons the magnetic field region is limited to $B \approx 0.6 - 0.8$ T. In the inset the amplitudes of the 0.7 T features (marked by a vertical line) are shown for the different temperatures, with the absolute value of the amplitude increasing by more than 40% when cooling down from $T = 1$ K to $T = 10$ mK.

Fig. 5.8 shows the magnetotransport data of a second natural graphite sample measured at $T \approx 10$ mK. The raw data of $R_{xx}(B)$ for $B = 0 - 10$ T are shown in Fig. 5.8 a). As for HOPG at higher temperatures, $R_{xx}(B)$ increases roughly linearly with the magnetic field, and, at $B = 10$ T, it is about three orders of magnitude larger than the zero-field value. The quantum oscillations which are superimposed on the large magnetoresistance can clearly be distinguished.

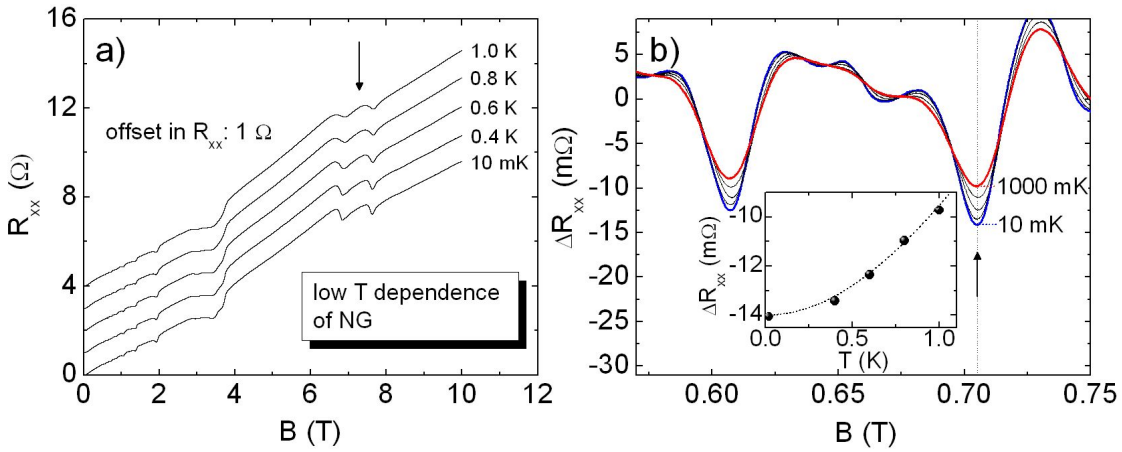

Fig. 5.7: ***a)*** *Low temperature dependence of $R_{xx}(B)$ between $T = 10$ mK and $T = 1$ K. The amplitudes of the quantum oscillations, superimposed on the large magnetoresistance, decrease with increasing temperature (arrow).* ***b)*** *Background removed signal $\Delta R_{xx}(B)$ for the different temperatures. The amplitudes of the quantum oscillations of the $B = 0.7$ T features (arrow) as a function of the temperature is shown in the inset. The absolute value of the amplitude increases by more than 40% when cooling down from $T = 1$ K to $T = 10$ mK.*

The extremely high quality of the data is revealed in the plots of the background removed data ΔR_{xx} (mΩ) (Figs. 5.8 a) - c)), for successively slower sweeps in order to reveal the quantum oscillations in the different magnetic field regions ($dB/dt = 0.05$, 0.01 and 0.001 T/min, respectively). As the oscillations are periodic in $1/B$, the optimal number of points used in the averaging depends upon the magnetic field region. For this reason, the amplitudes of the oscillations in Figs. 5.8 a) - c) should not be compared, as different averaging was used to remove the background. The oscillations start at $B_0 \approx 0.067$ T. Using again the condition $\omega_c \tau = \mu B_0 = 1$ to extract the mobility and the quantum lifetimes, we find $\mu = 15$ m^2/Vs and $\tau_e = 4.6$ ps, $\tau_h = 3.3$ ps for electrons and holes, respectively ($m_e^* = 0.054$ m$_e$ [51] and $m_h^* = 0.039$ m$_e$ [28]).

In the $\Delta R_{xx}(B)$ data two series of oscillations can clearly be distinguished. Spin splitting of the features (indicated by arrows) is observed for magnetic fields $B_z > 1$ T, which is considerably

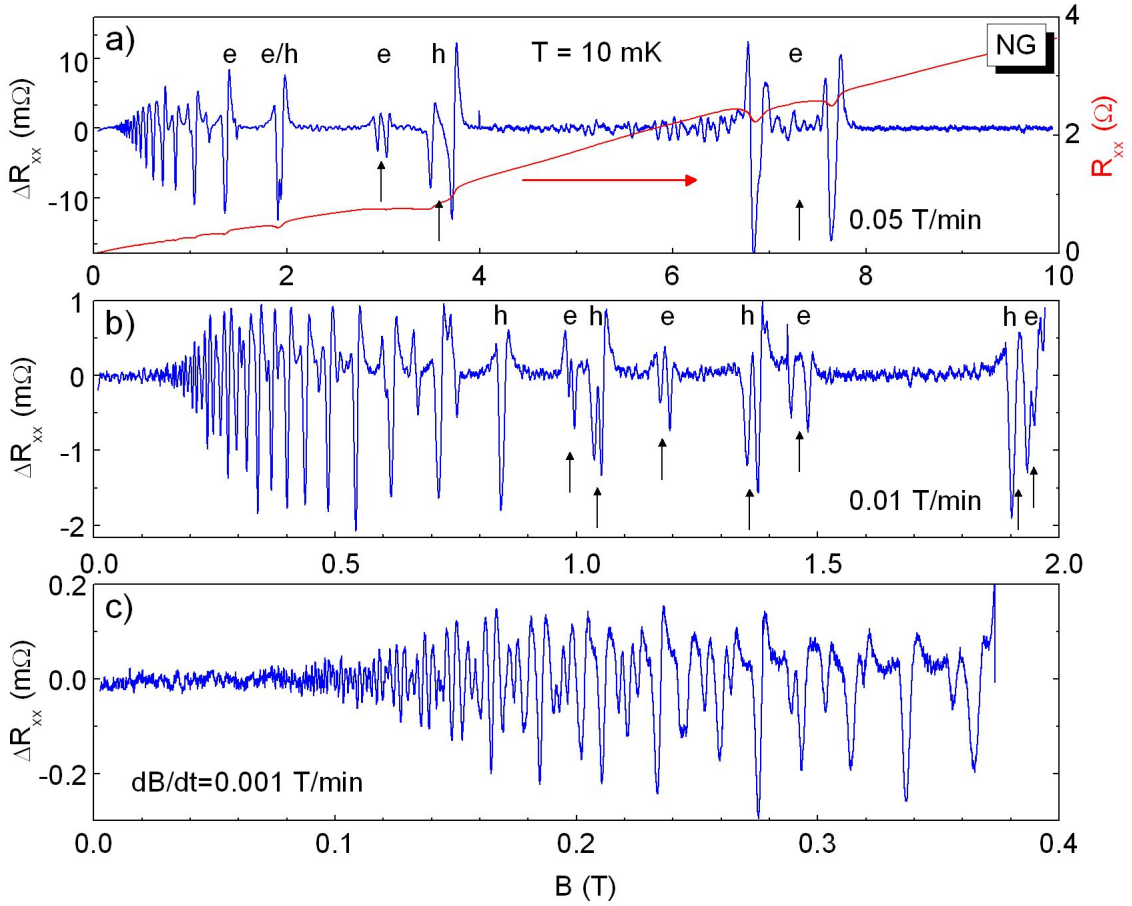

Fig. 5.8: ***a)*** *Right axis: Resistance R_{xx} vs. B measured at $T = 10$ mK for natural graphite.* ***a-c)*** *Left axis: Background removed data ΔR_{xx} over different magnetic field regions. The high field electron (e) and hole (h) features are indicated. The vertical arrows indicate spin split electron and hole features. Oscillations are observed for $B_0 > 0.07$ T.*

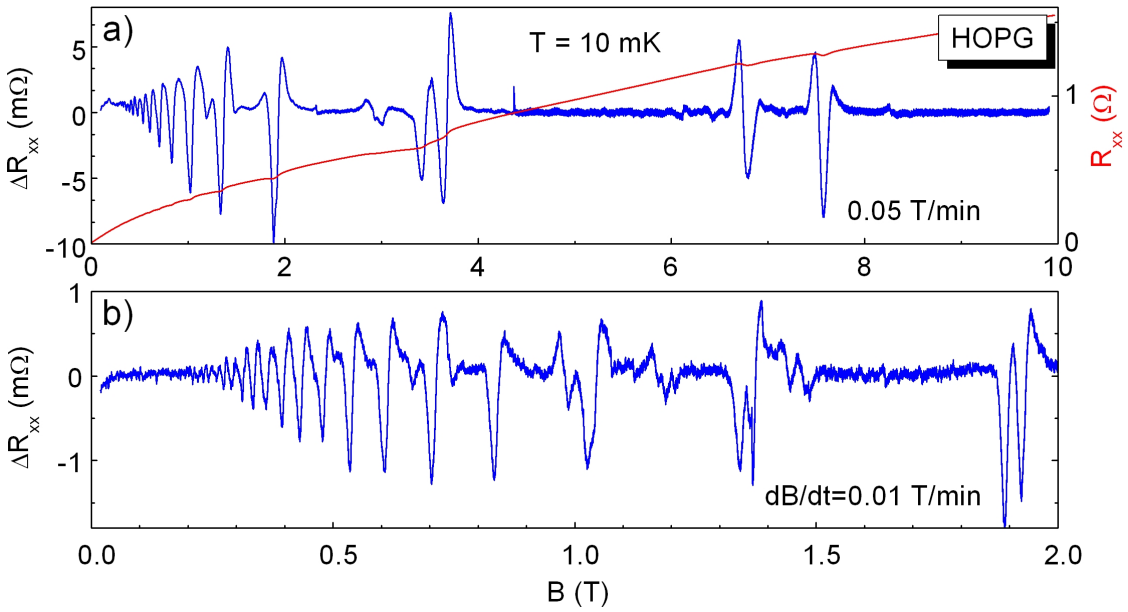

Fig. 5.9: ***a)*** *Right axis: Resistance R_{xx} vs. B measured at $T = 10$ mK for HOPG. R_{xx} increases linearly with the magnetic field, with the superimposed quantum oscillations being more distinct than in the higher temperature data (Fig. 5.1).* ***a)*** *and* ***b)*** *Left axis: Background removed data ΔR_{xx} showing quantum oscillations measured over different magnetic field regions with different sweep rates.*

lower than the magnetic field $B_z > 2$ T at which spin splitting was observed at higher temperatures ($T = 1.2$ K). The spin splitting of the features will be discussed in detail in Chapter 6 (see also Ref. [72]).

To compare natural graphite with HOPG, Fig. 5.9 shows the $T \approx 10$ mK magnetotransport data of HOPG. The raw data of $R_{xx}(B)$ for $B = 0 - 10$ T are shown in Fig. 5.9 a) (right axis). 5.9 a) and b) (left axis) show the background removed resistance ΔR_{xx} for different regions of the magnetic field ($dB/dt = 0.05$ and 0.01 T/min, respectively). The oscillations start at $B_0 \approx 0.25$ T, which corresponds to a mobility $\mu = 4$ m^2/Vs and the quantum lifetimes $\tau_e = 1.2$ ps, $\tau_h = 0.9$ ps. The positions of the features in magnetic field both of natural graphite and HOPG are essentially the same, which implies that HOPG and natural graphite have almost identical Fermi surfaces. This is in agreement with magneto-optical studies [33].

Nevertheless the quality of the natural graphite data is higher than that of HOPG. This can be seen when comparing the data of Fig. 5.8 b) and Fig. 5.9 b) for natural graphite and HOPG, respectively. Both data sets have been measured under the same conditions (sweep rate $dB/dt = 0.01$ T/min, $T = 10$ mK). In natural graphite the oscillations start at lower magnetic field ($B_0 \approx 0.16$ T in natural graphite vs. $B_0 \approx 0.22$ T in HOPG). Moreover, spin splitting is observed in natural graphite for more features. The better quality of the natural graphite data compared to the

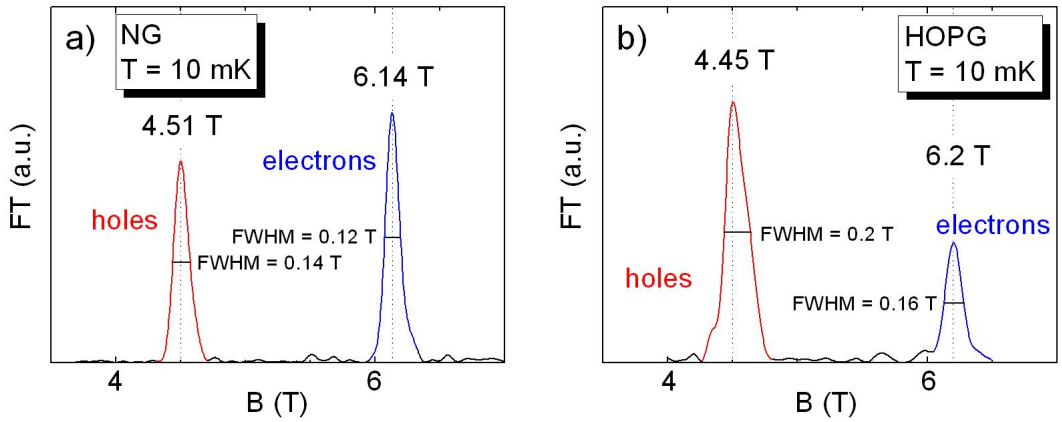

Fig. 5.10: *Spectral intensity of the Fourier transform $|F(B)|$ of the background removed data $\Delta R_{xx}(1/B)$ measured at mK temperature for **a)** natural graphite and **b)** HOPG. The frequencies of the electron and hole oscillations are very similar: $B_{F,h} \approx 4.45 \pm 0.05$ T and $B_{F,e} \approx 6.15 \pm 0.05$ T. The smaller broadening of the natural graphite peaks (Full width at half maximum (FWHM) indicated) results from the better quality of the data.*

HOPG data implies that natural graphite has less crystal defects than HOPG, as less crystal defects lead to a longer quantum lifetime τ and therefore to a reduced broadening $\Gamma = \hbar/\tau$ of the Landau bands. The reduced overlap of the Landau bands results in a lower onset magnetic field of the quantum oscillations.

Fig. 5.10 shows the spectral intensity of the Fourier transformation both for natural graphite and HOPG. Both types of bulk graphite show two distinct features with very similar frequencies. Note that at mK temperatures the hole and electron peaks have comparable amplitudes, in contrast to the $T = 1.2$ K data for which the electron peak is two orders of magnitude smaller. The better quality of the natural graphite data compared to the HOPG data reveals itself by "sharper" features (smaller broadening) and a higher intensity of the electron peak compared to the hole peak.

5.3 Phase/Frequency analysis of mK magnetotransport data

The large number of oscillations observed in the magnetotransport data for natural graphite at mK temperature can be exploited to make a detailed phase/frequency analysis of the quantum oscillations. Both parameters are crucial for the understanding of the topology of the Fermi surface.

The extraction of the phase and the frequency of the oscillations is based on the principle that when shifting a function from $f(B)$ to $f(B-B_0)$, a phase factor $e^{-i\varphi_0}$ is added to the Fourier transform, $\tilde{F}(B) = F(B-B_0) = F(B)e^{-i\varphi_0}$. Introducing the so-called phase shift function $K(\varphi,B) = \Re\left[e^{i\varphi}\tilde{F}(B)\right] = \cos(\varphi-\varphi_0)F(B)$, both the frequency B_F and the phase φ_0 can be detected simultaneously as the position of the maximum in the $\varphi - B$ plane [73]. $K(\varphi,B)$ is plotted in Figs. 5.11 b) and c) in the regions of the fundamental frequencies of the electrons and holes. From the maxima the determined frequencies and phases in units of 2π are $B_{F,h} = 4.51 \pm 0.1$ T, $\varphi_{0,h} = -0.43 \pm 0.1$ and $B_{F,e} = 6.14 \pm 0.05$ T, $\varphi_{0,e} = -0.28 \pm 0.1$ for holes and electrons, respectively.

With the oscillatory part of the magnetization given by

$$M_{osc} \propto \cos\left[2\pi\left(\frac{B_F}{B} - \gamma \pm \delta\right)\right], \tag{5.5}$$

with $\gamma = 1/2$ for massive charge carriers and $\gamma = 0$ or 1 for massless Dirac like carriers. The phase term δ reflects the curvature of the Fermi surface in the z-direction. It has the value $\delta = 0$ for a two-dimensional cylindrical Fermi surface. For a three-dimensional corrugated Fermi surface it

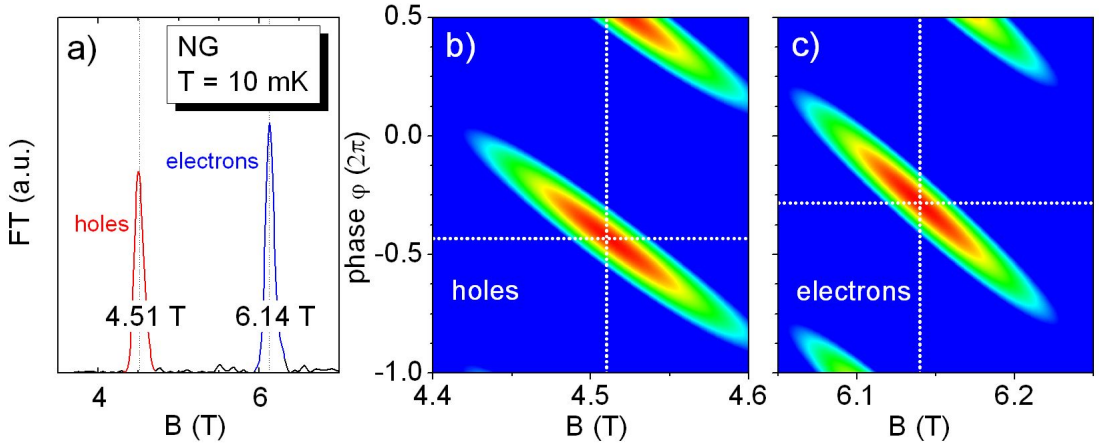

Fig. 5.11: ***a)*** *Spectral intensity of the Fourier transform $|F(B)|$ of the background removed data $\Delta R_{xx}(1/B)$ of natural graphite measured at mK temperature (Section 5.2). The electron and hole oscillations have frequencies of $B_{F,h} = 4.51 \pm 0.1$ T and $B_{F,e} = 6.58 \pm 0.1$ T.* ***b)*** *and* ***c)*** *Phase shift function $K(\varphi,B)$ in the $\varphi - B$ plane in the regions of the hole and electron features. The frequencies and phases of the oscillations are given by the maxima. $B_{F,h} = 4.51 \pm 0.1$ T, $\varphi_{0,h} = -0.43 \pm 0.1$ and $B_{F,e} = 6.14 \pm 0.05$ T, $\varphi_{0,e} = -0.28 \pm 0.1$ for holes and electrons, respectively.*

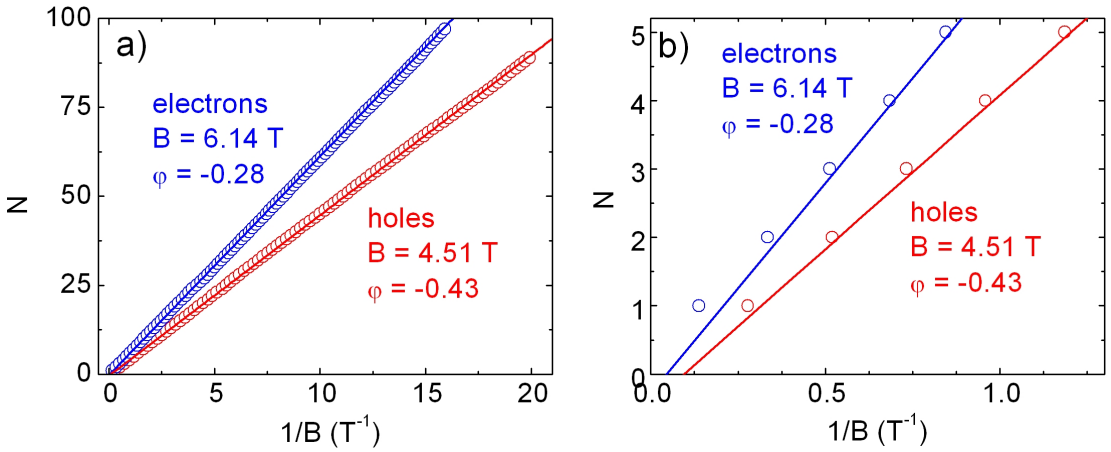

Fig. 5.12: *Orbital quantum number N as a function of the inverse magnetic field position of the minima in $\Delta R_{xx}(B)$ for* ***a)*** *$N < 100$ and* ***b)*** *$N \leq 5$. The solid lines are the expected linear dependence for the value B_F and the phase φ extracted from the phase shift function, giving a nearly perfect fit to the data. A clear deviation from the $1/B$ periodicity is seen in b) for the $N \leq 2$ features.*

has the value $\delta = \pm 1/8$, where the plus and minus sign correspond to minima and maxima cross sections, respectively. Note, however, that defining the phase values with respect to de Haas-van Alphen oscillations adds an additional phase term of $+\pi/2$ which can be incorporated in the value of δ. It has therefore the value $\delta = +1/8$ for maxima cross sections of the Fermi surface probed by Shubnikov-de Haas oscillations.

For the majority electrons and majority holes, the SWM-model predicts the phase values $\varphi = -\gamma + \delta = -0.375$. The phase values obtained from the phase shift function both for electrons and holes are in reasonable agreement with the phase values theoretically expected for massive three-dimensional charge carriers described in the SWM-model.

Another way of illustrating the frequency and phase values of the oscillations is the so-called *N vs. 1/B plot*. In graphite, we have experimentally $\rho_{xx} \gg \rho_{xy}$ (see Fig. 5.1 b)) so that the tensor relation for the conductivity (Eq. (A.4) in the Appendix) simplifies to give

$$\sigma_{xx} = \frac{\rho_{xx}}{\rho_{xx}^2 + \rho_{xy}^2} \propto \frac{1}{\rho_{xx}}. \tag{5.6}$$

Therefore, conductivity maxima which occur at coincidences of Landau bands and the Fermi energy E_F, correspond to minima in $\Delta R_{xx}(B)$ [8]. In Fig. 5.12 we show the positions of the minima in inverse magnetic field as a function of the orbital quantum number N, assigned to the electron and hole minima of $\Delta R_{xx}(B)$. For $N < 25$ the magnetic field positions of each series of oscillations can be determined directly from $\Delta R_{xx}(B)$. For $N > 25$, pass band frequency domain filtering was used to separate the superimposed electron and hole features. For both electron and hole features angular quantum numbers in the range $1 < N < 90$ (to almost $N = 100$ for electrons) are observed.

The solid lines in Fig. 5.12 correspond to $N = B_F/B + \varphi$ (with $\varphi = -\gamma + \delta$) with B_F and φ obtained from the phase shift function. They give a nearly perfect fit to the data at low magnetic fields, i.e., high quantum numbers N. However, for high magnetic fields (low quantum numbers N) there is a strong deviation from the $1/B$ periodicity, as shown in Fig. 5.12 b) for $1 \leq N \leq 5$. This deviation from the $1/B$ periodicity is due to an electron-hole cross talk, leading to a considerable movement of the Fermi energy as the quantum limit is approached [74]. The observed deviations from the $1/B$ periodicity at high magnetic fields means that the $T = 1.2$ K data with a very limited number of quantum oscillations cannot be used to extract the phase of the quantum oscillations.

5.4 SWM-model and the interpretation of quantum oscillations

In this section we demonstrate that the magnetotransport data of graphite can be fully understood within the frame work of the Slonczewski, Weiss and McClure (SWM) model. Before going into the details of the discussion, it is expedient to summarize the essential results of this model. Fig. 5.13 shows the Fermi surface calculated within the SWM-model. Note that the k_z-axis has been divided by a factor of about 5 for illustration reasons. The Fermi surface has two pockets: one hole pocket and one electron pocket, corresponding to the two types of oscillations observed in graphite. The frequency of the quantum oscillations in magnetic field is linked to the extremal cross section areas S of the Fermi surface perpendicular to the applied magnetic field (Eq. (2.11)),

$$\Delta\frac{1}{B} = \frac{2\pi e}{\hbar S}.$$

Consequently $B_F = \hbar\Delta S/2\pi e$. As the electron cross section ($k_z = 0$) is bigger than the hole cross section ($k_z \approx 0.3$), $S_e > S_h$ (see Fig. 5.13 a)), the oscillations with the higher fundamental frequency observed in the magnetotransport data are ascribed to electrons, whereas the oscillations with the smaller fundamental frequency are ascribed to holes.

For a more detailed analysis of the oscillations the band structure of graphite in a magnetic field has to be discussed. In Fig. 5.13 b) the calculated band structure for $B = 1.75$ T is shown ($\gamma_3 =$

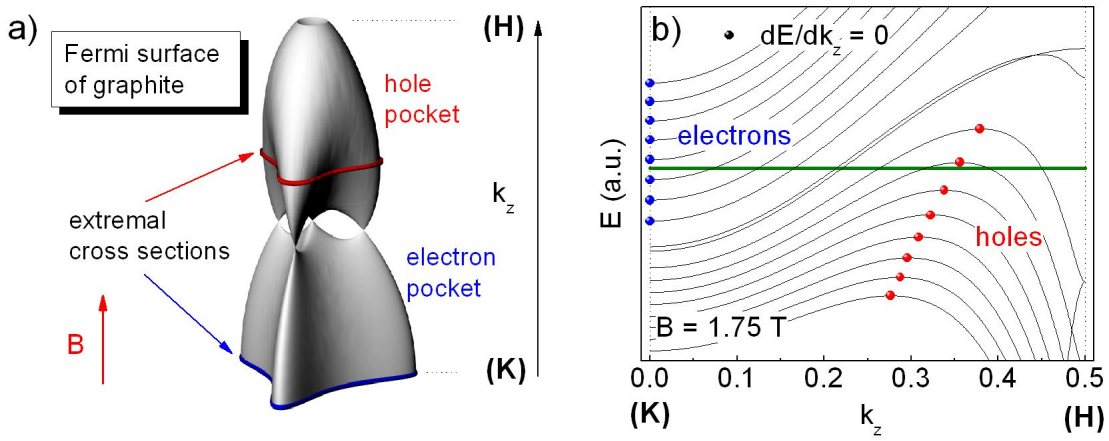

Fig. 5.13: ***a)*** *Fermi surface of graphite calculated within the SWM-model. The two oscillations observed in the magnetotransport data are due to electrons at the K point and holes close to the H point. The fundamental frequencies are linked to the extremal cross sections by $B_F = \hbar\Delta S/2\pi e$, i.e., the oscillations with the higher frequency are due to electrons and the oscillations with the smaller frequency are due to holes, as $S_e > S_h$.* ***b)*** *Band structure of graphite at $B = 1.75$ T as a function of k_z. The local extrema corresponding to maxima in the density of states are marked by dots (•).*

0). The bands are split into Landau bands. The energies of the electron bands decrease with decreasing magnetic field, while the energies of the hole bands increase with decreasing magnetic field. Consequently as the magnetic field is varied both the electron and hole bands cross the Fermi energy. Minima in ΔR_{xx} are observed when local minima or maxima of the bands, corresponding to the extremal cross sections of the Fermi surface (marked by dots (•) in Fig. 5.13 b)), cross the Fermi energy. This can be derived from the Einstein relation of the conductivity [75], which reads

$$\sigma_{xx} = e^2 \mathrm{DOS}(E_F) D, \tag{5.7}$$

with the conductivity being directly proportional to the diffusion constant D and the density of states at the Fermi energy $\mathrm{DOS}(E_F)$. The density of states of a band N is given by [41]

$$\mathrm{DOS_N} = \int_{S_N(E)} \frac{dS}{4\pi^3} \frac{1}{|\nabla E_N(\mathbf{k})|}\,, \tag{5.8}$$

with S_N being the surface of the Landau band and $\nabla E_N(\mathbf{k})$ being the k–gradient of the Landau band energy $E_N(\mathbf{k})$. To obtain the density of states at the Fermi energy, the gradient of the bands at the Fermi energy has to be calculated for a given magnetic field. In graphite this calculation is radically simplified, as the band structure becomes quasi-one-dimensional, depending only on the wave vector in z-direction, k_z. The density of states has therefore singularities at

$$\frac{dE_N}{dk_z}(B) = 0, \tag{5.9}$$

that is for local maxima and minima of the bands. Consequently maxima in the conductivity are observed when local extrema of the bands cross the Fermi energy. With $\sigma_{xx} \propto 1/\rho_{xx}$ (Eq. (5.6)) in graphite, maxima in the conductivity translate to minima in the resistivity. This means that minima in the longitudinal resistance R_{xx} due to electrons and holes are observed when local minima of the electron bands at the K point ($k_z = 0$) and local maxima of the hole bands with $k_z \approx 0.3$ close to the H point ($k_z = 0.5$) cross the Fermi energy.

For a quantitative agreement, the magnetotransport data has to be fitted to the full SWM-model ($\gamma_3 \neq 0$). This means that the magnetic field values of the minima in ΔR_{xx} have to coincide with the magnetic field values at the crossing of the local extrema with the Fermi energy in the band structure model. The starting point of the fitting procedure are the values of the SWM γ-parameters and the value of the Fermi energy taken from previous experiments and summarized in Ref. [28] (see Table 5.1). Initially we restrict ourselves to the magnetic field region $B < 2$ T. In this region it is a good approximation that the Fermi energy is constant, as many Landau bands are below the Fermi energy and the Fermi energy is stabilized ($\hbar\omega_c \ll E_F$). We come back to the problem of the Fermi energy movement when we look at the calculations performed at higher magnetic fields. The eight parameters (γ-parameters and Fermi energy) given in Ref. [28] where stepwise refined until a good agreement between the measured data points and the SWM fit was obtained. Even with the large desktop computing power available nowadays for numerically diagonalizing the SWM Hamiltonian, the procedure of finding a reasonable fit was time consuming (more than two weeks), due to the large parameter space and the large size of the magnetic field SWM Hamiltonian.

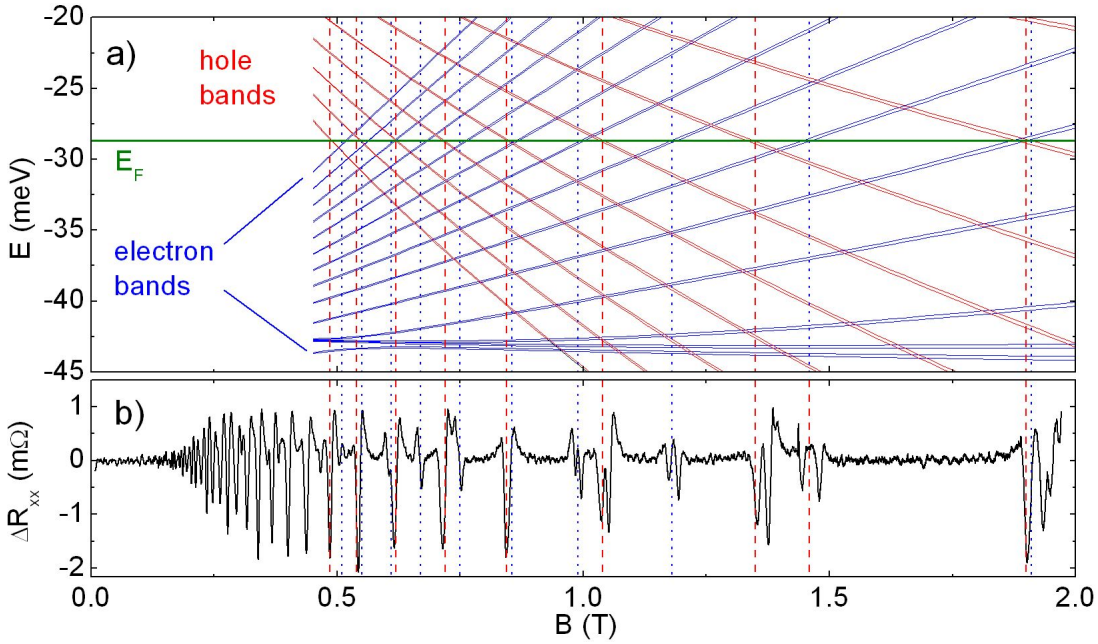

Fig. 5.14: ***a)*** *Spin split electron (increasing with B) and hole (decreasing with B) bands, which correspond to maxima in the density of states ($dE/dk_z = 0$), as a function of the magnetic field calculated from the SWM-model for $0.4 \leq B \leq 2$ T. The crossing of the electron and hole bands with the constant Fermi energy is in nearly perfect agreement with the measured magnetic field values of the electron features (dotted lines) and hole features (dashed lines), shown in* ***b)****. The parameters for the calculations are given in Table 5.1.*

Parameters	**This work**	**Ref.** [28]
γ_0 (eV)	3.37 ± 0.02	3.16 ± 0.05
γ_1 (eV)	0.363 ± 0.05	0.39 ± 0.01
γ_2 (eV)	-0.0243 ± 0.001	-0.02 ± 0.002
γ_3 (eV)	0.31 ± 0.05	0.315 ± 0.015
γ_4 (eV)	0.07 ± 0.01	0.044 ± 0.024
γ_5 (eV)	0.05 ± 0.01	0.038 ± 0.005
$\gamma_6 = \Delta$ (eV)	-0.007 ± 0.001	-0.008 ± 0.002
E_F (eV)	-0.0287 ± 0.001	-0.024 ± 0.002
g_s	2.4 ± 0.1	–
n_0 (cm^{-3})	$-(2.4 \pm 0.4) \times 10^{17}$	–

Table 5.1: *Summary of the SWM parameters found in this work and compared to the values given in Ref. [28].*

Fig. 5.14 a) represents the result of the fitting procedure at low magnetic field with a constant Fermi energy. The band energy plotted as a function of the magnetic field corresponds to local extrema of the bands (see Fig. 5.13). Contrary to the schematic picture of Fig. 5.13 b), spin splitting has been taken into account. The bands with increasing energy for increasing magnetic field are electron bands. The bands with decreasing energy for increasing magnetic field are hole bands. The Fermi energy is at $E_F \approx -29$ meV. The crossing of the electron and hole bands with the Fermi energy is in nearly perfect agreement with the measured magnetic field positions of the minima features of the electron (dotted lines) and hole (dashed lines) oscillations (Fig. 5.14 b)).

The parameters found by the fitting procedure are given in Table 5.1. While we are unable to fit our data with exactly the same tight binding parameters as in Ref. [28], the values we find are nevertheless not significantly different. Moreover, the theoretically predicted [76] effective electron mass $m^* = 4\hbar^2\gamma_1/3a_0^2\gamma_0^2 = 0.054m_e$, where $a_0 = 0.246$ nm is the in-plane lattice constant, calculated using our values for γ_0 and γ_1, is in good agreement with the accepted value of $m^* = 0.054m_e$ found by means of cyclotron resonance measurements [51].

If we assume a constant Fermi energy for magnetic fields $B > 2$ T, the magnetic field values at which the Fermi energy crosses the bands differ significantly from those observed experimentally. This is shown in Fig. 5.16 a). The dashed line corresponds to the constant Fermi energy. The crossing points of the constant Fermi energy with the bands are marked by arrows. The experimental magnetic field values are given by the vertical dashed and dotted lines, respectively. The differences of the magnetic field values reveal themselves in the deviation of the $1/B$ periodicity in the $1/B$ vs. quantum number N plot of Fig. 5.12. The deviations can be explained by a movement of the Fermi energy as the quantum limit is approached [74]. Qualitatively this can be understood considering that at high magnetic fields fewer bands are located in the vicinity of the Fermi energy, i.e., when the magnetic field is changed, electrons and holes are transferred between the electron

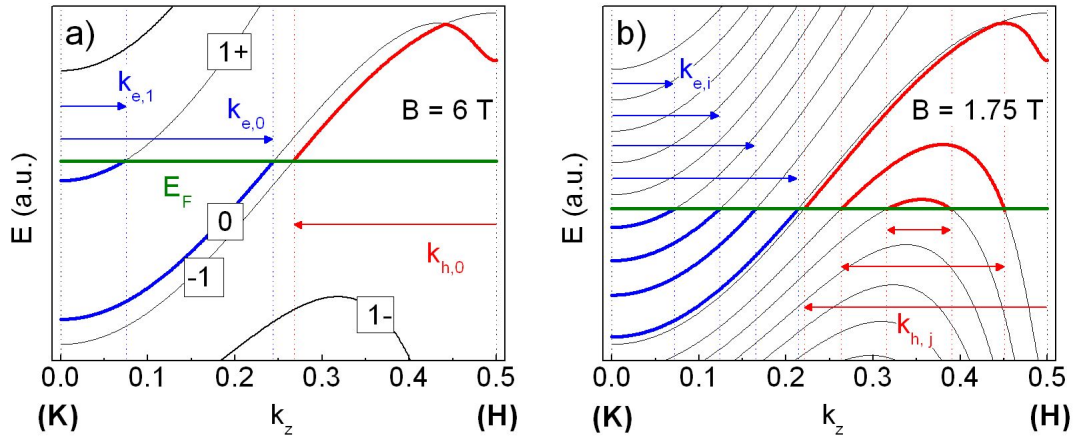

Fig. 5.15: ***a)*** *Band structure for $B = 6$ T ($\gamma_3 = 0$) to illustrate the self-consistent calculation of the Fermi energy. The electron and hole concentrations are given by $n_e = B \cdot (k_{e,0} + k_{e,1})$ and $n_h = B \cdot (k_{h,0})$, respectively.* ***b)*** *At low magnetic field ($B = 1.75$ T), many more bands are found below (electrons) and above (holes) the Fermi energy and the movement of the Fermi energy can be neglected.*

and hole puddles in order to keep the difference of the electron and hole concentration constant,

$$n_e - n_h = n_0. \tag{5.10}$$

In a perfect graphite lattice with no defects, the density of the electrons, n_e, equals the density of the holes, n_h [28]. However, the real lattice is doped with impurities. Those impurities - ionized donors (n^+) and acceptors (n^-) - result in an imbalance of the electron and hole concentration. The difference of the electron and hole concentration is given by $n_0 = n_e - n_h = n^+ - n^-$. n_0 gives rise to the Hall signal $\rho_{xy} = B/e(n_h - n_e)$ (Eq. (5.2)) shown in Fig. 5.1 b).

The electron and hole concentration and therefore the movement of the Fermi energy can be calculated self-consistently within the SWM-model. The electron and hole concentrations of a given band N, n_N, are proportional to the magnetic field B multiplied by the energy integral of the density of states,

$$n_N \propto B \cdot \int_E \mathrm{DOS}(\mathbf{k}) dE. \tag{5.11}$$

The magnetic field dependence of the electron concentration arises from the degeneracy of the Landau bands $\xi \propto eB/h$. In Eqs. (5.8) and (5.9) we have shown that the density of states in graphite reduces to a quasi-one-dimensional density of states. Consequently Eq. (5.11) gives

$$n \propto B \cdot \int_E \mathrm{DOS}(\mathbf{k}) dE = B \cdot \int \frac{1}{\left(\frac{dE}{dk_z}\right)} dE = B \cdot \int dk_z \approx B \cdot \sum \Delta k_z. \tag{5.12}$$

Fig. 5.15 a) demonstrates the calculation of the Fermi energy at high magnetic field ($B = 6$ T, $\gamma_3 = 0$). In this magnetic field region we only have to consider the bands $N = 0$ and $N = 1^+$ for

the electron concentration and the band $N = -1$ for the hole concentration. With Eq. (5.11) the electron and hole concentrations are given by

$$n_e = B \cdot (k_{e,0} + k_{e,1}) \quad \text{and} \quad n_h = B \cdot (k_{h,0}) \,.$$

When the magnetic field is decreased, the energy of the electron band $N = 1^+$ decreases while the band energy of the $N = 0$ band stays to a good approximation constant. If the Fermi energy was constant, the electron concentration would increase due to the increasing value of $k_{e,0}$. However, this is forbidden by the "neutrality" condition $n_e - n_h = n_0$. Consequently the Fermi energy has to decrease, which reduces the value of $k_{e,0}$ and increases the value of $k_{h,0}$. Numerically the value of the Fermi energy was found by incrementally changing its value until the condition $n_e - n_h = n_0$ was fulfilled.

At lower magnetic fields, many more bands are below (electrons) and above (holes) the Fermi energy. This is illustrated in Fig. 5.15 b) for $B = 1.75$ T. n_e and n_h are given by

$$n_e = B \cdot \sum_i k_{e,i} \quad \text{and} \quad n_h = B \cdot \sum_j k_{h,j}.$$

It is evident that due to the large number of bands the Fermi energy is stabilized at low magnetic fields, i.e., adding electrons or holes due to changes of the magnetic field does not require significant changes of the Fermi energy to fulfill $n_e - n_h = n_0$ and the movement of the Fermi energy can be neglected.

Fig. 5.16 shows the electron and hole bands as a function of the magnetic field from $B = 0.5 - 10$ T. The Fermi energy was calculated self-consistently with the above described method. The impurity concentration was assumed to be low, i.e., about 1.5% of the electron and hole concentration. The agreement between the magnetic field values at which the Fermi energy crosses the bands and those observed experimentally (dashed and dotted lines) is once again remarkable.

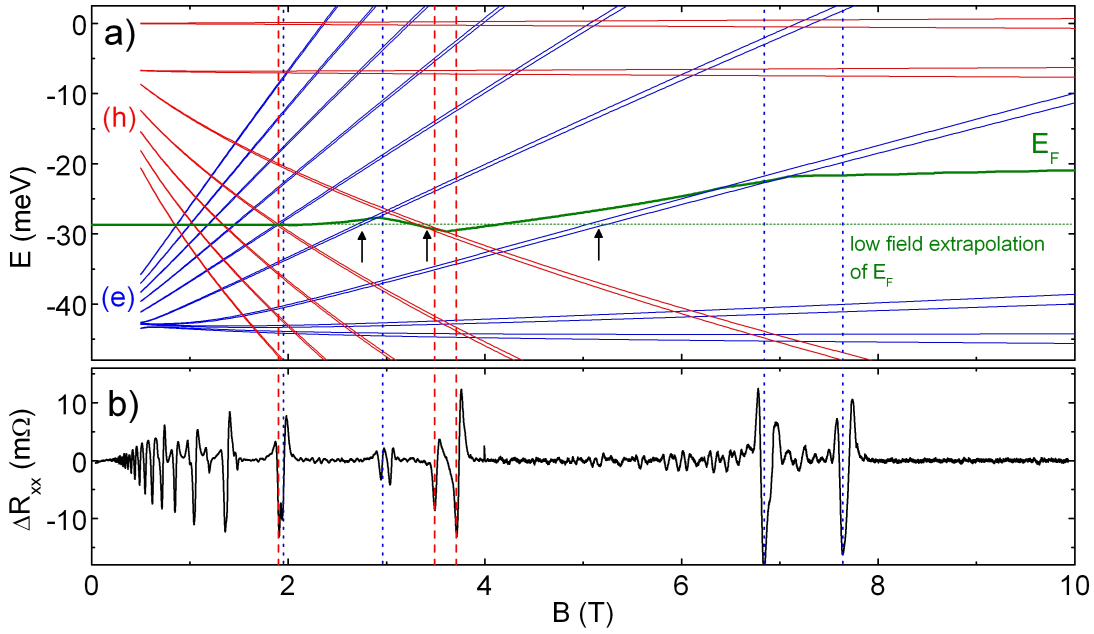

Fig. 5.16: *Electron and hole bands for* $0.4 \leq B \leq 10$ *T. The Fermi energy is calculated self-consistently, keeping the difference of the electron and hole concentration constant, i.e.,* $n_e - n_h = n_0$*. The agreement with the magnetic field positions of the electron features (dotted lines) and hole features (dashed lines) extracted from the magnetotransport data* ***b)*** *is remarkable. The arrows mark the magnetic field positions at which the features should occur if the Fermi energy was constant.*

5.5 Majority Dirac carriers in magnetotransport of graphite?

In 2004, the authors of Ref. [73], Luk'yanchuk and Kopelevich, claimed that a macroscopic concentration of massless charge carriers with linear energy spectrum exists in graphite and governs its electronic transport properties. Their findings are based on the phase analysis of quantum oscillations in magnetotransport and de Haas-van Alphen oscillations. They claimed that one type of oscillations observed in graphite has a phase of $\gamma = 1/2$ as predicted by the SMW-model, while the other type of oscillations has a phase of $\gamma = 0$ in contradiction to the SMW-model (see discussion in Chapter 3.2). In subsequent papers they suggested that due to the fact that these carriers have the same nature as Dirac fermions observed in graphene, graphite consists of graphene layers which are electronically almost independent [59, 77]. They came to the conclusion that the classical SWM-model has to be revised.

The view point that graphite is a system of independent mono and multi carbon layers is in strong contradiction to our work, in which we demonstrated that the results of magnetotransport in graphite can be fully understood within the frame work of the SWM-model [78]. The question

in which model graphite should be described became subject of an ongoing debate [79,80]. In this section we put forward some explanations which are aimed at correcting the controversy.

In Ref. [59] Luk'yanchuk and Kopelevich extract the phase values of the quantum oscillations from a $1/B$ vs. N plot of magnetotransport data. In Fig. 5.12 we showed such a plot for our low temperature data. As $N = B_0/B - \gamma + \delta$, the phase can in principle be extracted by plotting the quantum number N as a function of the positions of the features in inverse magnetic field $1/B$ followed by a linear fit of $N(1/B)$ which is extrapolated to $N(1/B \rightarrow 0)$. At $N(1/B \rightarrow 0)$ the phase term is given by $\varphi = N(1/B = 0) = -\gamma + \delta$.

Fig. 5.17 a) shows the $1/B$ vs. N plot of magnetotransport data presented in the paper of Luk'yanchuk and Kopelevich of 2006 [59]. Note that they only observed Shubnikov-de Haas oscillations at $B > 1$ T, i.e., $1 \leq N \leq 5$. They assigned both minima ($\circ$) of the oscillations (integer quantum numbers N) and maxima ($\times$) of the oscillations (half integer numbers N). Our low temperature data shows that the assignment of maxima features to half integer quantum numbers is questionable, as features clearly reveal themselves as minima in the magnetotransport raw data (Fig. 5.8 a)). A linear fit through the data gives $B_{F,\mathrm{low}} = 4.62$ T, $\varphi_{\mathrm{low}} = -0.6$ for the low frequency oscillations and $B_{F,\mathrm{high}} = 6.16$ T, $\varphi_{\mathrm{high}} = 0$ for the high frequency oscillations. This would imply that the charge carriers giving rise to the high frequency oscillations are of Dirac like nature.

However, a direct comparison between our low temperature data and the data of Luk'yanchuk and Kopelevich [59], presented in Fig. 5.17 b) explains the discrepancy. Note that even though

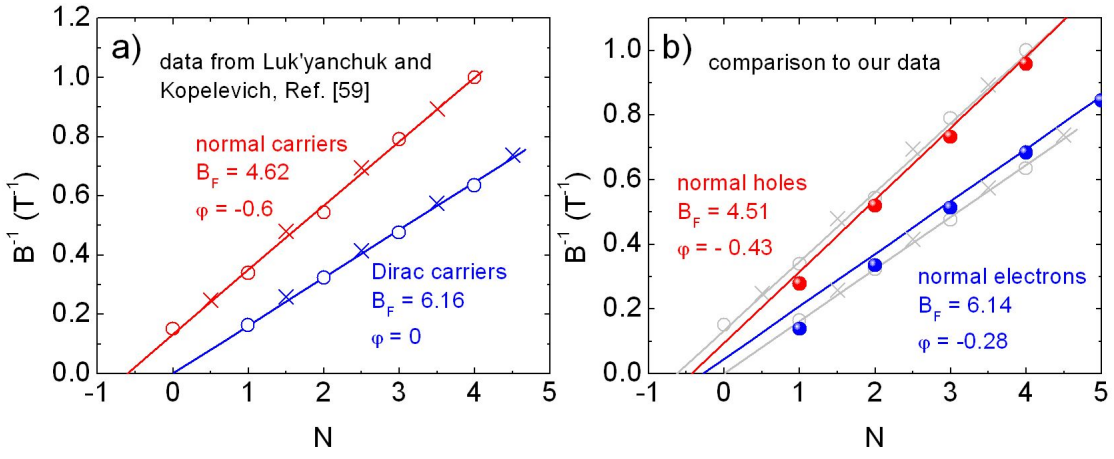

Fig. 5.17: ***a)*** *$1/B$ vs. N plot extracted from Ref. [59]. The data points "$\circ$" and "$\times$" correspond to maxima and minima positions of Shubnikov-de Haas oscillations, respectively. A linear extrapolation of the data to $1/B = 0$ (solid lines) allows to extract the phase factor φ. The phase $\varphi = 0$ ($\gamma = 0$, $\delta = 0$) is characteristic for two-dimensional Dirac fermions.* ***b)*** *Comparison of the data from Ref. [59] to our low temperature data. The extrapolation of a phase from data which is non periodic in $1/B$ is questionable.*

the positions of the features are similar, our low temperature data reveal a strong deviation from the low magnetic field behaviour, given by the solid line (with the frequencies and the phases extracted from the Fourier transform (see Fig. 5.12)). The deviation from the $1/B$ periodicity is due to the electron hole cross talk, which leads to a considerable movement of the Fermi energy. The extrapolation of a phase term from data which is not periodic in $1/B$ is at the very least highly questionable.

Remark: In Ref. [73] Luk'yanchuk and Kopelevich, in order to assign the $\gamma = 0$ series to holes at the H point, are obliged to invert the well-established assignment of the high frequency series to electrons at the K point and the low frequency series to holes close to the H point [14]. If correct, this reassignment would have far reaching consequences, changing the position of the Fermi energy and modifying some of the SWM parameters. A number of problems with Ref. [73] have already been pointed out, notably concerning the validity of this reassignment [22]. Moreover, the sign of the de Haas-van Alphen signal, invoked by Luk'yanchuk and Kopelevich to lend support to the reassignment, cannot be used to determine the nature of the charge carriers [22].

5.6 Minority carriers in graphite?

In Section 3.2 it was shown that apart from the two types of majority charge carriers (electrons and holes), the SWM-model predicts a third kind of charge carriers located at the H point of graphite (see Fig. 3.6). Due to their small Fermi surface extremal cross section, the carriers at the H points are referred to as *minority holes*. Oscillations with a much smaller fundamental frequency were first discovered by Soule (de Haas-van Alphen studies) [81] and further investigated by Williamson *et al.* (de Haas-van Alphen) [13], Anderson *et al.* (de Haas-van Alphen) [82] and Woollam (thermoelectric power and magnetotransport studies) [83]. According to those publications the existence of at least one additional minority group appears to be beyond doubt. Its fundamental frequency was determined to be $B_{F,m} \approx 0.3$ T.

Despite the high quality of the mK magnetotransport data obtained for natural graphite (see Section 5.2), a third series of oscillations is neither seen in the background removed data at low magnetic field (Fig. 5.8 c)), nor in the spectral intensity of the Fourier transformed signal of $\Delta R_{xx}(1/B)$. This is surprising, since the quantum oscillations already start at $B_0 \approx 0.07$ T, and at least four minority features should be observed in this magnetic field region ($B_{F,m}/4 = 0.075$ T). A possible explanation for not observing minority carrier oscillations in the mK magnetotransport data is that the minority carrier oscillations are hidden by the majority carrier oscillations in this magnetic field region. The problem can be overcome when the magnetic field is swept faster. This results in a lower resolution in magnetic field, i.e. the rapidly oscillating majority features at very low magnetic field are not resolved. A faster sweep shifts therefore the onset magnetic field of the majority quantum oscillations B_0 to higher magnetic fields.

Fig. 5.18 shows R_{xx} and the background removed resistance ΔR_{xx} measured at mK temperatures with a magnetic field sweep rate of $dB/dt = 0.05$ T/min (instead of $dB/dt = 0.001$ T/min in Section 5.2) in the magnetic field range $-0.6 \leq B \leq 0.6$ T. For this sweep rate, the majority

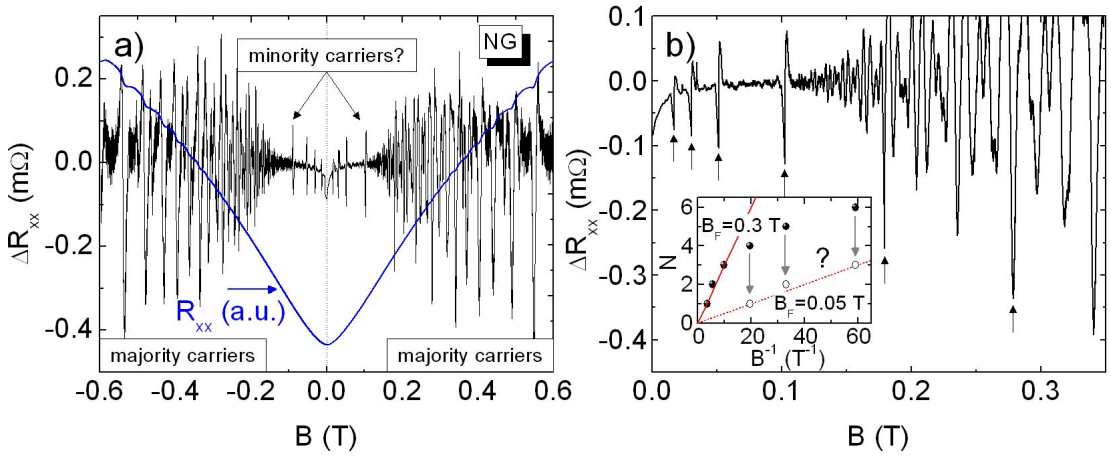

Fig. 5.18: ***a)*** *R_{xx} and ΔR_{xx} of natural graphite measured at mK temperature with a sweep rate of $dB/dt = 0.05$ T/min (instead of $dB/dt = 0.001$ T/min in Fig. 5.8 c)) in the magnetic field range $-0.6 \leq B \leq 0.6$ T. A third series of features is observed at low magnetic fields.* ***b)*** *Zoom in on the low magnetic field features at positive polarization of the magnetic field. The presumed third series of quantum oscillations is marked by arrows.* ***Inset****: N vs. 1/B plot. The features at higher magnetic field are periodic in $B_{F,m}/B$ with $B_{F,m} \approx 0.3$.The features at lower field have rather a fundamental frequency of $B_{F,m} \approx 0.05$ T.*

quantum oscillations start at higher magnetic field ($B_0 \approx 0.12$ T instead of $B_0 \approx 0.07$ T). In addition to the majority quantum oscillations, a third series of features appears at very low magnetic field. Fig. 5.18 b) provides a closer look on these features for positive polarization of the magnetic field ($0 \leq B \leq 0.35$ T). The features are marked by arrows, assuming the fundamental frequency $B_{F,m} \approx 0.3$ T of minority hole oscillations is correct and that the $N = 1$ feature should therefore be observed at $B \approx 0.3$ T. However, the *N vs. 1/B plot* does not reveal the expected simple linear dependence (inset of Fig. 5.18 b)). While the oscillations for $B > 0.1$ T with a fundamental field $B_{F,m} \approx 0.3$ T are periodic in $B_{F,m}/B$ (solid line) the features at lower magnetic field do not fit to this series. They could be consistent with another minority carrier series with $B_{F,m} \approx 0.05$ T but the very few data points do not allow a definitive assignment. Further studies, notably de Haas-van Alphen experiments using a low-frequency field modulation technique as in Ref. [13] are needed.

5.7 Conclusion

Based on our results of low temperature magnetotransport data, we come to the conclusion that the charge carriers in graphite are perfectly described by the SWM-model. Not only the frequencies and phases extracted from the mK magnetotransport data are in agreement with what is predicted by the SWM Fermi surface of graphite, but detailed SWM calculations in magnetic field show that the observed features in magnetotransport can be reproduced nearly perfectly by the crossing of the Landau bands with the Fermi energy. The deviations of the features form the $1/B$ periodicity at high magnetic fields can be explained by a movement of the Fermi energy due to a considerable electron hole cross talk. Our findings are in agreement with a great number of experiments performed so far, e.g. magnetotransport [9–12], de Haas-van Alphen oscillations [9, 13], magneto reflection [14, 15], microwave absorption and cyclotron resonance [16, 17], and very recently Nernst effect [18].
Minority carrier oscillations in magnetotransport are probably observed but further measurements are required to clarify this point.

6 High field magnetotransport: Spin splitting and CDW phase

Résume du chapitre

Nous avons effectué des mesures de magnétotransport sur le graphite sous champ magnétique intense incliné ($0 < B < 28$ T) pour étudier l'effet Zeeman. Puisque le mouvement orbital des porteurs de charge ne dépend que de la composante perpendiculaire du champ magnétique $B_\perp$, le champ magnétique dans le plan peut être utilisé pour modifier l'énergie de Zeeman $g^*\mu_B B$. Nous avons obtenu la valeur $g^* = 2.5 \pm 0.1$ pour $1.5 \leq B \leq 22$ T ce qui est supérieur à la valeur de $g = 2.0023$ pour des électrons libres. La valeur nettement plus grande trouvée ici est attribuée aux interactions multi-corps (interaction d'échange).

Des mesures de magnétotransport du graphite sous champ magnétique intense ($0 < B < 28$ T) ont été également employées pour étudier l'onde de densité de charge pour différentes températures entre $T = 50$ mK et $T = 0.9$ K. L'onde de densité de charge se caractérise par une augmentation suivie d'une réduction de la magnétorésistance aux champs magnétiques élevés [26,27]. En accord avec la Réf. [27], le champ magnétique B_{CDW} auquel l'onde de densité de charge apparait diminue à température décroissante. B_{CDW} et la température sont liés par une équation de type Bardeen-Cooper-Schrieffer (BCS).

The present chapter focuses on high field magnetotransport of natural graphite and HOPG in the magnetic field range $0 \leq B \leq 28$ T performed on a 20 MW resistive magnet. It is divided into two parts: The study of the *spin splitting* of magnetotransport features in tilted field configuration and the observation of a *charge density wave (CDW)* phase for different temperatures with the magnetic field applied normal to the sample plane.

Spin splitting: In the first part of the chapter we focus on spin split features observed in the magnetotransport data of $\Delta R_{xx}(B)$. While orbital effects have been extensively used to caliper the Fermi surface [9–11, 59, 73, 83], the more subtle spin effects have received less attention.

This is perhaps because the well documented movement of the Fermi energy in magnetic field seriously complicates the extraction of the spin splitting (g-factor) from the magnetotransport data (see previous chapter). Recent advances in experimental techniques, in particular the vastly increased desktop computing power available for diagonalizing the SWM Hamiltonian, makes it timely to revisit this problem, extending previous measurements to higher magnetic fields and lower temperatures.

The g-factor of graphite has been precisely measured using electron spin resonance. It is slightly anisotropic and close to the free electron value [37, 38, 84, 85] due to the small spin orbit coupling of carbon [50]. However, in accordance with Larmor's theorem, electron spin resonance is insensitive to many body effects, and measures the undressed spin splitting corresponding to neutral excitations [86]. Transport techniques on the other hand probe charged spin excitations which include the exchange interaction due to many body effects. The difference between the electron spin resonance and the transport spin splitting is therefore a measure of the importance of many body effects in graphite.

Here, we extend our previous low temperature investigation of natural graphite using tilted magnetic fields up to $B = 28$ T in order to probe the spin splitting of the orbital features in the magnetotransport. Since the orbital motion of the carriers depends only on the perpendicular component of the magnetic field, the in-plane magnetic field in the tilted field configuration can be used to tune the Zeeman energy. The magnetic field splitting, ΔB, of the orbital features due to the spin degree of freedom, does not show the expected quadratic increase as a function of the total magnetic field (see Section 6.1.3). This is direct experimental evidence that the Fermi energy is not constant but rather moves in the magnetic field. The magnetotransport data in tilted magnetic fields has been analyzed using the SWM-model, including a self-consistent calculation of the Fermi level movement, to extract the spin splitting, and hence the g-factor, $g^* = 2.5 \pm 0.1$ for both electrons and holes. The usual simple model which calculates the magnetic field position for the spin Landau bands crossing the Fermi energy can explain the observed ΔB versus total magnetic field dependence provided the movement of the Fermi level, taken from the SWM-model, is included. Within experimental error, we find no evidence for an anisotropy of the magnetotransport g-factor.

The results of this part of the chapter have been published in [J. M. Schneider *et al.*, Phys. Rev. B, **81**, 195204 (2010)].

Charge density wave (CDW) phase: In Ref. [26] it was reported for the first time that the magnetoresistance in graphite increases abruptly at high magnetic fields and low temperatures. Since then, a number of experiments has been performed in order to explain the nature of this magnetic field induced phase [12, 27, 58, 87–90]. The fact that the critical field, at which the resistance increases sharply, has a strong temperature dependence suggests that this phenomenon can be interpreted by an electronic phase transition involving many–body effects [87]. Whereas the real nature the magnetic field induced phase remains still to be found, Yoshioka and Fukuyama showed that it can be discussed theoretically in terms of the formation of a charge density wave phase associated with a one-dimensional energy spectrum [91]. In this chapter we extend temper-

ature dependent measurements of the charge density wave phase presented recently in Ref. [27] ($T \geq 1.1$ K) to lower temperatures ($T \leq 1.0$ K). Our data agrees with the findings that the critical temperature, at which the sharp increase of the resistance is observed, is linked to the applied field by a Bardeen-Cooper-Schrieffer (BCS)-type formula [92].

6.1 Spin splitting

6.1.1 Experiment

For the measurements we used the same mm-size pieces of natural graphite as discussed in the previous chapter. The silver paint contacts were made in an approximate Hall-bar configuration with the current flowing in the *ab* plane. The measurements were performed using a 28 T resistive magnet and a ^{3}He cryostat ($T \approx 300$ mK), equipped with an *in situ* rotation stage. The longitudinal resistance $R_{xx}(B)$ was measured using conventional phase sensitive detection with a current of 10 μA at 10.7 Hz. The exact orientation of the rotation stage corresponding to $B \| ab$ was determined experimentally by minimizing the magnetoresistance $R_{xx}(B)$ at low magnetic field [9].

6.1.2 Angular dependence of the quantum oscillations

The longitudinal resistance R_{xx} as a function of the magnetic field from $B = 0 - 28$ T for various orientations of the magnetic field between $\theta = 0^\circ$ ($B \perp ab$) and $\theta = 90^\circ$ ($B \| ab$) is shown in Fig. 6.1 a). In perpendicular magnetic field ($\theta = 0^\circ$), $R_{xx}(B)$ increases by three orders of magnitude between $B = 0$ T and $B = 21$ T. Above 21 T the resistance decreases signalling the onset of a charge density wave state [12, 27, 58, 87–90]. In the magnetic field range $0 < B < 8$ T, small quantum oscillations due to the majority electrons and holes are superimposed on the large magnetoresistance background [10, 11, 59, 73, 78, 83]. When the sample is tilted away from $B \perp ab$, the magnetoresistance is strongly suppressed, which is a clear signature of the highly anisotropic nature of the carrier transport in graphite. Nevertheless, the magnetoresistance for $\theta = 90^\circ$ remains considerable. It is only one order of magnitude smaller than for $\theta = 0^\circ$. However, this could be attributed to a small residual $B \perp ab$ component of the magnetic field if the sample was slightly misaligned on the rotation stage preventing the $\theta = 90^\circ$ condition ever being reached. Comparing the $\theta = 0^\circ$ and the $\theta = 90^\circ$ data curves, we estimate that an experimentally plausible misalignment of $\simeq 2.7^\circ$ would be sufficient to explain the observed magnetoresistance. Additionally, the lack of crystal perfection, e.g. the possible misalignment of layers within the sample, should be considered [93].

For increasing tilt angles the quantum oscillations are shifted to higher (total) magnetic field. The quantum oscillations are better seen in the background removed data ΔR_{xx}. Here the large magnetoresistance background is again removed by subtracting a smoothed (moving window average) data curve. A Fourier transformation of the ΔR_{xx} vs. $1/B$ data with the magnetic field applied perpendicular to the sample plane, gives fundamental frequencies of $B_F = 6.15$ T and $B_F = 4.50$ T for electrons and holes, respectively. In Fig. 6.1 c) ΔR_{xx} is shown as a function of the perpendicular magnetic field $B_\perp = B\cos(\theta)$. Plotted in this way there is no shift of the magnetic field position of the quantum oscillations with the tilt angle showing that their position depends only on the perpendicular component of the magnetic field. Thus, the orbital motion of the carriers is effectively confined within the *ab* plane (each graphene sheet) due to the extremely anisotropic conductivity in graphite [28].

This quasi-two-dimensional behaviour is confirmed in Fig. 6.2 where we plot the ratio of the "fun-

damental" frequencies for the holes and the electrons $B_F(0)/B_F(\theta)$ as a function of the tilt angle θ. For the holes the fundamental frequency is obtained from the Fourier transformation at each angle of the corresponding ΔR_{xx} vs. 1/B curve. For the electrons we use rather the position of the $N = 1$ feature since the smaller amplitude of the electron oscillations at high tilt angles makes the Fourier transform unreliable. For both electrons and holes, for angles up to $\theta = 70°$, $B_F(0)/B_F(\theta)$ shows a nearly perfect $\cos(\theta)$ dependence, indicated by the solid line. The quasi-two-dimensional behaviour can be explained by the extreme anisotropy of graphite, i.e., the in-plane coupling is much bigger than the out of plane coupling ($\rho_c \gg \rho_{ab}$) [28]. This means that the carrier motion is confined to the plane so that the cyclotron energy depends only on the perpendicular component

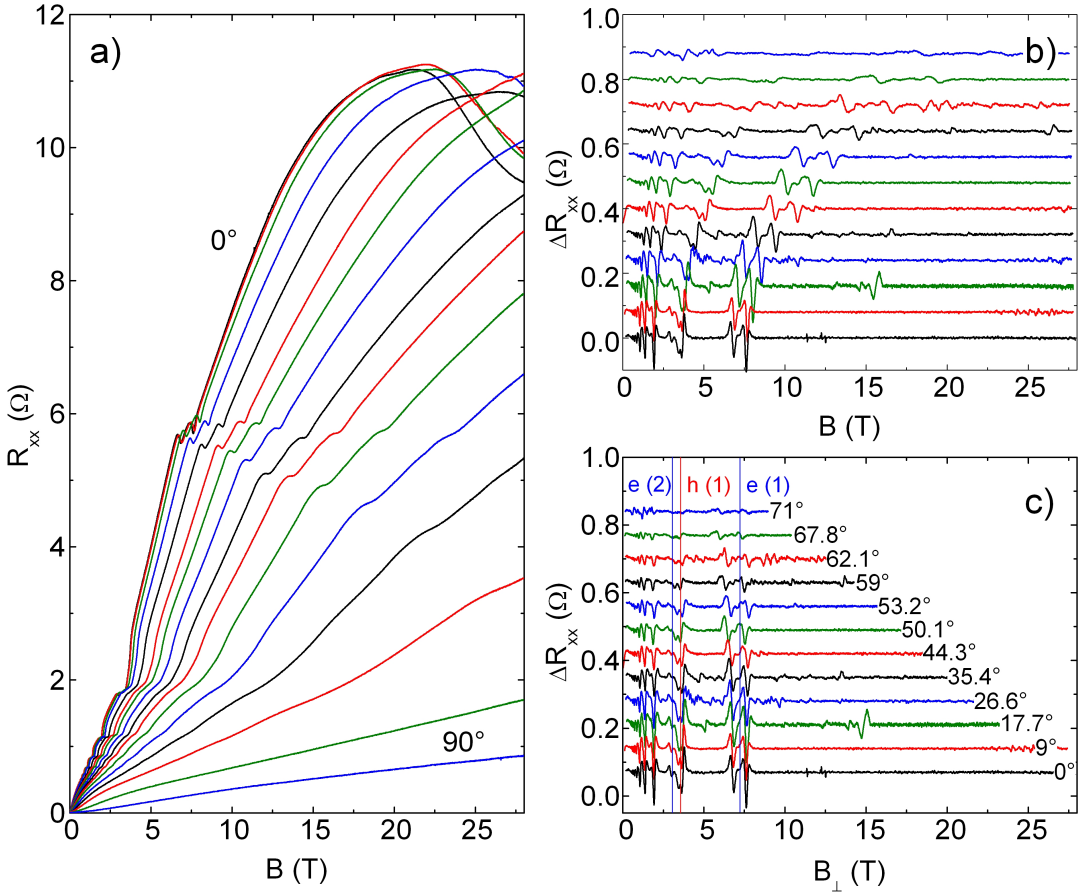

Fig. 6.1: ***a)*** *$R_{xx}(B)$ for various orientations of the magnetic field ($0° \leq \theta \leq 90°$) showing the rapid decrease in the amplitude of the magnetoresistance for increasing tilt angles. Quantum oscillations are superimposed on the large magnetoresistance background.* ***b)-c)*** *Background removed signal ΔR_{xx} as a function of b) the total magnetic field and c) the perpendicular magnetic field $B_\perp = B\cos(\theta)$. In c) the $N = 1,\ 2$ electron and $N = 1$ hole features are indicated by vertical solid lines showing that they depend only on the $B_\perp$ component of the magnetic field.*

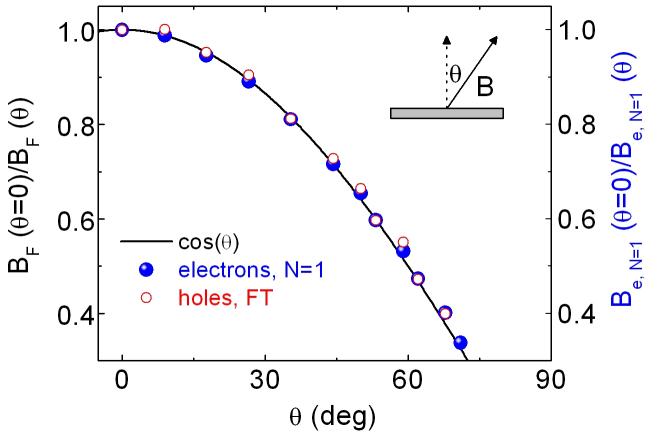

Fig. 6.2: *Normalized "fundamental" magnetic field $B_F(\theta = 0)/B_F(\theta)$ as a function of the angle for the electron and hole oscillations. Both electrons and holes show a nearly perfect $\cos(\theta)$-dependence (solid line), revealing the large anisotropy of graphite.*

of the magnetic field $B_\perp$. Nevertheless, the system is not strictly two-dimensional and the weak coupling between the layers gives rise to Landau bands rather than Landau levels. The oscillations in $R_{xx}(B)$ appear when the Landau bands "cross" the Fermi energy (when there is a maximum in the density of states at E_F). Whereas the angle dependence of quantum oscillations has been extensively studied [9, 11, 13, 94], there has been, to the best of our knowledge, no detailed study of the spin splitting of the Landau bands.

6.1.3 Spin splitting

At very low temperatures $T \simeq 10$ mK, both the electron and hole features are spin split for magnetic fields $B_\perp > 1$ T [78]. At the higher temperatures used here ($T \approx 300$ mK) spin splitting is resolved only for the high magnetic field $N = 1$ electron and hole features. Rotating the sample in field can be used to extract the g-factor since the spin splitting depends on the total magnetic field, while the energy of the Landau bands depends only on the perpendicular component of the magnetic field. The experimentally observed splitting $\Delta B = B_\downarrow - B_\uparrow$, where $B_\uparrow$ and $B_\downarrow$ are the magnetic field positions of the spin up and spin down features, is plotted as a function of the mean total magnetic field position $B_m = (B_\downarrow + B_\uparrow)/2$ for the $N = 1$ electron and hole features in Fig. 6.3 a). The magnetic field splitting of the $N = 1$ electron and $N = 1$ hole features were obtained from the tilted field measurements in Fig. 6.1 b). For the $N = 1$ electron feature ΔB departs significantly from a quadratic behaviour $\Delta B \propto B_m^2$ as indicated by the dashed line in Fig. 6.3 a).

The failure of ΔB to follow a simple quadratic behaviour (see discussion below) is an experimental signature that the movement of the Fermi energy must be taken into account when extracting the g-factor. A simple expression can be derived from the crossing points of a given spin up and spin

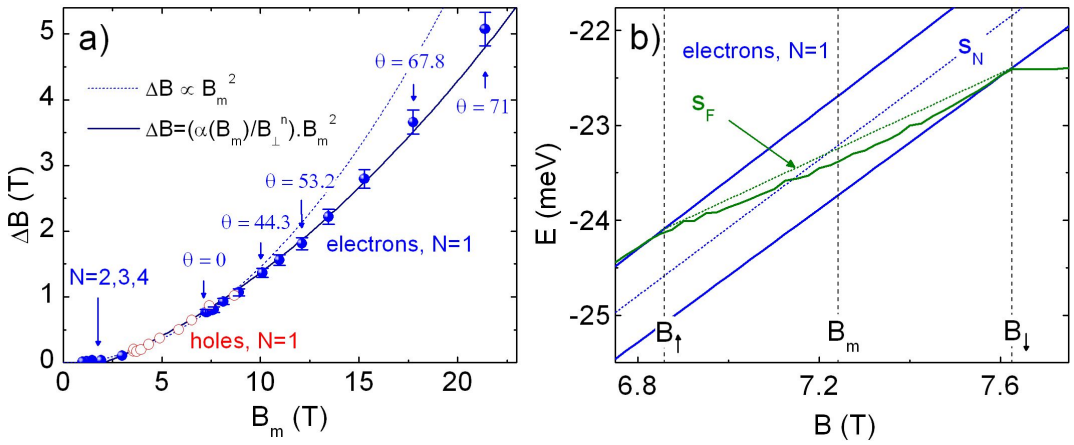

Fig. 6.3: ***a)*** *Magnetic field splitting ΔB as a function of the total magnetic field B_m. The broken line is the $\Delta B \propto B_m^2$ dependence (fitted to the low field data) expected if the Fermi energy was constant. The solid line is calculated for the $N = 1$ electron Landau band using Eq. (6.5) which takes into account the movement of the Fermi energy using $g^* = 2.53$ (discussion in Section 6.1.5).* ***b)*** *Crossing of the $N = 1$ electron Landau band with E_F in the $\theta = 0$ configuration calculated using the SWM-model with $g^* = 2.53$ as described in the text. The movement of E_F (solid line), is calculated assuming a constant total electron and hole concentration. The dashed lines indicate the slope S_N of the $N = 1$ electron Landau band and a linear approximation for S_F.*

down Landau band and the Fermi energy,

$$\Delta B = \frac{g^* \mu_B B_m}{(S_N - S_F)\cos(\theta)} = \frac{\alpha B_m}{\cos(\theta)}, \tag{6.1}$$

where $S_N = \Delta E_N / \Delta B_\perp$ is the slope of the Nth Landau band and $S_F = \Delta E_F / \Delta B_\perp$ is the slope of the Fermi energy in the Nth Landau band obtained from the two crossing points as illustrated for the $\theta = 0$ configuration in Fig. 6.3 b). The angle θ can be taken from experiment, however, a simple expression can also be derived,

$$\cos(\theta) = \frac{B_\perp^N + \frac{g^* \mu_B \Delta B}{4(S_N - S_F)}}{B_m} = \frac{B_\perp^N + \frac{\alpha}{4}\Delta B}{B_m}, \tag{6.2}$$

where $B_\perp^N$ is the perpendicular magnetic field position for the crossing of the (non spin split) Nth Landau band and the Fermi energy (see Fig. 6.3 b)). For both equations we have a single independent dimensionless fitting parameter $\alpha = g^* \mu_B / (S_N - S_F)$. Thus, to extract the g-factor it is necessary to know both S_N and S_F. Neglecting the movement of the Fermi energy, the model predicts $\Delta B \propto B_m^2$ in contradiction with experiment. The dashed line in Fig. 6.3 a) is fitted to the $\theta = 0$ data point assuming $\Delta B \propto B_m^2$. It does not well reproduce the data set and also requires, if we assume $S_F = 0$, an unrealistically large g-factor ($g^* \approx 6.5$).

Eliminating $\cos(\theta)$ from Eqs. (6.1) and (6.2) gives,

$$\Delta B = \frac{\alpha B_m^2}{B_\perp^N + \frac{\alpha}{4}\Delta B} \approx \frac{\alpha B_m^2}{B_\perp^N} \tag{6.3}$$

since $\alpha \ll 1$, so that to a good approximation $B_\perp^N \gg \frac{\alpha}{4}\Delta B$. Eq. (6.2) shows that the experimentally accessible B_m has some physical significance since $B_m \cos(\theta) \simeq B_\perp^N$ to a good approximation. This also implies that Eq. (6.2) should not be used to extract the g-factor since the shift in the perpendicular magnetic field value of the spin split features ($\frac{\alpha}{4}\Delta B$) is too small to be reliably determined from experiment.

The fact that for a given total magnetic field the splitting ΔB of the ($N = 1$) hole and electron Landau bands are the same is at first sight surprising since the effective mass for electrons (0.054 m_e) and holes (0.039 m_e) are fundamentally different [28, 76]. However, we will see that this is fully consistent with the predictions of the Slonczewski, Weiss and McClure band structure calculations when the movement of the Fermi energy is included.

6.1.4 Slonczewski, Weiss and McClure model

In order to extract the g-factor, we use the SWM band structure model [2, 23] with its seven coupling parameters $\gamma_0, \ldots, \gamma_6$ as described in the previous chapter. For $\gamma_3 \neq 0$, the magnetic field Hamiltonian has infinite order, which was numerically reduced to a 600×600 matrix for the exact diagonalization procedure. Since the orbital motion of the carriers depends only on the perpendicular component of the magnetic field, the effect of the in-plane magnetic field can be incorporated into the SWM-model through an effective spin splitting $\Delta_s = g_{\text{eff}} \mu_B B_\perp$ where the real g-factor $g^* = g_{\text{eff}} \cos(\theta)$. In graphite, E_F moves with the applied perpendicular magnetic field as carriers are transferred between the electron and hole pockets [9]. The Fermi level has to be calculated self-consistently assuming that the sum of the electron and hole concentrations is constant, $n - p = n_0$. As in the previous chapter, we have used $n_0 = -2.4 \times 10^{17}$ cm^{-3}. At each angle, the effective spin splitting is found for which the SWM-model gives the correct magnetic field position for the crossing of the spin up and spin down Landau band with the Fermi energy. Fitting to the spin split high magnetic field data requires a slight refinement of the SWM parameters. The values used are given in Table 6.1. Compared to the values in Table 5.1 (page 63) found from the low magnetic field ($B_\perp$) magnetotransport data the changes are small, with the parameters γ_1 and γ_2 changing by only $3 - 4\%$.

Fig. 6.4 a) shows the result for the spin splitting Δ_s extracted from the SWM calculations as a function of the total magnetic field for the $N = 1$ hole and the $N = 1 - 4$ electron Landau bands. The data for the $N > 1$ electron features, taken from Fig. 5.8, was measured only for the $\theta = 0$ configuration at $T = 10$ mK. The spin splitting is similar for both the electron and hole Landau bands at a given total magnetic field. Δ_s increases linearly with magnetic field and a linear fit to $\Delta_s = g^* \mu_B B_m$ (solid line) for both electron and hole Landau bands gives $g_s = 2.5 \pm 0.1$. While the value of g^* found here is similar to the value published by *Woollam* for the $N = 1$ electron feature in $\theta = 0$ configuration, a comparison is not really meaningful since in Ref. [10] the SWM parameter γ_3 was neglected.

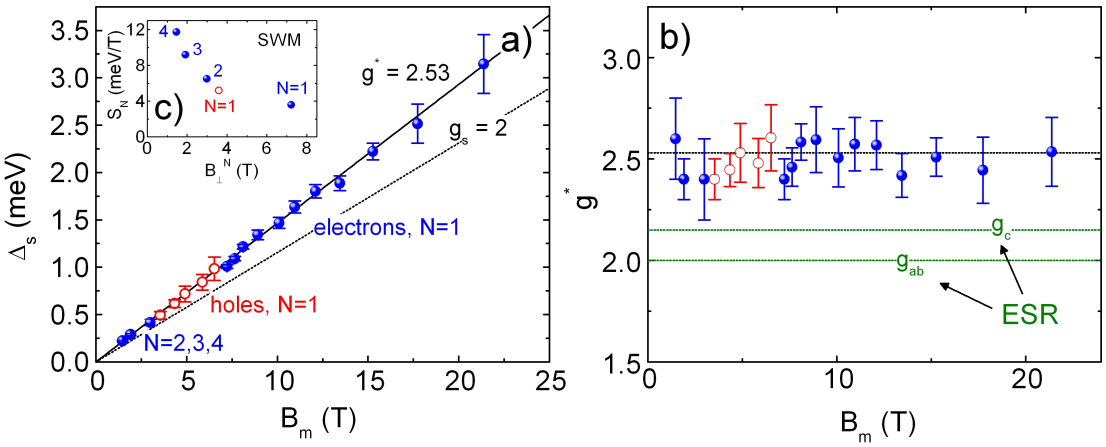

Fig. 6.4: ***a)*** *Spin splitting Δ_s for the electron and hole Landau bands, obtained by fitting the SWM-model to the data in Fig. 6.3 a), as a function of the magnetic field. The solid line is a linear fit to the data giving $g^* = 2.53$. The dashed line corresponds to the free electron value of $g_s = 2$.* ***b)*** *The SWM g-factor for each data point in a). The thick dashed line corresponds to $g^* = 2.53$ while the thin dashed lines correspond to the anisotropic electron spin resonance g-factor.* ***c)*** *SWM-calculation of the slope S_N of the electron and hole Landau bands where they cross the Fermi energy as a function of the perpendicular magnetic field component.*

Alternatively, the g-factor calculated from each data point is plotted in Fig. 6.4 b). Within experimental error there is no magnetic field (angular) dependence of the g-factor, which is also consistent with the linearity of Δ_s vs. B_m, and justifies *a posteriori* our neglect the g-factor anisotropy in the analysis. Anisotropy can be included in our analysis simply by writing $\Delta_s = g_{\text{eff}}\mu_B B_\perp$ where $g_{\text{eff}} = g_c + g_{ab}\tan(\theta)$. However, the scatter in the data (see Fig. 6.4 b)) is comparable to the anisotropy observed in electron spin resonance measurements. Thus, the anisotropy is too small to be observed in the magnetotransport data. A value of $g^* = 2.5 \pm 0.1$ is also consistent with the very simple estimation made from the magnetic field at which spin splitting occurs, ($B_z \sim 1$ T), and at which the Shubnikov-de Haas oscillations start ($B_0 \sim 0.07$ T) in the perpendicular configuration

Parameters		Parameters	
γ_0 (eV)	3.37 ± 0.02	γ_4 (eV)	0.07 ± 0.01
γ_1 (eV)	3.377 ± 0.05	γ_5 (eV)	0.05 ± 0.01
γ_2 (eV)	-0.025 ± 0.001	γ_6 (eV)	-0.007 ± 0.001
γ_3 (eV)	3.2 ± 0.05	E_F (eV)	-0.0287 ± 0.001

Table 6.1: *Summary of the SWM parameters used in this chapter.*

and at $T = 10$ mK [78]. Assuming the Landau level broadening to be independent of the magnetic field we can write $g^*\mu_B B_z = \hbar e B_0/m^*$ where $m^* = 0.054 m_e$ is the effective electron mass [76] so that $g^* \approx \hbar e B_0/m^*\mu_B B_z \approx 2.5$.

Electron spin resonance measurements in graphite give a low temperature anisotropic g-factor of $g_{ab} = 2.003$ for $B \,\|$ab and $g_c = 2.15$ for $B \,\|$c [37, 38]. These values are close to the free electron value of $g_{ab} = 2.0023$ as expected for carbon with its small spin orbit coupling parameter Λ [50]. In accordance with Larmor's theorem, optical techniques measure the splitting corresponding to neutral ($k = 0$) transitions and are therefore insensitive to many body corrections. Magnetotransport measurements, on the other hand, are sensitive to long wavelength charged excitations which include the many body (Coulomb) contribution to the spin splitting. The significantly larger value of $g^* = 2.5 \pm 0.1$ found here in transport measurements is therefore attributed to the many body (exchange) enhancement of the spin splitting. In two dimensions, the enhanced spin gap can be written [40]

$$\Delta_s = g\mu_B B_m + \frac{n_\uparrow - n_\downarrow}{n_\uparrow + n_\downarrow}\frac{e^2}{\varepsilon \ell_B}, \tag{6.4}$$

where g differs from the free electron g-factor due to the spin orbit coupling in graphite and the magnetic length depends only on the perpendicular component of magnetic field. This implies that for a given Landau band crossing E_F, the Coulomb energy $e^2/\varepsilon\ell_B$ is constant. Therefore, to reproduce the observed linear dependence of $\Delta_s(B_m)$ a linear increase in the spin polarization $(n_\uparrow - n_\downarrow)/(n_\uparrow + n_\downarrow)$ as a function of B_m is required. To verify this a self-consistent calculation of the spin polarization is necessary since the spin splitting depends on the polarization and vice-versa.

6.1.5 Spin splitting including the movement of the Fermi energy

In this section we present a simple model which allows to illustrate the Fermi energy movement S_F and therefore the magnetic field dependence of the parameter $\alpha(B_m)$, which is required to reproduce the non quadratic behaviour of the magnetic field splitting ΔB as a function of the total magnetic field B_m (see Fig. 6.3 a)). The movement of the Fermi energy within the $N = 1$ electron band, shown in Fig. 6.3 b), can be fitted nearly perfectly by a second order polynomial. From the SWM calculations, we know that the slope of E_F at $B_\downarrow$ is to a good approximation constant, i.e., independent of the spin splitting (angle). Using this fact, the Fermi energy movement for a given angle can be approximated by shifting the $\theta = 0$ second order polynomial (equivalent to writing the polynomial with coordinates $(B - B_\downarrow)$) and extrapolating the behaviour of E_F to lower magnetic fields. The result of those calculations is shown in Fig. 6.5 a) for various angles. The calculated slope of the Fermi energy movement within the $N = 1$ electron Landau band is given in Fig. 6.5 b).

With the Fermi energy movement within the $N = 1$ electron Landau band, the magnetic field (angular) dependence of the dimensionless parameter α can be extracted. The result is depicted in Fig. 6.5 c), where the calculated value of α is plotted versus the inverse magnetic field for the

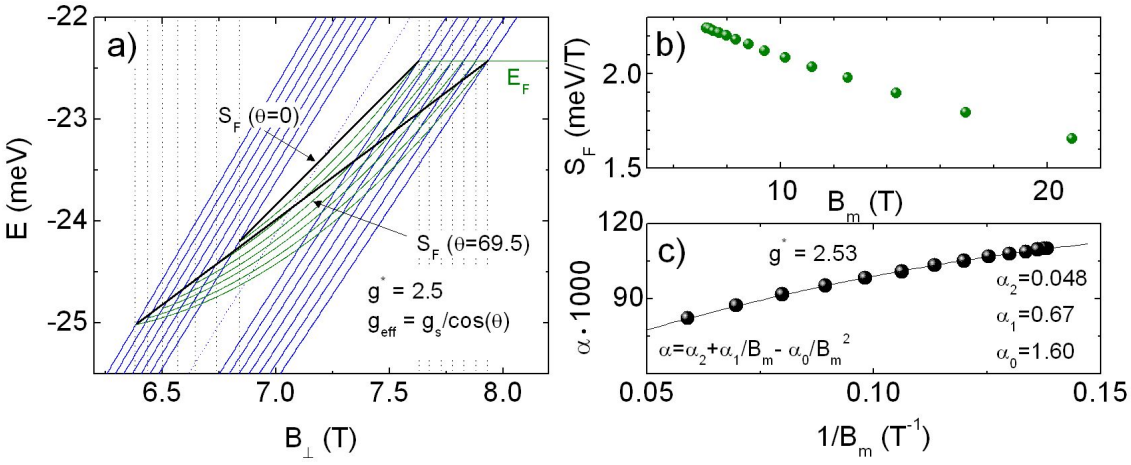

Fig. 6.5: ***a)*** *Simple model, described in the text, which allows to illustrate the Fermi energy movement S_F and therefore the parameter $\alpha(B_m)$, required to reproduce the non quadratic behaviour of the magnetic field splitting ΔB as a function of the total magnetic field B_m.* ***b)*** *Magnetic field dependence of S_F obtained from the SWM calculations presented in a).* ***c)*** *Calculated dependence of the parameter $\alpha = g^*\mu_B/(S_N - S_F)$ as a function of $1/B_m$ with $g^* = 2.53$. The solid line is fitted using a second order polynomial.*

$N = 1$ electron Landau band. Here, $\alpha = g^*\mu_B B/(S_N - S_F)$ is calculated using $g^* = 2.5$, $S_N = 3.576$ meV/T and $S_F(B_m)$, extracted from Fig. 6.5 b). $\alpha(1/B_m)$ is well approximated by a second order polynomial (solid line) with the coefficients shown in Fig. 6.5 c). Substituting the second order polynomial for α in Eq. (6.3) gives,

$$\Delta B \approx \frac{1}{B_\perp^N}(\alpha_2 B_m^2 + \alpha_1 B_m - \alpha_0). \tag{6.5}$$

The predicted variation of ΔB versus B_m for the $N = 1$ electron Landau band, calculated using the coefficients α_0, α_1 and α_2 given in Fig. 6.5 c) is indicated by the solid line in Fig. 6.3 a). The agreement between the data and the simple model is remarkable confirming our hypothesis that the observed deviation from the simple $\Delta B \propto B_m^2$ dependence is due to the movement of the Fermi energy S_F which in turn leads to a magnetic field (angular) dependence of the dimensionless parameter α.

6.1.6 Conclusion

Magnetotransport measurements have been analyzed using the full Slonczewski, Weiss and McClure band structure calculations for graphite in a magnetic field. Using tilted magnetic fields to tune the Zeeman energy, we extract an effective g-factor $g^* = 2.5 \pm 0.1$ for both the electron and hole Landau bands. This is significantly larger than the g-factor obtained using electron spin resonance showing the importance of many body effects in graphite.

6.2 Charge density wave (CDW) phase

In the second part of this chapter the charge density wave phase observed in the magnetoresistance of graphite at high magnetic fields and at low temperatures is discussed. The charge density wave phase manifests itself in a sharp increase of the magnetoresistance at high magnetic fields [26]. Here we extend temperature dependent measurements of the charge density wave phase presented recently by Yoshioka and Fukuyama in Ref. [27] for temperatures $T \geq 1.1$ K to lower temperatures ($T \leq 1.0$ K).

6.2.1 Results and discussions

Fig. 6.6 a) shows the transverse magnetoresistance ρ_{xx} of Kish graphite at different temperatures between $T = 1.1$ K and $T = 10$ K measured by Yoshioka and Fukuyama in pulsed magnetic fields up to $B = 55$ T [27]. Kish graphite, which is artificially grown by precipitation from carbon saturated molten iron or nickel [95], has a lower crystal ordering than HOPG [96], but exhibits more distinct features associated to the charge density wave transition [87]. The reason for this remains to be explained. In the magnetic field range $3 \leq B \leq 7$ T the well documented quantum oscillations are observed [10,11,59,73,78,83]. For temperatures below $T = 10$ K a sharp resistance increase, attributed to the electronic phase transition of the field induced density wave state, is clearly seen (marked by arrows). Both the onset magnetic fields and the resistance jumps in the very vicinity of the onset magnetic fields decrease with the temperature. The complicated behaviour of the resistance at higher magnetic fields is not discussed at this point.

For a comparison, Fig. 6.6 b) shows our data of HOPG. The measurements were performed using a 28 T resistive magnet and a ^{3}He/^{4}He dilution fridge with a base temperature of about $T_b \approx 30$ mK. The magnetoresistance R_{xx} in the magnetic field range $B = 0 - 28$ T is given for different temperatures between $T = 50$ mK and 900 mK. For illustration reasons the offset between the magnetoresistance curves is $R = 1.4\ \Omega$. The temperature values are not exact values as the temperature of the mixing chamber slowly increased during the sweep. However, knowing the temperatures before and after the sweep ($0 \rightarrow 28 \rightarrow 0$ T), the exact temperatures for given magnetic fields can be estimated by linear interpolation. The onset magnetic field for the charge density wave state is marked by arrows. The increase of the resistance is only very weak. As mentioned before, this is in agreement with Ref. [87], in which it is stated that the increase of the resistance associated to charge density wave transition are less distinct in HOPG than in Kish graphite. Moreover in the vicinity of the onset magnetic fields the resistance jumps decrease with temperature (Fig. 6.6 a)).

To study the phase transition in more detail, Fig. 6.7 a)-c) shows a zoom in on $R_{xx}(B)$ in the magnetic field region of the charge density wave onset magnetic field. As the onset magnetic fields are not very distinct in the raw data (left axis), we also show the first derivative dR_{xx}/dB (right axis). The onset magnetic fields, marked by arrows, reveal themselves as maxima in the first derivative.

The phase diagram of Fig. 6.7 d) shows for the different temperatures the onset magnetic fields both for our data (HOPG, $T \leq 1$ K) and the data of Yaguchi and Singleton (Kish graphite, $T \geq$

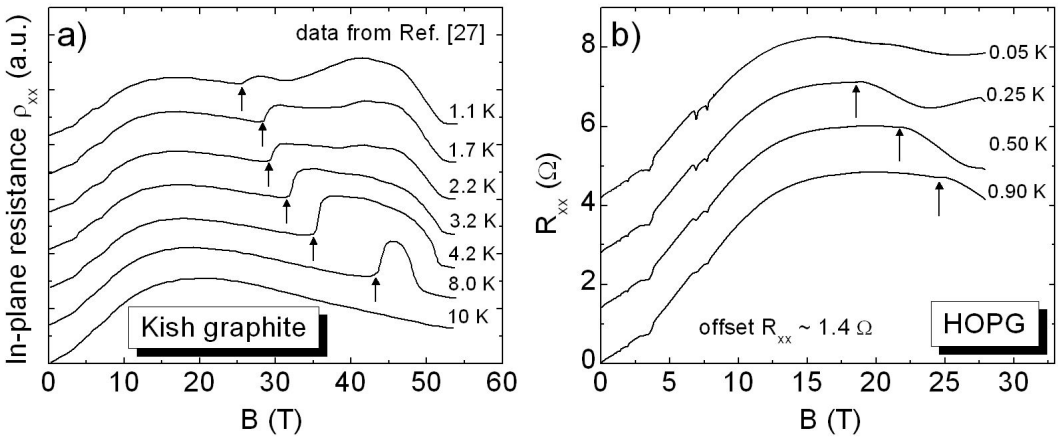

Fig. 6.6: ***a)*** *Magnetoresistance data of Yoshioka and Fukuyama [27] performed on Kish graphite in pulsed magnetic fields up to $B = 55$ T for temperatures between $T = 1.1$ K and 10 K. The temperature dependent onset magnetic field of the charge density wave phase is marked by arrows.* ***b)*** *Our data of HOPG obtained using a 28T resistive magnet and a $^3He/^4He$ dilution fridge. The magnetic fields of the electronic phase transition for the different temperature sweeps are marked by arrows. The increases of the resistance associated to the charge density wave transition are less distinct in HOPG than in Kish graphite, in accordance with Ref. [87].*

1.1 K, [27]). Our data seems to follow the same temperature-magnetic field dependence. The solid curve employed through the data indicates the phase boundary between the normal state and the charge density wave state and is empirically expressed by the formula

$$T_c(B) = T^* \exp\left(-\frac{B^*}{B_{CDW}}\right), \tag{6.6}$$

where T^* and B^* are adjustable parameters. We find $T^* = 113 \pm 1$ K and $B^* = 113 \pm 0.5$ T, which is comparable to what was found in previous studies [87–89]. Eq. (6.6) has the same form as the Bardeen-Cooper-Schrieffer (BCS)-type formula which describes the transition temperature between the normal conducting state and the superconducting state [92].

A detailed explanation of the charge density wave state is beyond the scope of this thesis. Here we limit ourselves to summarize the most important results. The description of the high magnetic field phase as a charge density wave was proposed by Yoshioka and Fukuyama [91], considering the quasi-one-dimensionality of the energy spectrum caused by the Landau level quantization. We have seen in the previous chapter that for high magnetic fields $B > 8$ T graphite is in its quantum limit, with only the lowest electron ($N = 0$) and hole ($N = -1$) sub-band being populated. Electron phonon coupling, which acts as a perturbation, opens a gap Δ at the Fermi energy (Peierls transition) [97]. If $k_B T \gg \Delta$, the electrons can easily overcome the gap and graphite is found in its normal state. Lowering the temperature a point is reached at which the electrons cannot overcome

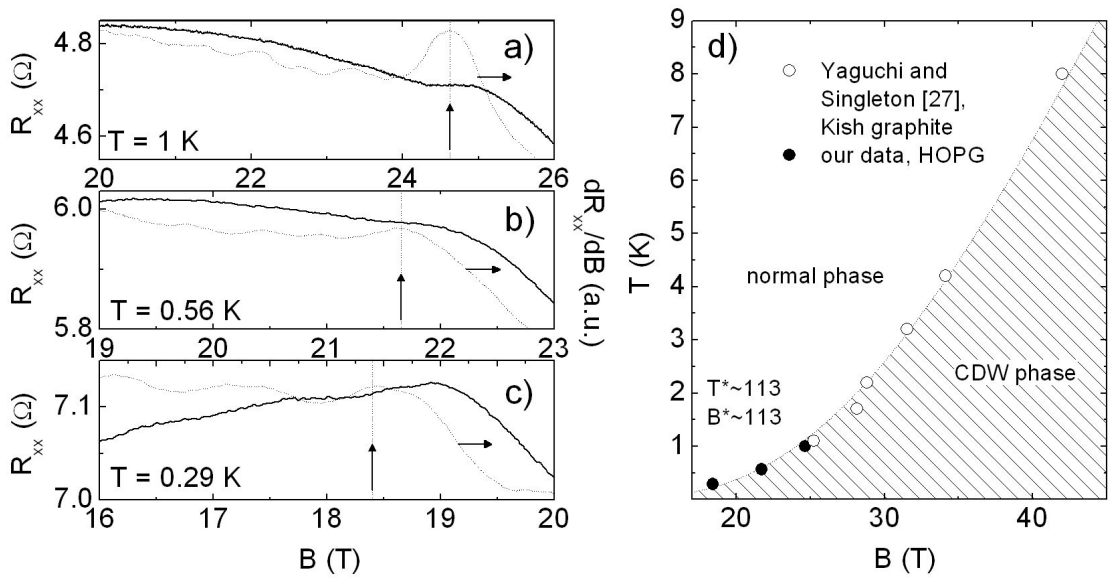

Fig. 6.7: ***a)-c)*** *Zoom in on the magnetic field regions at which the onset of the charge density wave state is observed for the different temperatures. While the transition to the charge density wave state is difficult to see in the raw data R_{xx} (left axis), it manifests itself clearly in dR_{xx}/dB (right axis).* ***d)*** *Phase diagram of graphite in the B-T plane showing the transition from the normal phase to the charge density wave phase. Our data (●) follow the same behaviour as the data of Yoshioka and Fukuyama [27] (○), i.e., the phase transition can be described by a BCS-type formula (6.6).*

the gap anymore and a collective mode is formed by electron and hole pairs.

6.2.2 Conclusion

Our data of HOPG is consistent with the findings of Ref. [27] that the critical temperature at which the sharp increase of the resistance is observed is linked to the applied field by a Bardeen-Cooper-Schrieffer (BCS)-type formula.

7 de Haas-van Alphen effect

Résume du chapitre

Nous avons étudié l'effet de Haas-van Alphen dans le graphite à $T = 400$ mK en utilisant la méthode de couple. Par analogie avec des mesures de magnétotransport nous avons effectué quelques mesures de Haas-van Alphen en haute résolution aux champs magnétiques faibles. Le champ magnétique auquel les oscillations quantiques commencent est $B_0 = 63$ mT. En ce qui concerne les fréquences et les phases on trouve les valeurs $B_{F,h} = 4.62$ T, $\varphi_{0,h} = -0.56 \pm 0.05$ et $B_{F,e} = 6.32$ T, $\varphi_{0,e} = -0.48 \pm 0.05$. Ces valeurs sont très similaires à celles obtenues en magnétotransport.
Nous avons également effectué des mesures en champs magnétiques inclinés pour sonder la surface de Fermi. Les fréquences en fonction du champ magnétique se déplacent comme $1/cos(\theta)$ vers des champs magnétiques plus élevés. Le comportement quasi-bidimensionel peut être expliqué par l'extrême anisotropie du graphite, le couplage dans le plan étant beaucoup plus grand que le couplage entre les plans ($\rho_c \gg \rho_{ab}$) [28]. Le comportement quasi-bidimensionnel est en accord avec le modèle SWM, qui prédit des surfaces de Fermi quasi-cylindriques pour $\theta < 60^\circ$ dans les régions des électrons et trous majoritaires.

In this chapter magnetization measurements of graphite using a capacitive torquemeter are presented. Even though the measurements were performed at $T = 0.4$ K (due to limitations of the experimental setup that time), the data of the quantum oscillations are comparable or even better than the mK magnetotransport data. A phase/frequency analysis of the background removed data gives the same result as for magnetotransport. Preliminary tilted field measurements show that the capacitive torquemeter method is an ideal tool to map out the Fermi surface of graphite.

7.1 Experiment

For the magnetization measurements we used the same mm-size pieces of natural graphite as discussed in the previous chapters. The graphite samples were mounted on the circular plate of the capacitive torquemeter with vacuum grease (see Chapter 4.5). Two different cantilevers with

the dimensions 5 mm $\times$ 125 μm $\times$ 125 μm (length$\times$width$\times$hight) and 5 mm 125 μm $\times$ 50 μm were used. These cantilevers are referred to as *cantilever A* and *cantilever B*, respectively. Whereas the more rigid cantilever A was used for magnetization measurements in the magnetic field range $-3 \leq B \leq 3$ T, the more flexible cantilever B was used for high sensitive measurements at low magnetic field ($B < 0.21$ T). The measurements were performed using a 16 T superconduction magnet and a dilution fridge, equipped with an *in situ* rotation stage. The temperature was $T \approx 0.4$ K. This quite high temperature was a result of the high thermal conductivity of the coaxial cables in the prototype version of the probe, which resulted in a heat transfer to the mixing chamber of the dilution fridge, preventing the base temperature of the dilution fridge ($T_b \approx 10$ mK) ever being reached. The torque signal was measured with a lock-in amplifier using conventional phase sensitive detection at 5.3 Hz (Fig. 4.4).

7.2 Results and discussion

7.2.1 Magnetization of graphite

The torque signal in units of 10^{-4} V as a function of the magnetic field in the range $-3 \leq B \leq 3$ T for various orientations between $\theta = 4^\circ$ and $\theta = 56^\circ$ (with $\theta = 0^\circ$ for $(B \perp ab)$) is shown in Fig. 7.1 a). The measurements were performed using the more rigid cantilever A. The restriction to angles $\theta \geq 4^\circ$ results from the fact that the torque on the cantilever $\boldsymbol{\tau} = \mathbf{M} \times \mathbf{B} = MB \cdot \sin(\theta)$ becomes zero for small angles. The limitation to tilt angles $\theta \leq 56^\circ$ is due to the construction of the

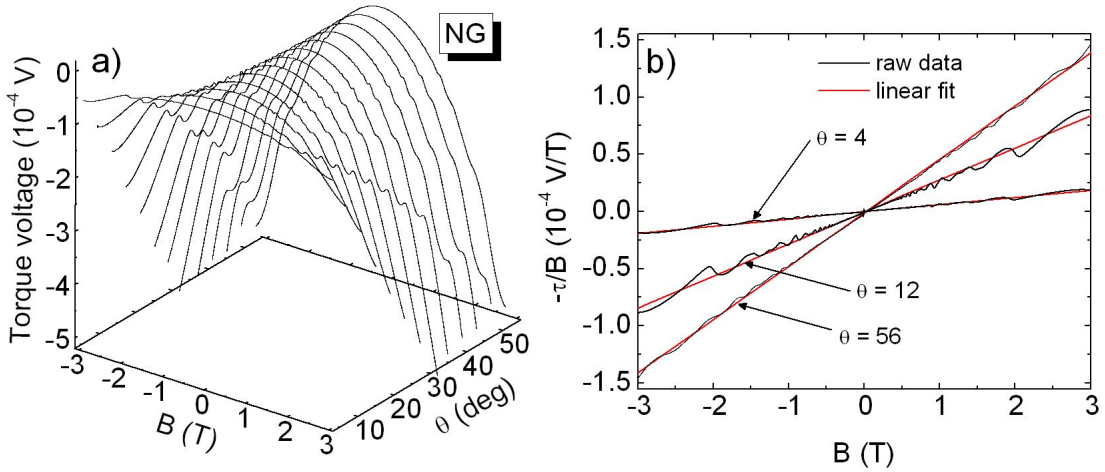

Fig. 7.1: ***a)*** *Torque voltage V as a function of the magnetic field in the range $-3 \leq B \leq 3$ T for various orientations between $\theta = 4^\circ$ and $\theta = 56^\circ$.* ***b)*** *$-\tau/B$ as a function of the magnetic field for selected tilt angles (4°, 12°, 56°). $-\tau/B$, which is proportional to the magnetization M, is a linear function of the magnetic field (indicated by the linear fits of the data).*

sample holder, which did not allow to measure higher angles at the time the measurements were performed. Having a small value at $B = 0$ T, the absolute value of the torque voltage V strongly increases with the strength of the magnetic field. The curves have a nearly perfect dependence on B^2, which is a result of the linear dependence of the magnetization on the magnetic field (discussed subsequently). Note that the sign of the torque voltage reflects the fact that the cantilever bends towards the ground plate of the capacitance bridge. The small quantum oscillations superimposed on the large magnetization background are discussed later on in this chapter.

In Chapter 4.5 it was discussed that the torque voltage is linked to the out-of-plane magnetization $M_{\parallel}$ by the torque equation (4.2)

$$\tau = -\frac{1}{B_F}\frac{dB_F}{d\theta}M_{\parallel}B, \tag{7.1}$$

where B_F is the angle dependent fundamental frequency of the oscillations. For a given angle θ, the magnetization is therefore proportional to $-\tau/B$. $M \propto -\tau/B$ as a function of the magnetic field ($|B| < 3$ T) is shown in Fig. 7.1 b) for three different angles (4°, 12°, 56°). Neglecting the superimposed quantum oscillations, $-\tau/B(\theta)$ are linear functions of the magnetic field as indicated by the linear fits of the data. This result is confirmed e.g. in Refs. [98, 99]. The linearity of $-\tau/B$ as a function of the magnetic field results in $\tau \propto B^2$ which is observed in Fig. 7.1 a).

Graphite has the largest value of diamagnetism among all known materials ($B\|c$) [28]. Qualitatively the large diamagnetism of graphite can be explained in the following way: When the magnetic field is turned on, groups of states, which were originally distributed in energy, condensate on Landau bands with discrete energies. This raises the total energy of the electrons [100] which leads, considering the definition of the magnetization,

$$M = -\frac{1}{V}\frac{\partial E}{\partial B},$$

to the diamagnetism of the material. The band energy of graphite varies in a first approximation as $E_N = \hbar\omega_c(N+1/2)$, with $\omega_c = \hbar B/e$ being the cyclotron frequency. The extremely small effective mass of $m^* \approx 0.05$ for electrons and $m^* \approx 0.039$ for holes [16, 57, 76, 101, 102] results in a strong variation of the band energies with the magnetic field and therefore in a large diamagnetism. A qualitative explanation of the high diamagnetism of graphite is given by McClure, both on the basis of a simple two-dimensional energy spectrum (graphene) and the full SWM-model [23, 103].

7.2.2 Quantum oscillations

In this section the quantum oscillations superimposed on the large magnetization background are discussed. Fig. 7.2 a) shows the torque voltage V measured with the more flexible cantilever B between $B = 0 - 0.21$ T at $T \approx 400$ mK with a sweep rate of $dB/dt = 0.002$ T/min. The angle between the sample plane and the magnetic field was $\theta = 16°$. In this region of the tilt angle, the signal due to the quantum oscillations is strongly enhanced, as discussed subsequently. The quantum oscillations can be observed in the raw data for $B > 0.08$ T (see inset).

As for the Shubnikov-de Haas oscillations in magnetotransport, the de Haas-van Alphen oscillations can be better observed in the background removed data. Here we use again the method of removing the background by subtracting a smoothed (moving window average) data curve. Fig. 7.2 b) shows ΔV between $B = 0 - 0.21$ T. The onset magnetic field of the quantum oscillations is $B_0 = 66$ mT ($\theta = 16°$) which translates to $B_0 \cdot \cos(\theta) \approx 63$ mT in the $\theta = 0°$ configuration. The features observed at lower magnetic field are probably due to noise. The onset magnetic field of the quantum oscillations is lower than that of $B_0 = 70$ mT of the magnetotransport data measured at mK temperatures (Chapter 5.2). Considering the much higher temperature at which the de Haas-van Alphen measurements were performed, it can be concluded that the torque method is more sensitive to quantum oscillations than magnetotransport measurements. Compared to the de Haas-van Alphen measurements, which probe pure thermodynamics, the magnetotransport is influenced by scattering processes at the Fermi energy, which reduce the signal of the oscillations.

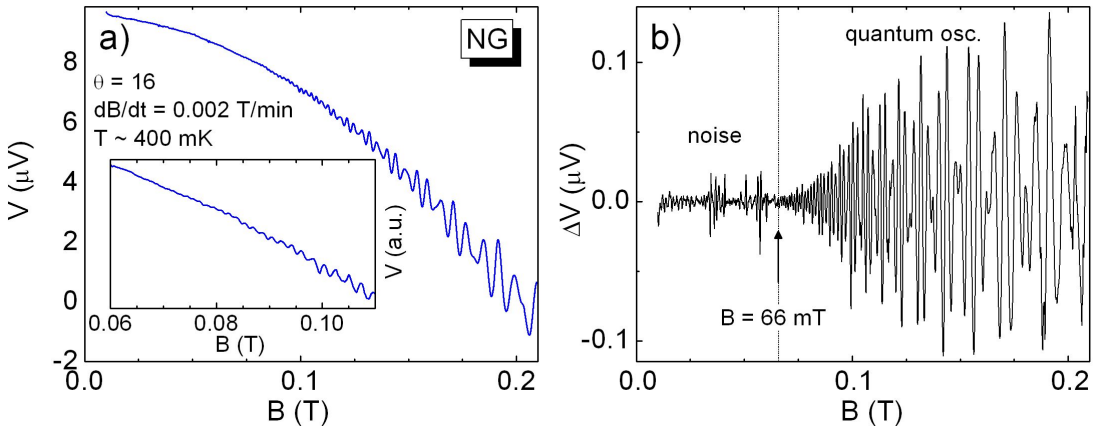

Fig. 7.2: ***a)*** *Torque voltage as a function of the magnetic field between $B = 0 - 0.21$ T measured at $T \approx 400$ mK for $\theta = 16°$ with an extremely slow sweep rate of $dB/dt = 0.002$ T/min. (Inset:) The quantum oscillations can be observed in the raw data at $B_0 > 0.08$ T.* ***b)*** *Background removed data $\Delta V(B)$. The small value of the onset magnetic field of the quantum oscillations ($B_0 = 66$ mT) indicates the high quality of the de Haas-van Alphen measurements using the torque method.*

7.2.3 Phase/frequency analysis of quantum oscillations

The same method as for Shubnikov-de Haas oscillations to extract the phase and the frequency was used for the analysis of the de Haas-van Alphen oscillations of Fig. 7.2 b). As discussed before, the method is based on the phase shift function $K(\varphi,B) = \Re\left[e^{i\varphi}\tilde{F}(B)\right] = \cos(\varphi-\varphi_0)F(B)$, where the fundamental frequency B_F and the phase φ_0 reveal themselves as maxima in the $\varphi - B$ plane [73]. To begin with, Fig. 7.3 a) shows the spectral intensity of the Fourier transformation. Both, the electron and hole features, are very distinct. No additional feature is observed at $B \approx 0.3$ T, which is the magnetic field at which minority carriers are expected (not shown, see discussion in Chapter 5.6). The frequency values of $B_{F,h} = 4.62$ T and $B_{F,e} = 6.32$ T for electrons and holes, respectively, have to be corrected by the tilt angle $\theta = 16°$. One obtains $B_{F,h} = 4.44$ T and $B_{F,e} = 6.08$ T. These values are very similar to those obtained for the mK magnetotransport data ($B_{F,h} = 4.51$ T and $B_{F,e} = 6.14$ T, see Chapter 5.3). The phase shift function $K(\varphi,B)$ is plotted in Figs. 7.3 b) and c) in the regions of the hole and electron features, which are known from the Fourier analysis. The phase values in units of 2π obtained from the maxima are $\varphi_{0,h} = -0.56 \pm 0.05$ and $\varphi_{0,e} = -0.48 \pm 0.05$ for holes and electrons, respectively. These values are as well very similar to $\varphi_{0,h} = -0.43 \pm 0.05$ and $\varphi_{0,e} = -0.28 \pm 0.05$ of the mK magnetotransport data. This is at first sight surprising, since according to Eqs. (2.27) and (2.20) Adams and Holstein predict a phase shift of $\pi/2$ between Shubnikov-de Haas and de Haas-van Alphen oscillations. Note, however, that this phase shift is compensated by the $-\pi/2$ phase shift of the impedance of the capacitor.

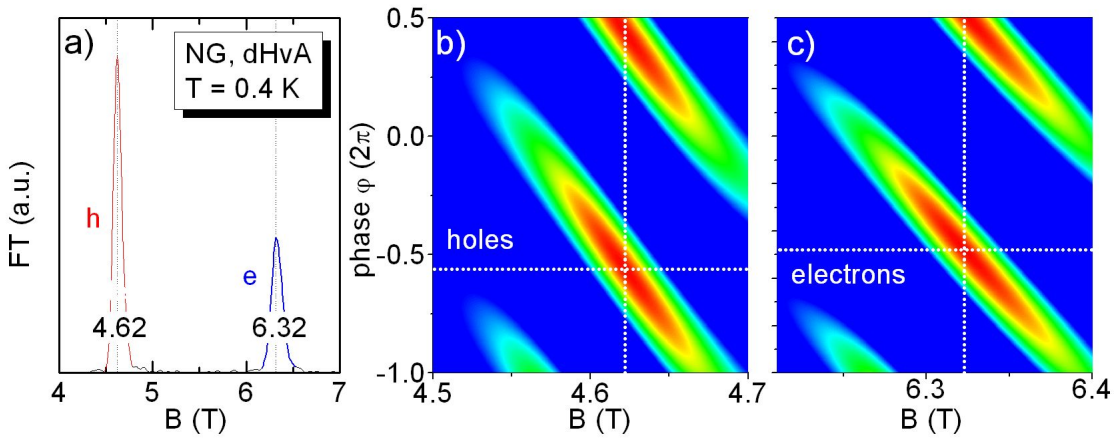

Fig. 7.3: ***a)*** *Spectral intensity of the de Haas-van Alphen data $\Delta V(B)$ of Fig. 7.2. The frequency values corrected by the tilt angle $\theta = 16°$ are $B_{F,e} = 6.08$ T and $B_{F,h} = 4.44$ T for electrons and holes, respectively. These values are very similar to those obtained for the mK magnetotransport data ($B_{F,h} = 4.51$ T and $B_{F,e} = 6.14$ T, see Chapter 5.3).* ***b)*** *and* ***c)*** *Phase shift function in the $\varphi - B$ plane. The phase values $\varphi_{0,h} = -0.56 \pm 0.05$ and $\varphi_{0,e} = -0.48 \pm 0.05$ for holes and electrons, respectively, are as well very similar to those of the mK magnetotransport data.*

7.2.4 Mapping out of the Fermi surface of graphite

The high quality of the de Haas-van Alphen data allows to precisely map out the Fermi surface. It was shown before in Fig. 6.2 and for example in Refs. [11, 13] that for angles up to $\theta = 70°$, $B_F(0)/B_F(\theta)$ for electrons and holes can be described to a good approximation by a $\cos(\theta)$ dependence. The quasi-two-dimensional behaviour can be explained by the extreme anisotropy of graphite, i.e., the in–plane coupling is much bigger than the out of plane coupling ($\rho_c \gg \rho_{ab}$) [28]. The quasi-two-dimensional behaviour is consistent with the SWM-model, which predicts for $\theta < 60°$ quasi-cylindrical Fermi surfaces in the regions of the majority electron and hole pockets. For higher angles, deviations from the $\cos(\theta)$ dependence are expected. Those deviations, however, could not be observed in our magnetotransport data (Fig. 6.2) and previous publications [11, 13] due to the scatter in the data.

Fig. 7.4 shows the spectral intensity as a function of the magnetic field for various angles. The spectral intensity was obtained from the Fourier transform of the data presented in Fig. 7.1 a) after removing the background. The series of all three features observed in the magnetic field region between $B = 3 - 12$ T (holes, electrons and first harmonic of the hole features) shift as a function of $1/\cos(\theta)$ to higher magnetic fields (solid lines in the $B - \theta$-plane). The spectral intensities as a function of the tilt angle increase at first and reach their maximum values for angles between $\theta = 20°$ and $\theta = 30°$. This increase can be explained with the torque equation (7.1). Knowing

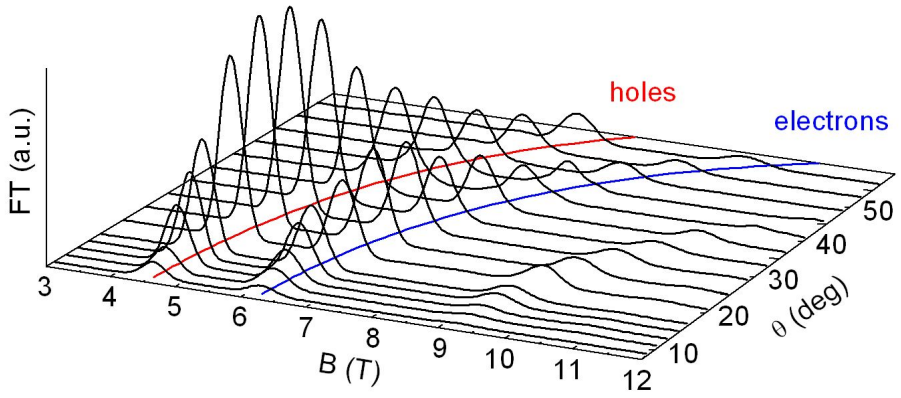

Fig. 7.4: *Spectral intensity of the Fourier transform obtained from the background removed data $\Delta V(B)$ as a function of the magnetic field for various angles between $\theta = 4°$ and $\theta = 56°$. The series of all three features observed in the magnetic field region between $B = 3 - 12$ T (holes, electrons and first harmonic of the hole features) shift as a function of $1/\cos(\theta)$ to higher magnetic fields (solid lines in the $B - \theta$-plane). The features have their maximum values between $\theta = 20°$ and $\theta = 30°$.*

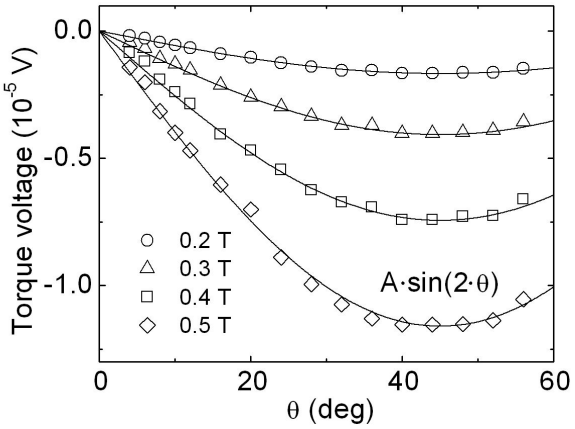

Fig. 7.5: *Torque voltage as a function of the angle for given magnetic fields between $B = 0.2$ T and $B = 0.5$ T, which corresponds to the magnetic field region in which the quantum oscillations are much smaller than the large background magnetization. The data can be explained nearly perfectly by the function $A \cdot sin(2\theta)$, a results which can be derived from the torque equation (7.1) knowing that the fundamental frequency of the oscillations as a function of θ is $B_F(0)/cos(\theta)$.*

that $B_F(0)/B_F(\theta) \approx \cos(\theta)$ and $M = \alpha \cdot B$ (see Fig. 7.1 b)), the torque equation (7.1) becomes

$$\tau = -\frac{\cos(\theta)}{B_F(0)} \frac{-\sin(\theta)B_F(0)}{\cos^2(\theta)} \alpha B_0^2 \cos^2(\theta) = \frac{\alpha B_0^2}{2} \sin(2\theta), \tag{7.2}$$

i.e., the torque signal increases with $\sin(2\theta)$. This behaviour is confirmed in Fig. 7.5 in which we plot the torque voltage as a function of the angle for given magnetic fields between $B = 0.2$ T and $B = 0.5$ T. In this magnetic field region the quantum oscillations are much smaller than the large background magnetization. The solid lines represent a curve of the form $A \cdot \sin(2\theta)$, which fit the data nearly perfectly.

With the increasing torque signal for increasing angles θ, the signal of the quantum oscillations increases as well. This explains the increase of the spectral intensity. For angles $\theta > 30°$, the features of the spectral intensity decrease. This can be explained by the fact that the quantum oscillations are increasingly hidden by the large background magnetization. Moreover, fewer quantum oscillations are observed in the magnetic field region $-3 \leq B \leq 3$ T for high angles.

Fig. 7.6 shows the top view of the spectral intensity plot after interpolating the various curves for different angles. The solid lines represent the curves $B_F(0) \cdot \cos(\theta)$. They nearly perfectly fit the data for angles $\theta < 40°$. For higher angles deviations of the spectral intensity peaks from the $\cos(\theta)$ behaviour towards lower magnetic fields are observed. The dotted lines represent the curves $B_F(0)/\cos(\theta - 1°)$, which consider a misalignment of the sample by $\theta = 1°$ on the rotation stage. The corrected curves give better fits to the high angle data, but fit the data $\theta < 40°$ less perfectly. We are unable to determine if the failure of the $B_F(0)/\cos(\theta)$ curve to fit the data over the whole range in the θ-B-plane should be ascribed either to deviations from the cylindrical Fermi

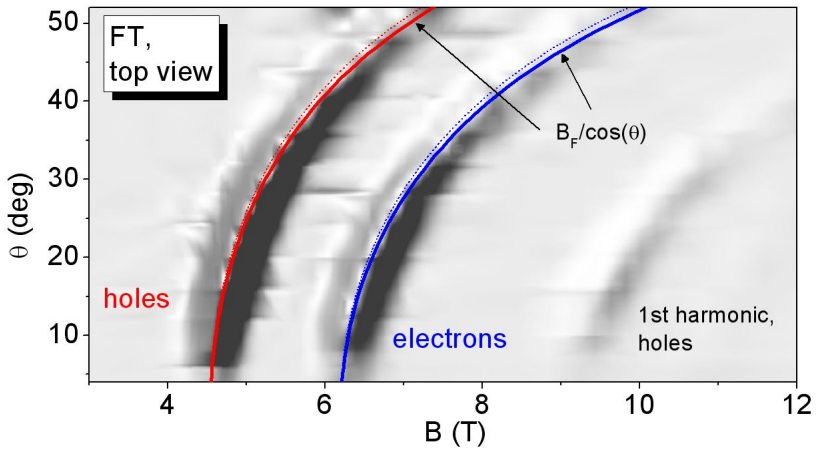

Fig. 7.6: *Top view of the spectral intensity plot after interpolating the various curves for different angles. The solid lines represent the curves $B_F(0)/cos(\theta)$ with $B_{F,e}(0) = 4.55$ T and $B_{F,h}(0) = 6.2$ T for the electron and hole features, respectively. The deviations from the $1/cos(\theta)$ behaviour for $\theta > 40°$ could either be explained by a misalignment of the sample by an angle of $\theta \approx 1°$ or deviations from the cylindrical Fermi surface predicted by the SWM-model for high angles.*

surface at high angles, which is predicted by the SWM-model, or to a misalignment of the sample. To answer this question de Haas-van Alphen measurements at higher angles are required.

7.3 Summary and Conclusion

In this chapter de Haas-van Alphen measurements of natural graphite using a capacitive torquemeter were presented. The quality of the data measured at $T \approx 0.4$ K with the cantilever A is comparable to or even better than the magnetotransport data of natural graphite measured at mK temperatures. The big advantage of the de Haas-van Alphen measurements concerns the mapping of the Fermi surface. The fact that the torque signal follows a $A \cdot \sin(2\theta)$ behaviour, i.e., the signal of the spectral intensity first increases with increasing tilt angle, results in an increase of the amplitude of the quantum oscillations when the magnetic field is tilted away from the c-axis of graphite. For higher tilt angles the signal increases as the quantum oscillations are hidden by the large background magnetization. However, in the region where the background magnetization has its maximum value (at $\theta \approx 45°$), the quantum oscillations are still clearly visible. It is expected that for higher tilt angles, the spectral intensity of the features increases again, as the magnetization background, which superimposes the quantum oscillations, decreases for $\theta > 45°$ (see Fig. 7.5). We can therefore expect that the Fermi surface can be mapped out with high precision up to $\theta > 80°$. Moreover, we expect that measurements at mK temperatures considerably improve the signal. This has not only been observed for our magnetotransport data, but also recently for de Haas-van Alphen measurements of graphite using the torque method [104].

8 Summary

Résume du chapitre

Dans cette thèse le magnétotransport à basse température ($T \approx 10$ mK) et l'effet de Haas-van Alphen ($T \approx 0.4$ K) ont été examinés pour le graphite naturel et le graphite HOPG. Dans la première partie, le magnétotransport pour des champs magnétiques allant jusqu'à $B = 11$ T est présenté. Une analyse de Fourier de ΔR_{xx} (signal après soustraction du fond de magnétorésistance) montre que le transport électrique dans le graphite est dominé par deux types de porteurs avec des fréquences et des phases en accord avec le modèle SWM. Nous avons confirmé la validité du modèle SWM par des calculs détaillés de la structure de bande sous champ magnétique. Le mouvement de l'énergie de Fermi pour $B > 2$ T a été calculée d'une manière auto-cohérente en supposant que la somme des concentrations des électrons et des trous est constante. En outre nous avons confirmé la transition métal isolant découverte dans le graphite récemment. Une recherche systématique des oscillations de porteurs minoritaires à bas champ magnétique ($B < 0.3$ T) s'est avérée infructueuse.

Des mesures sous champs magnétiques intenses ($0 \leq B \leq 28$ T) ont été employées pour étudier l'effet Zeeman et la phase de l'onde de densité de charge. En ce qui concerne l'effet Zeeman, les calculs SWM incluant le mouvement de l'énergie de Fermi nécessitent un facteur de Lande $g^* = 2.5 \pm 0.1$ pour reproduire la séparation de spin observée dans les données. Les mesures de l'onde de densité de charge ont confirmés que le champ magnétique auquel celle-ci apparait est lié à la température par une formule de type Bardeen-Cooper-Schrieffer (BCS). Les mesures de l'effet de Haas-van Alphen ont confirmé les résultats obtenus par de magnétotransport à bas champ.

Interest in graphite has been renewed by the recent investigation of graphene, which shows remarkable physical properties due to the presence of Dirac like charge carriers with a zero rest mass. Historically, graphene forms the starting point for the Slonczewski, Weiss and McClure (SWM) band structure calculations of graphite [2, 3]. In graphite, the Bernal stacked graphene layers are weakly coupled with the form of the in-plane dispersion depending upon the momentum k_z in the direction perpendicular to the layers. The carriers occupy a small region along the H-K-H edge of the hexagonal Brillouin zone. At the K point ($k_z = 0$), the in-plane dispersion of

the electron pocket is parabolic (massive fermions), while at the H point ($k_z = 0.5$) the dispersion of the hole pocket is linear (massless Dirac fermions). The Fermi surface along the edge H-K-H is made up of one electron pocket and four hole pockets. Two of the latter are placed directly at the H points. Techniques such as magnetotransport and de Haas-van Alphen measurements, which probe the density of states at the Fermi energy, are linked to extremal cross sections of the Fermi surface. Two types of majority carriers are expected: Majority electrons at the K point ($k_z = 0$) and majority holes with $k_z \approx 0.3$ close to the H point ($k_z = 0.5$). Both charge carriers are massive, having a parabolic in-plane energy spectrum. The additional hole pockets at the H points ($k_z = 0.5$) with a small cross section give rise to groups of massless minority holes with a linear in-plane dispersion relation, similar to the charge carriers in graphene.

In this thesis, low-temperature magnetotransport and the de Haas-van Alphen effect of both natural graphite and highly oriented pyrolytic graphite (HOPG) have been examined. In the first part, low field magnetotransport up to $B = 11$ T was discussed.

Preliminary magnetotransport measurements on HOPG at $T = 1.2$ K reveal small quantum oscillations which are superimposed on a large magnetoresistance background. A Fourier analysis of the background removed signal ΔR_{xx} shows that the electrical transport in graphite is governed by two types of charge carriers with fundamental frequencies of $B \approx 4.5$ T and $B \approx 6.2$ T, ascribed to majority electrons and holes, respectively. The same kind of measurements of HOPG and natural graphite were repeated at mK temperatures in a dilution fridge. Natural graphite reveals an extremely rich magnetotransport spectrum, for which orbital quantum numbers up to almost $N = 100$ are observed (features start at a magnetic field of $B_0 = 0.07$ T). Spin splitting is observed for magnetic fields $B_z > 1$ T. HOPG has a similar spectrum, i.e., the positions of the features in magnetic field are essentially the same as for natural graphite. This implies that both types of bulk graphite are very similar and are described by the same physics. Nevertheless, the quality of the natural graphite data is higher than that of HOPG, which can be explained by a higher crystal quality of natural graphite.

The high quality of the magnetotransport data of natural graphite measured at mK temperatures allowed an accurate phase analysis of the quantum oscillations. It was shown that electrons and holes have a so-called Berry phase of $\Phi_B = 0$, which implies that both charge carriers are massive charge carriers.

The effective mass m^* of the holes was extracted from the temperature dependence of quantum oscillations, which is described by the temperature factor R_T (2.22) of the Lifshitz-Kosevich equation. The value of $m^* \approx 0.05$ is similar to the accepted value of $m_e = 0.039 m_e$ [28]. Temperature dependent measurements were furthermore used to confirm the existence of the metal-insulator-transition in graphite, which reveals itself in the longitudinal resistance as a function of the temperature for increasing magnetic fields.

We then demonstrated that the quantum oscillations can be consistently interpreted with the presence of majority electron and hole pockets within the three-dimensional SWM band structure model for graphite. The observed significant deviations of the quantum oscillations from the $1/B$ periodicity at high magnetic fields ($B > 2$ T) are explained by a movement of the Fermi energy as

the quantum limit is approached. The movement of the Fermi energy in magnetic field was calculated self-consistently assuming that the sum of the electron and hole concentrations is constant. The deviations of the quantum oscillations from the $1/B$ periodicity seriously question the validity of using the high field data to extract the phase of the Shubnikov-de Haas oscillations and hence the nature of the charge carriers as it was done by the authors of Ref. [59]. The appearance of a third series of features at low magnetic fields was discussed. Those features are not periodic in $1/B$ and therefore cannot be ascribed to the expected minority carrier oscillations at low magnetic field.

The second part of the thesis dealt with high field magnetotransport of natural graphite in the magnetic field range $0 \leq B \leq 28$ T. Both *spin splitting* of magnetotransport features in tilted field configuration and the onset of the *charge density wave (CDW)* phase for different temperatures with the magnetic field applied normal to the sample plane were discussed. Concerning the charge density wave phase investigation, we extended temperature dependent measurements of the charge density wave onset magnetic field by Yaguchi and Singleton [27] to lower temperatures. Our data follows the same temperature-magnetic field dependence as Yaguchi and Singleton's data, and can be described by a Bardeen-Cooper-Schrieffer (BCS)-type formula, which characterizes the transition temperature between the normal conducting state and the superconducting state.
Concerning the investigation of the spin splitting in graphite, high field magnetotransport in tilted field configuration was used. The splitting of the magnetotransport features for various magnetic fields and angles was reproduced by SWM calculations including the movement of the Fermi energy. The fact that the Fermi energy movement has to be included in the calculations is derived from the fact that the spin splitting ΔB as a function of the magnetic field is not a parabolic function of the magnetic field. We found a g-factor of $g^* = 2.5 \pm 0.1$ for both electrons and holes. The enhancement of this value with respect to the free electron g-factor of $g_s = 2$ is tentatively attributed to many body effects.

Finally we have examined the magnetization of graphite as a function of the magnetic field using a capacitive torquemeter. Even though having been measured at $T = 0.4$ K, the data of the quantum oscillations is comparable to or even better than the mK magnetotransport data. A phase/frequency analysis of the background removed data gives the same result as magnetotransport. Preliminary tilted field measurements show that the capacitive torquemeter method is an ideal tool to map out the Fermi surface of graphite.

A Appendix

A.1 Classical transport theory

The classical description of electronic transport is given by the Drude theory, which applies the theory of a classical Boltzmann gas to the charge carriers in a sample. The charge carriers are assumed to be subject to collisions with impurity atoms or defects. The crucial terms in the Drude theory are therefore the Lorentz force and a nonlinear damping term, depending on the mean time τ between collisions. The equation of the drift acceleration $d\mathbf{v}/dt$ is given by

$$\frac{d\mathbf{v}}{dt} = -\frac{e}{m^*}(\mathbf{E} + \mathbf{v}_d \times \mathbf{B}) - \frac{\mathbf{v}_d}{\tau}, \tag{A.1}$$

where $\mathbf{E}$ is the electric field. In the stationary regime $d\mathbf{v}/dt = 0$, the system of linear equations reads

$$\begin{aligned} -eE_x - \omega_c m^* v_y - \frac{m^* v_x}{\tau} &= 0 \\ -eE_y - \omega_c m^* v_x - \frac{m^* v_y}{\tau} &= 0. \end{aligned} \tag{A.2}$$

The expressions for the resistivities are found using $\mathbf{E} = \bar{\rho}_{\mathbf{xy}} \cdot \mathbf{j}$, where $\bar{\rho}$ is the resistivity tensor and $\mathbf{j} = ne\mathbf{v}$ (n is the charge carrier density). With

$$\begin{pmatrix} E_x \\ E_y \end{pmatrix} = -\frac{m^*}{ne^2\tau} \begin{pmatrix} 1 & \omega_c\tau \\ -\omega_c\tau & 1 \end{pmatrix} \equiv \begin{pmatrix} \rho_{xx} & \rho_{xy} \\ \rho_{yx} & \rho_{yy} \end{pmatrix} \begin{pmatrix} j_x \\ j_y \end{pmatrix},$$

we find

$$\rho_{xx} = \rho_{yy} = -\frac{m^*}{ne^2\tau} \quad \text{and} \quad \rho_{xy} = -\rho_{yx} = -\frac{B}{ne}. \tag{A.3}$$

While ρ_{xx} is independent of the magnetic field, ρ_{xy} is a linear function of B. Both resistivities depend on the carrier density n of the material.

Expressions for the conductivity are found with $\mathbf{j} = \bar{\sigma}_{\mathbf{xy}} \cdot \mathbf{E}$, so that

$$\begin{pmatrix} j_x \\ j_y \end{pmatrix} = -\frac{ne^2\tau}{m^*} \begin{pmatrix} \frac{1}{1+\omega_c^2\tau^2} & -\frac{\omega_c\tau}{1+\omega_c^2\tau^2} \\ \frac{\omega_c\tau}{1+\omega_c^2\tau^2} & \frac{1}{1+\omega_c^2\tau^2} \end{pmatrix} \equiv \begin{pmatrix} \sigma_{xx} & \sigma_{xy} \\ \sigma_{yx} & \sigma_{yy} \end{pmatrix} \begin{pmatrix} E_x \\ E_y \end{pmatrix}.$$

The link between the resistivities and the conductivities ρ_{xx} and σ_{xx} is therefore given by the tensor relations

$$\sigma_{xx} = \frac{\rho_{xx}}{\rho_{xx}^2 + \rho_{xy}^2} \quad \text{and} \quad \sigma_{xy} = \frac{\rho_{xy}}{\rho_{xx}^2 + \rho_{xy}^2} \ . \tag{A.4}$$

Under the assumption that the electronic transport is governed by two types of charge carriers, electrons and holes, σ_{xx} and σ_{xy} are given by [41]

$$\sigma_{xx} = \frac{n_e e \mu_e}{1 + \mu_e^2 B^2} + \frac{n_h e \mu_h}{1 + \mu_h^2 B^2} \quad \text{and} \quad \sigma_{xy} = -\frac{n_e e \mu_e^2 B}{1 + \mu_e^2 B^2} + \frac{n_h e \mu_h^2 B}{1 + \mu_h^2 B^2}, \tag{A.5}$$

where μ_e and μ_h are the charge carrier mobilities. In the extreme quantum limit ($\mu_{e,h} B \gg 1$), the transverse resistivity is determined by the carrier density imbalance,

$$\rho_{xy} = \frac{\sigma_{xy}}{\sigma_{xx}^2 + \sigma_{xy}^2} \approx \frac{B}{e\left(n_h - n_e\right)}. \tag{A.6}$$

For low (non-quantizing) magnetic fields ($\mu_{e,h} B \ll 1$) we can make use of the fact that in a perfect graphite crystal the carrier densities are compensated, $n_e \approx n_h \equiv n$ so that

$$\rho_{xy} \approx \frac{B}{en} \frac{\mu_h - \mu_e}{\mu_h + \mu_e}. \tag{A.7}$$

A.2 Cryogenics

In the following the three different cryogenic systems presented in Chapter 4.3 are discussed.

Before presenting schematically the design of the cryostats, some properties of helium are discussed. Helium comes in two isotopes, the boson ^{4}He and the fermion ^{3}He. The phase diagram of ^{4}He is shown in Fig. A.1 a). It liquefies under atmospheric pressure at $T = 4.2$ K. The vapour pressure drops approximately exponentially when liquid ^{4}He is cooled down and reaches $p = 1$ mbar at $T = 1.2$ K. At $T = 2.17$ K ($p = 1$ bar) the so-called λ line is crossed. For $T > 2.17$ K, ^{4}He behaves like an ordinary liquid and is referred to as *HeI*. For $T < 2.17$ K, it undergoes a phase transition and behaves like a superfluid. The superfluid phase is referred to as *HeII*.
The phase diagram of ^{3}He is sketched in Fig. A.1 b). Under atmospheric pressure the boiling point of ^{3}He is at $T = 3.18$ K, which is about 1 K below that of ^{4}He and can be explained by the lighter mass and therefore a higher average velocity of ^{3}He. Consequently the vapour pressure of ^{3}He is also higher at identical temperatures. At $T = 270$ mK it is $p = 10^{-3}$ bar. As ^{3}He atoms are fermions, the liquid can be treated as a Fermi gas.

A.2.1 ^{4}He cryostat with variable temperature insert - VTI

A schematic sketch of the ^{4}He cryostat with variable temperature insert (VTI) is shown in Fig. A.2 a). As ^{4}He has a small latent heat, i.e., boils off easily, the liquid He cryostat has to be thermally decoupled from the environment. This is achieved by

- separating the helium vessel from the environment by a vacuum, which suppresses heating via thermal convection
- making the liquid helium container of stainless steel, a material with poor thermal conductivity, which reduces the heat load from the top

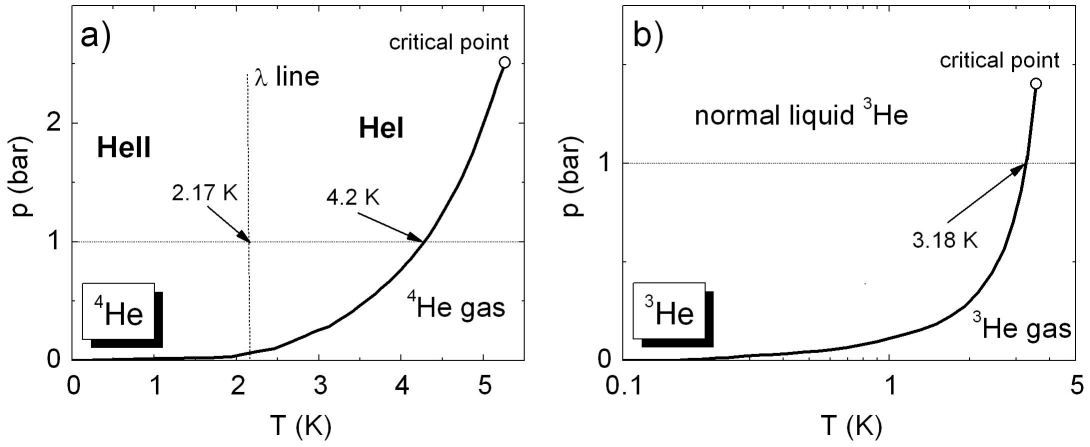

Fig. A.1: ***a)*** *Phase diagram of* ^{4}*He and* ***b)*** ^{3}*He.*

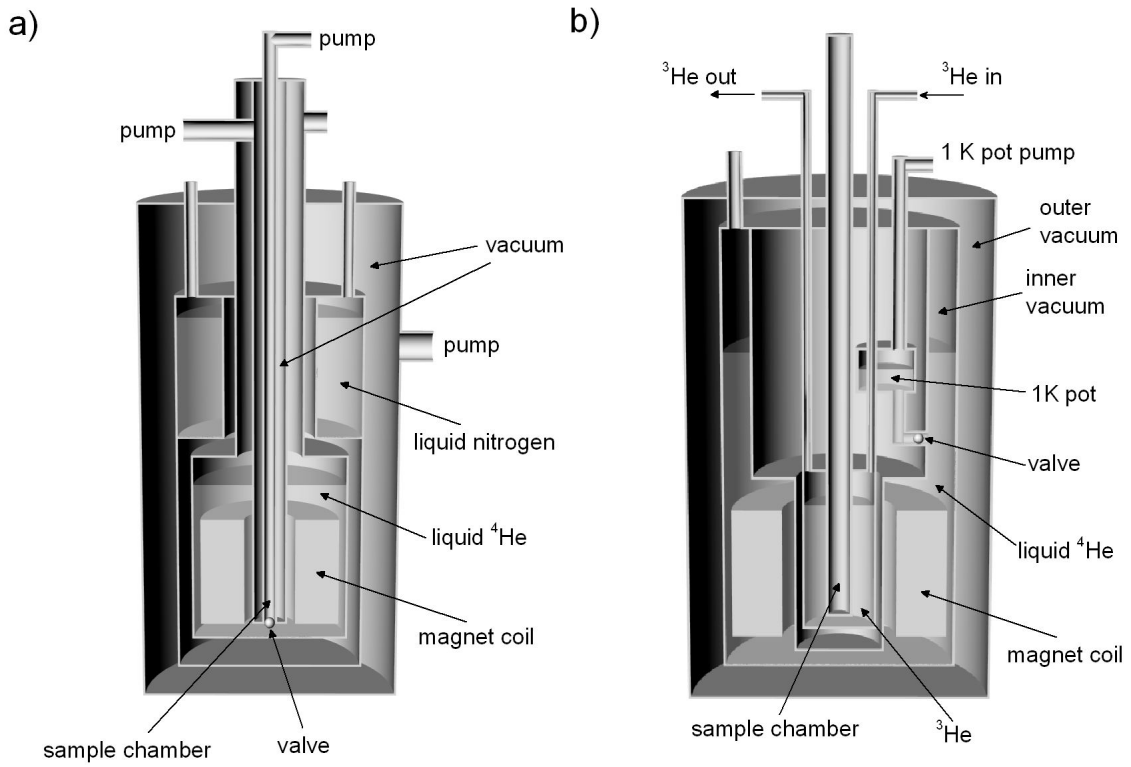

Fig. A.2: ***a)*** *Schematic sketch of a ^{4}He cryostat with variable temperature insert (VTI).* ***b)*** *Sketch of a ^{3}He cryostat.*

- shielding the thermal radiation from the environment by surrounding the liquid He vessel with liquid nitrogen, which reduces the temperature of the radiation entering the helium dewar.

As mentioned above, the temperature of liquid helium at atmospheric pressure is $T = 4.2$ K. However, the liquid helium, which enters the thermally decoupled sample chamber via the needle valve, can be pumped. This causes liquid helium to evaporate and therefore cools the liquid. The lowest possible temperature of our ^{4}He cryostat was $T_b \approx 1.2$ K. At this temperature the vapour pressure of ^{4}He is $p = 1$ mbar. If temperatures above 4.2 K are required, the temperature of the helium gas, which enters the sample chamber, can be adjusted by controlling the power applied to a heater of the gas. The maximal temperature in our ^{4}He cryostat without excessively boiling off helium from the main bath was about 200 K.

A.2.2 ^{3}He cryostat

As the vapour pressure of ^{3}He at temperatures below $T = 1$ K is much higher than that of ^{4}He, ^{3}He cryostats have a lower base temperature than ^{4}He cryostats ($T_b \approx 300$ mK). In a ^{3}He cryostat, the ^{3}He is isolated from the ^{4}He precooling stage by an inner vacuum chamber (Fig. A.2 b)). The

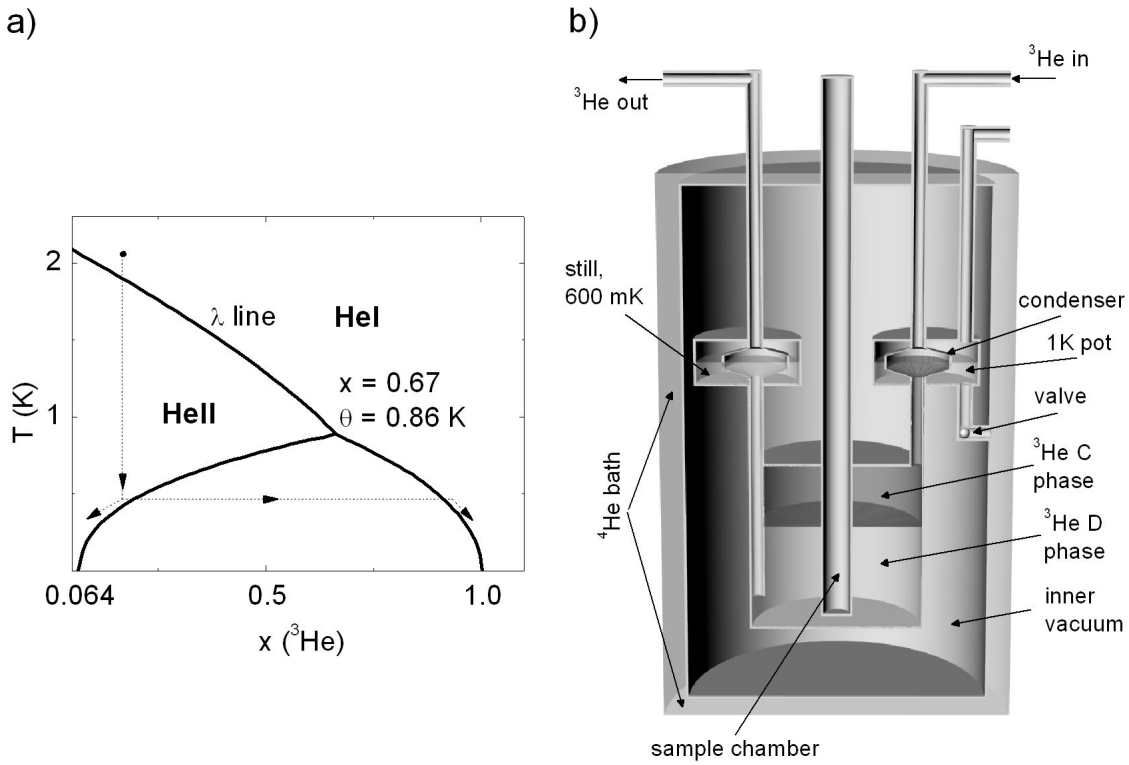

Fig. A.3: ***a)*** *Phase diagram of the ^{3}He/^{4}He mixture as a function of the ^{3}He concentration x and the temperature T. The λ line separates the two phases of ^{4}He, i.e., HeI (normal fluid) and HeII (Bose condensate). The tricritical point is at $x = 0.67$ and $T = 0.86$ K. At lower temperatures, the mixture separates into a so-called concentrated phase C (^{3}He-rich phase) and a diluted phase D (^{3}He-poor phase).* ***b)*** *Schematic sketch of a ^{3}He/^{4}He dilution refrigerator.*

^{3}He is kept in a closed cycle. The pumped ^{3}He gas is condensed in a pumped ^{4}He pot, which is connected to the ^{4}He bath via a needle valve. The temperature of the ^{4}He pot is kept below 3.18 K, which is the condensation temperature of ^{3}He.

A.2.3 ^{3}He/^{4}He dilution refrigerator

^{3}He/^{4}He dilution refrigerators make use of the unique properties of the ^{3}He/^{4}He mixture. The phase diagram of this mixture is shown in Fig. A.3 a), with the λ line separating the two phases of ^{4}He, i.e. HeI (normal fluid) and HeII (Bose condensate). Below the λ line at $T > 860$ mK, ^{3}He is dissolved in HeII as an additional component of the normal fluid HeII. For $T < 860$ mK the mixture undergoes a phase separation into the so-called *diluted phase* D (^{3}He–poor phase) and the *concentrated phase* C (^{3}He–rich phase). The D phase can be described as the ^{3}He vapour of the C phase, which has a significant vapour pressure even at very low temperature. As the C phase has a smaller density, the "liquid" (D) floats on top of the "gas" (C).

The essential parts of a ^{3}He/^{4}He cryostat are presented in Fig. A.3 b). The ^{3}He/^{4}He mixture rests in the *mixing chamber*. The D phase is connected via a tube to the *still*, which is heated to about 600 mK. At this temperature the vapour pressure of ^{3}He is much higher than that of ^{4}He, i.e. the ^{3}He is effectively distilled from the D phase. The missing ^{3}He in the D phase is delivered by "evaporation" of ^{3}He from the C phase, which leads to a cooling of the mixture in the mixing chamber. The evaporated ^{3}He is recondensed into the mixing chamber by a pot filled with ^{4}He which is pumped to temperatures below the condensation temperature of ^{3}He (*1 K pot*).

A.3 The SMW Hamiltonian in MATLAB

```
function EV

% by Johannes Schneider
% program to calculate the eigenvalues of the magnetic field SWM Hamiltonian
% see [Nakao, J. Phys. Soc. Japan, 40, 761 (1976)] for further details

% Implementation of parameters
% ------------------------------------------------
B = 5;          % Magnetic field value in T
gs = 2.5;       % value for g factor
sz = 50;        % the size of the SWM Hamiltonian corresponds to "sz*12"
                % factor 3: submatrix n; factor 4: each matrix D has the
                % size 4x4;
                % "sz = 50" corresponds to a 600x600 matrix

% Gamma parameters of SWM model in eV
g0 = 3.37;
g1 = 0.363;
g2 = -0.0243;
g3 = 0.31;
g4 = 0.07;
g5 = 0.05;
Delta = -0.007;

% kz values in units of c0/2Pi (at K point kz = 0; at H point kz = 0.5)
kmin = 0;
kmax = 0.5;
Deltak = 0.005; % step size of kz values


% kz values in units of c0/2Pi (at K point kz = 0; at H point kz = 0.5)
v  = 30;        % total number of eigenvalues for given submatrix n
nv = 10;        % number of Landau bands for a given submatrix n
                % the values of "v" and "nv" have to be increased for
                % B < 1.5 T
% ------------------------------------------------


% Constants
a0=2.46e-10;    % distance between carbon atoms in single graphite lattice
e=1.6e-19;      % elementary charge
h=1.055e-34;    % Planck constant
muB=5.789e-5;   % Bohr magneton
mu=muB/2*gs;
s=2*e*B/h;


```

```
% Implementation of the SWM-Hamiltonian
% ---------------------------------------------------

for n = -1:1:1  % n = -1 connects Landau bands (-1,2,5,8,...) etc.
                % selection rule n -> n+/-3
  dummyn = n;   % dummy variable for n
  dummyk = 0;   % dummy variable for k

 for k = kmin:Deltak:kmax  % kz
  dummyk = dummyk + 1;
  n = dummyn;

  l = 1; m = 1;            % Initialise SWM matrix: l = line, m = column

  % SWM variables depending on kz value
  Gamma = 2*cos(pi*k);
  gplus = -(g0+g4*Gamma);
  gmin  = -(g0-g4*Gamma);
  E1 = Delta + g1*Gamma + 0.5*g5*Gamma^2;
  E2 = Delta - g1*Gamma + 0.5*g5*Gamma^2;
  E3 = 0.5*g2*Gamma^2;
  % ---------------------------------------
  for j = 1:1:sz           % i und j are parameters in submatrix notation
   for i = 1:1:sz          % they correspond to lines and columns

   % Diagonal matrix elements: case for submatrices D0(n)
   if i == j
     if n == 0             % D0(0)
      E(l,m) = E1;
      E(l+1,m+1) = E2;
      E(l+3,m+3) = E3;

      E(l,m+3) = sqrt(6)/4*a0*gmin*sqrt((n+1)*s);
      E(l+1,m+3) = sqrt(6)/4*a0*gplus*sqrt((n+1)*s);
      E(l+3,m) = sqrt(6)/4*a0*gmin*sqrt((n+1)*s);
      E(l+3,m+1) = sqrt(6)/4*a0*gplus*sqrt((n+1)*s);


      m = m+4;             % column jump to the next submatrix

      elseif n == -1       % D0(-1)
       E(l+3,m+3) = E3;
       m = m+4;

      else                 % D0(n) with n ≥ 1
       E(l,m) = E1;
       E(l+1,m+1) = E2;
       E(l,m+2) = sqrt(6)/4*a0*gmin*sqrt(n*s);
       E(l+1,m+2) = -sqrt(6)/4*a0*gplus*sqrt(n*s);
       E(l,m+3) = sqrt(6)/4*a0*gmin*sqrt((n+1)*s);
       E(l+1,m+3) = sqrt(6)/4*a0*gplus*sqrt((n+1)*s);
```

```
99
100         E(l+2,m) = sqrt(6)/4*a0*gmin*sqrt(n*s);
101         E(l+3,m) = sqrt(6)/4*a0*gmin*sqrt((n+1)*s);
102         E(l+2,m+1) = -sqrt(6)/4*a0*gplus*sqrt(n*s);
103         E(l+3,m+1) = sqrt(6)/4*a0*gplus*sqrt((n+1)*s);
104         E(l+2,m+2) = E3;
105         E(l+3,m+3) = E3;
106
107         m = m+4;              % column jump to the next submatrix
108
109       end                     % end "if n = -1,0 or 1"
110
111
112       % Off-diagonal matrix elements: case for D1(n) and D1+(n)
113       elseif i == j+1         % D1(n)
114        E(l+3,m+2) = sqrt(3)/2*a0*g3*Gamma*sqrt((n+2)*s);
115
116        m = m+4;               % column jump to the next submatrix
117
118       elseif i == j-1         % D1+(n)
119        E(l+2,m+3) = sqrt(3)/2*a0*g3*Gamma*sqrt((n+2)*s);
120
121        m = m+4;               % column jump to the next submatrix
122        n = n+3;               % Initialisation of n finished; jump to n = n+3
123
124       else                    % other matrix elements are zero
125
126        m = m+4;               % column jump to the next submatrix
127
128       end                     % end "if i = j"
129     end                       % end "for i = 1:1:20"
130
131      m = 1; l = l+4;          % line jump to the next submatrix
132
133   end                         % end "for i = 1:1:20"
134
135   % ----------------------------------------
136
137   % CALCULATION of the eigenvalues
138      p = 0.01;               % eigenvalues calculated at around this energy
139
140      [D]= eigs(E,v,p);       % v eigenvalues of spare matrix in the vicinity
141                              % of the value p
142
143
144    % SORT eigenvalues in such a way that they are assigned
145    % to a given Landau band N
146
147    % 1) Sort eigenvalue vector so that norm(D(1)) ≤ norm(D(2)) ...,
148    %    i.e., D(v)=0;
149
```

```
150     for i = 1:v
151      for j = i+1:v
152       if norm(D(i)) < norm(D(j))
153        dummysort = D(j);
154        D(j) = D(i);
155        D(i) = dummysort;
156       end
157      end
158     end
159
160     %    for submatrix n, the "vv" last eigenvalues of the sorted
161     %    eigenvector are zero and have therefore to be removed
162     if dummyn == -1
163      vv = 3; end
164     if dummyn == 0
165      vv = 1; end
166     if dummyn == 1
167      vv = 0; end
168
169     % 2) Assign eigenvalue to Landau bands
170     for tt = 1:1:nv+1       % tt is dummy variable
171
172      for ii = 1:1:v-vv      % get rid of the eigenvalues "0"
173       y(ii,dummyk) = D(ii); % new eigenvector y
174      end
175
176      for i = 1:v-3          % sort in ascending order
177       for j = i+1:v-vv
178        if y(i,dummyk) < y(j,dummyk)
179         dummysort = y(j,dummyk);
180         y(j,dummyk) = y(i,dummyk);
181         y(i,dummyk) = dummysort;
182        end
183       end
184      end
185
186
187      % eigenvalue vector at K point (kz = 0)
188      if dummyk == 1
189       nn = 0;               % eigenvalue number
190       for jj = 1:v-vv
191        if y(jj,dummyk) ≤ 0 && nn ≤ nv
192         nn = nn + 1;
193
194         if dummyn == -1
195          LLm1(nn,dummyk) = y(jj,dummyk);
196         end
197
198         if dummyn == 0
199          LL0(nn,dummyk) = y(jj,dummyk);
200         end
```

```
201
202         if dummyn == 1
203          LL1(nn,dummyk) = y(jj,dummyk);
204         end
205
206        end
207       end
208      end
209
210      % eigenvalue vector away from K point (kz neq 0)
211      if dummyk > 1
212       diff = 5;              % eigenvalue number is found through
213       for jj = 1:v-vv        % smallest energy difference
214
215        if dummyn == -1
216         difftest = norm(LLm1(tt,dummyk-1) - y(jj,dummyk));
217         if difftest < diff
218          diff = difftest;
219          LLm1(tt,dummyk) = y(jj,dummyk);
220         end
221        end
222
223        if dummyn == 0
224         difftest = norm(LL0(tt,dummyk-1) - y(jj,dummyk));
225         if difftest < diff
226          diff = difftest;
227          LL0(tt,dummyk) = y(jj,dummyk);
228         end
229        end
230
231        if dummyn == 1
232         difftest = norm(LL1(tt,dummyk-1) - y(jj,dummyk));
233         if difftest < diff
234          diff = difftest;
235          LL1(tt,dummyk) = y(jj,dummyk);
236         end
237        end
238
239       end
240      end
241     end
242
243   end                          % end "for k = kmin:Deltak:kmax+Deltak"
244  end                           % end "for n = -1:1:1"
245
246
247
248  % PLOT eigenvalues in meV including spin splitting
249  k = kmin:Deltak:kmax;
250  plot(k,(LLm1(:,:)+mu*B)*1000,'-r')
251  hold on
```

```
252 plot(k,(LLm1(:,:)-mu*B)*1000,'-r')
253 hold on
254
255 plot(k,(LL0(:,:)+mu*B)*1000,'-g')
256 hold on
257 plot(k,(LL0(:,:)-mu*B)*1000,'-g')
258 hold on
259
260 plot(k,(LL1(:,:)+mu*B)*1000,'-b')
261 hold on
262 plot(k,(LL1(:,:)-mu*B)*1000,'-b')
263 hold on
264
265 set(gcf,'color','white')
266 xlabel('k_z')
267 ylabel('E (meV)')
268 axis([0,0.5,-55,3])
269 hold off;
270
271 % ----------------------------------------
```

Bibliography

[1] J. BERNAL, *Proc. R. Soc. London A* **106**, 749 (1924).

[2] J. SLONCZEWSKI and P. WEISS, *Phys. Rev.* **109**, 272 (1958).

[3] J. W. MCCLURE, *Phys. Rev.* **108**, 612 (1957).

[4] R. S. H.-P. BOEHM and E. STUMPP, *Pure & Appl. Chem.* **66**, 1893 (1994).

[5] K. S. NOVOSELOV and A. K. GEIM, *Nature* **438**, 197 (2005).

[6] L. D. LANDAU, *Z. Phys.* **64**, 629 (1930).

[7] I. M. LIFSHITZ and A. M. KOSEVICH, *Sov. Phys. JETP* **2**, 636 (1956).

[8] E. N. ADAMS and T. D. HOLSTEIN, *J. Phys. Chem. Solids* **10**, 254 (1959).

[9] D. SOULE, J. MCCLURE, and L. SMITH, *Physical Review* **134**, A453 (1964).

[10] J. A. WOOLLAM, *Phys. Rev. Lett.* **25**, 810 (1970).

[11] J. A. WOOLLAM, *Phys. Rev. B* **3**, 1148 (1971).

[12] Y. IYE and G. DRESSELHAUS, *Phys. Rev. Lett.* **54**, 1182 (1985).

[13] S. WILLIAMSON, S. FONER, and M. DRESSELHAUS, *Phys. Rev.* **140**, A1429 (1965).

[14] P. R. SCHROEDER, M. S. DRESSELHAUS, and A. JAVAN, *Phys. Rev. Lett.* **20**, 1292 (1968).

[15] W. W. TOY, M. S. DRESSELHAUS, and G. DRESSELHAUS, *Phys. Rev. B* **15**, 4077 (1977).

[16] J. K. GALT, W. A. YAGER, and J. H. W. DAIL, *Phys. Rev.* **103**, 1586 (1956).

[17] H. SUEMATSU, K. HIGUCHI, and S. TANUMA, *J. Phys. Soc. Jpn.* **48**, 1541 (1980).

[18] Z. ZHU, H. YANG, B. FAUQUÉ, Y. KOPELEVICH, and K. BEHNIA, *Nature Physics* **6**, 26 (2009).

[19] R. E. FRANKLIN, *Acta Crystallogr.* **4**, 253 (1951).

[20] P. WALLACE, *Phys. Rev.* **71**, 622 (1947).

[21] M. ORLITA, C. FAUGERAS, J. M. SCHNEIDER, G. MARTINEZ, D. K. MAUDE, and M. POTEMSKI, *Phys. Rev. Lett.* **102**, 166401 (2009).

[22] G. P. MIKITIK and Y. V. SHARLAI, *Phys. Rev. B* **73**, 235112 (2006).

[23] J. W. MCCLURE, *Phys. Rev.* **119**, 606 (1960).

[24] M. INOUE, *J. Phys. Soc. Japan* **17**, 808 (1962).

[25] Y. KOPELEVICH, V. V. LEMANOV, S. MOEHLECKE, and J. H. S. TORRES, *Phys. Solid State* **41**, 1959 (1999).

[26] S. TANUMA, R. INADA, A. FURUKAWA, O. TAKAHASJI, and Y. IYE, in *Proceedings in high magnetic fields: proceedings of the Oji International Seminar, Hakone, Japan*, 1981.

[27] H. YAGUCHI and J. SINGLETON, *J. Phys.: Condens. Matter* **21**, 344207 (2009).

[28] N. BRANDT, S. CHUDINOV, and Y. G. PONOMAREV, *SEMIMETALS, 1. Graphite and its compounds*, North-Holland, 1988.

[29] H. W. KROTO, J. R. HEATH, S. C. O'BRIEN, R. F. CURL, and R. E. SMALLEY, *Nature* **318**, 162 (1985).

[30] S. IIJIMA, *Nature* **354**, 56 (1991).

[31] R. PEIERLS, *Quelques propriétés typiques des corpses solides*, Gauthier-Villars, 1935.

[32] S. Y. ZHOU, G.-H. GWEON, J. GRAF, A. V. FEDOROV, C. D. SPATARU, R. D. DIEHL, Y. KOPELEVICH, D.-H. LEE, S. G. LOUIE, and A. LANZARA, *Nature physics* **2**, 595 (2006).

[33] M. ORLITA, C. FAUGERAS, G. MARTINEZ, D. K. MAUDE, M. L. SADOWSKI, J. M. SCHNEIDER, and M. POTEMSKI, *J. Phys.: Condens. Matter* **20**, 454223 (2008).

[34] W. J. DE HAAS and P. M. VAN ALPHEN, *Proc. Netherlands Roy. Acad. Sci.* **33**, 1106 (1930).

[35] L. W. SHUBNIKOV and W. J. DE HAAS, *Proc. Netherlands Roy. Acad. Sci.* **33**, 130 and 160 (1930).

[36] L. ONSAGER, *Phil. Mag. Ser. 7* **43**, 1006 (1952).

[37] K. MATSUBARA, T. TSUZUKU, and K. SUGIHARA, *Phys. Rev. B* **44**, 11845 (1991).

[38] D. L. HUBER, R. R. URBANO, M. S. SERCHELI, and C. RETTORI, *Phys. Rev. B* **70**, 125417 (2004).

[39] J. F. JANEK, *Phys. Rev.* **178**, 1416 (1969).

[40] T. ANDO and Y. UEMURA, *J. Phys. Soc. Japan* **37**, 1044 (1974).

[41] ASHCROFT/MERMIN, *Solid State Physics*, Saunders-College, 1976.

[42] D. SHOENBERG, *Magnetic oscillations in graphite*, Cambridge University Press, 1984.

[43] A. PIPPARD, *The Dynamics of Conduction Electrons*, Blackie and son, Glasgow, 1965.

[44] B. I. HALPERIN, *Phys. Rev. B* **25**, 2185 (1982).

[45] H. AOKI and H. KAMIMURA, *Solid State Commun.* **21**, 45 (1977).

[46] C. BERGER, Z. SONG, X. LI, X. WU, N. BROWN, C. NAUD, D. MAYOU, T. LI, J. HASS, A. N. MARCHENKOV, E. H. CONRAD, P. N. FIRST, and W. A. DE HEER, *Science* **312**, 1191 (2006).

[47] R. SAITO, M. DRESSELHAUS, and G. DRESSELHAUS, *Physical Properties of carbon nanotubes*, Imperial College Press, 1998.

[48] G. DRESSELHAUS, *Phys. Rev. B* **10**, 3602 (1974).

[49] G. P. MIKITIK and Y. V. SHARLAI, *Phys. Rev. Lett.* **82**, 2147 (1999).

[50] G. DRESSELHAUS and M. S. DRESSELHAUS, *Phys. Rev.* **140**, A401 (1965).

[51] P. NOZIÈRES, *Phys. Rev.* **109**, 1510 (1958).

[52] K. NAKAO, *J. Phys. Soc. Japan* **40**, 761 (1976).

[53] Y. LATYSHEV, Z. KOSAKOVSKAYA, A. ORLOV1, A. LATYSHEV, V. KOLESOV, P. MONCEAU, and D. VIGNOLLES, *Journal of Physics: Conference Series* **129**, 012032 (2008).

[54] F. BITTER, *Rev. of Sci. Instr.* , 482 (1936).

[55] M. WOOD, *High Magnetic Fields*, p. 387, M.I.T. Press and Johan Wiley and Sons, New York, 1962.

[56] G. AUBERT, F. DEBRAY, W. JOSS, H. JONGBLOETS, and M. OHL, *IEEE Transactions on Applied Superconductivity* **10**, 455 (2000).

[57] D. E. SOULE, *Phys. Rev.* **112**, 698 (1958).

[58] G. TIMP, P. DRESSELHAUS, T. CHIEU, G. DRESSELHAUS, and Y. IYE, *Phys. Rev. B* **28**, 7393 (1983).

[59] I. A. LUK'YANCHUK and Y. KOPELEVICH, *Phys. Rev. Lett.* **97**, 256801 (2006).

[60] A. A. ABRIKOSOV, *Phys. Rev. B* **60**, 4231 (1999).

[61] T. TOKUMOTU, E. JOBILIONG, E. S. CHOI, Y. OSHIMA, and J. S. BROOKS, *Solid State Commun.* **129**, 599 (2004).

[62] X. DU, S.-W. TSAI, D. L. MASLOV, and A. F. HEBARD, *Phys. Rev. Lett.* **94**, 166601 (2005).

[63] J. GONZÁLES, M. MUÑOZ, N. GARCIA, J. BARZOLA-QUIQUIA, D. SPODDIG, K. SCHINDLER, and P. ESQUINAZI, *Phys. Rev. Lett.* **99**, 216601 (2007).

[64] Y. K. H. KEMPA, P. ESQUINAZI, *Solid State Commun.* **138**, 118 (2006).

[65] S. B. HUBBARD, T. J. KERSHAW, A. USHER, A. K. SAVCHENKO, and A. SHYTOV, *arXiv:1007.2573v1* (2010).

[66] J. W. MCCLURE, *Phys. Rev.* **112**, 715 (1958).

[67] Y. KOPELEVICH, J. H. S. TORRES, R. R. DA SILVA, F. MROWKA, H. KEMPA, and P. ESQUINAZI, *Phys. Rev. Lett.* **90**, 156402 (2003).

[68] D. V. KHVESHCHENKO, *Phys. Rev. Lett.* **87**, 206401 (2001).

[69] E. V. GORBAR, V. P. GUSYNIN, V. A. MIRANSKY, and I. A. SHOVKOVY, *Phys. Rev. B* **66**, 045108 (2002).

[70] I. V. T. MANIV, V. ZHURAVLEV and P. WYDER, *Rev. Mod. Phys.* **73**, 867 (2001).

[71] Y. ZHENG and T. ANDO, *Phys. Rev. B* **65**, 245420 (2002).

[72] J. M. SCHNEIDER, N. A. GONCHARUK, P. VAŠEK, P. SVOBODA, Z. VÝBORNÝ, L. SMRČKA, M. ORLITA, M. POTEMSKI, and D. K. MAUDE, *Phys. Rev. B* **81**, 195204 (2010).

[73] I. A. LUK'YANCHUK and Y. KOPELEVICH, *Phys. Rev. Lett.* **93**, 166402 (2004).

[74] K. SUGIHARA and S. ONO, *J. Phys. Soc. Jpn.* **21**, 631 (1966).

[75] L. D. LANDAU, L. P. PITAEVSKII, and E. LIFSHITZ, *Electrodynamics of Continuous Media*, Butterworth-Heinemann, 1984.

[76] M. KOSHINO and T. ANDO, *Phys. Rev. B* **76**, 085425 (2007).

[77] I. A. LUK'YANCHUK, Y. KOPELEVICH, and M. E. MARSSI, *Physica B: Condensed Matter* **404**, 404 (2009).

[78] J. M. SCHNEIDER, M. ORLITA, M. POTEMSKI, and D. K. MAUDE, *Phys. Rev. Lett.* **102**, 166403 (2009).

[79] I. A. LUK'YANCHUK and Y. KOPELEVICH, *Phys. Rev. Lett.* **104**, 119701 (2010).

[80] J. M. SCHNEIDER, M. ORLITA, M. POTEMSKI, and D. K. MAUDE, *Phys. Rev. Lett.* **104**, 119702 (2010).

[81] D. E. SOULE, *IBM J. Res. Develop* **8**, 268 (1964).

[82] J. R. ANDERSON, W. J. O'SULLIVAN, J. E. SCHIRBER, and D. E. SOULE, *Phys. Rev.* **164**, 1038 (1967).

[83] J. A. WOOLLAM, *Phys. Rev. B* **4**, 3393 (1971).

[84] G. WAGONER, *Phys. Rev.* **118**, 647 (1960).

[85] K. KAWAMURA, S. KANEKO, and T. TSUZUKU, *J. Phys. Soc. Japan* **52**, 3936 (1983).

[86] C. KALLIN and B. I. HALPERIN, *Phys. Rev. B* **30**, 5655 (1984).

[87] Y. IYE, P. M.TEDROW, G. TIMP, M. SHAYYEGAN, M. S. DRESSELHAUS, G. DRESSELHAUS, A. FURUKAWA, and S. TANUMA, *Phys. Rev. B* **25**, 5478 (1982).

[88] K. NAKAMURA, T. OSADA, G. KIDO, N. MIURA, and S. TANUMA, *J. Phys. Soc. Japan* **52**, 2875 (1983).

[89] Y. IYE, P. M. BERGLUND, and L. E. MCNEIL, *Solid State Commun.* **52**, 975 (1984).

[90] H. YAGUCHI and J. SINGLETON, *Phys. Rev. Lett.* **81**, 5193 (1998).

[91] S. YOSHIOKA and H. FUKUYAMA, *J. Phys. Soc. Japan* **50**, 725 (1981).

[92] G. GRÜNER, *Rev. Mod. Phys.* **60**, 1129 (1988).

[93] H. KEMPA, H. C. SEMMELHACK, P. ESQUINAZI, and Y. KOPELEVICH, *Solid State Commun.* **125**, 1 (2003).

[94] D. J. FLOOD, *Phys. Lett. A* **30**, 178 (1969).

[95] S. B. AUSTERMANN, Growth of graphite crystals from solution, in *Chemistry and Physics of Carbon*, 1968.

[96] T. MATSUI, H. KAMBARA, Y. NIIMI, K. TAGAMI, M. TSUKADA, and H. FUKUYAMA, *Phys. Rev. Lett.* **94**, 226403 (2005).

[97] R. PEIERLS, *More Surprises in Theoretical Physics*, Princeton University Press, 1991.

[98] G. CHOUTEAU and A. BRIGGS, *Solid State Commun.* **21**, 785 (1977).

[99] J. T. NICHOLLS, E. J. MCNIFF, and G. DRESSELHAUS, *Phys. Rev. B* **42**, 5555 (1990).

[100] F. SEITZ, *The modern theory of solids*, Dover Publications, 1987.

[101] Y. ZHANG, J. P. SMALL, M. E. S. AMORI, and P. KIM, *Phys. Rev.* **94**, 176803 (2005).

[102] G. LI and E. Y. ANDREI, *Nature Physics* **3**, 623 (2007).

[103] J. W. MCCLURE, *Phys. Rev.* **104**, 666 (1956).

[104] T. J. KERSHAW, *Millikelvin Magnetisation studies of Low Dimensional Systems*, PhD thesis, University of Exeter, 2008.

List of publications

Work presented in this thesis:

J. M. Schneider, M. Orlita, M. Potemski, and D. K. Maude
Consistent Interpretation of the Low-Temperature Magnetotransport in Graphite Using the Slonczewski-Weiss-McClure 3D Band-Structure Calculations
Phys. Rev. Letters, **102**, 166403, 2009

J. M. Schneider, M. Orlita, M. Potemski, and D. K. Maude
Reply to Comment on "Consistent Interpretation of the Low-Temperature Magnetotransport in Graphite Using the Slonczewski-Weiss-McClure 3D Band-Structure Calculations"
Phys. Rev. Letters, **104**, 119702, 2010

J. M. Schneider, N. A. Goncharuk, P. Vašek, P. Svoboda, Z. Výborný, L. Smrčka, M. Orlita, M. Potemski, and D. K. Maude
Using magnetotransport to extract the spin gap for charged excitations in graphite
Phys. Rev. B, **81**, 195204, 2010

Other work:

M. Orlita, C. Faugeras, G. Martinez, D. K. Maude, M. L. Sadowski, **J. M. Schneider** and M. Potemski
Magneto-transmission as a probe of Dirac fermions in bulk graphite
J. Phys.: Condens. Matter, **20**, 454223, 2008

P. Plochocka, **J. M. Schneider**, D.K. Maude, M. Potemski, M. Rappaport, V. Umansky, I. Bar-Joseph, J. G. Groshaus, Y. Gallais, A. Pinczuk
Optical Absorption to Probe the Quantum Hall Ferromagnet at Filling Factor $\nu = 1$
Phys. Rev. Letters, **102**, 126806, 2009

M. Orlita, C. Faugeras, **J. M. Schneider**, G. Martinez, D. K. Maude, and M. Potemski
Graphite from the Viewpoint of Landau Level Spectroscopy: An Effective Graphene Bilayer and Monolayer
Phys. Rev. Letters, **102**, 166401, 2009

Conferences and workshops attended:

29th International Conference on the Physics of Semiconductors (**ICPS**),
Rio de Janeiro - Brazil, Jul 27 - Aug 1, 2008
Contributed oral presentation:
Magnetotransport in graphite: Evidence for a 2D or 3D system?

18th International Conference on High Magnetic Fields in Semiconductor
Physics and Nanotechnology (**HMF18**),
São Pedro - Brazil, Aug 3 - Aug 8, 2008
Contributed oral presentation:
High field magnetotransport in graphite

ICTP Conference: Graphene Week 2008
Trieste - Italy, Aug 25 - Aug 29, 2008
Poster presentation:
Magnetotransport in graphite

LCMI workshop: Semiconductor and carbon based nanostructures in magnetic fields
Grenoble - France, Nov 24 - Nov 26, 2008
Contributed oral presentation:
Magnetotransport in graphite: Evidence for a 3D system?

XXXVIII International School & Conference on the Physics of Semiconductors,
"Jaszowiec" 2009
Krynica - Poland, Jun 19 - Jun 26, 2009
Contributed oral presentation:
Low temperature magnetotransport in graphite interpreted using the Slonczewski–Weiss–McClure band structure calculations

18th International Conference on Electronic Properties of Two-Dimensional Systems (**EP2DS**),
Kobe - Japan, Jul 19 - Jul 24, 2009
Poster presentation:
Magnetotransport in graphite

XXXIX International School & Conference on the Physics of Semiconductors,
"Jaszowiec" 2010
Krynica - Poland, Jun 19 - Jun 24, 2010
Poster presentation:
Using magnetotransport to determine the spin splitting in graphite

Acknowledgment

Finally - hidden on the last pages of my thesis - the acknowledgment. The time you arrive here, you have probably read the whole thesis with high interest... Here are the people I want to thank:

To begin with I would like to thank *Thierry Ouisse* for accepting being the president of my jury. I also would like to thank the two "rapporteurs", *Kamran Behnia* and *Laurence Eaves*, for their evaluation of my thesis, for their comments and for creating a friendly and relaxed atmosphere at the day of my soutenance. The same goes for *Piotr Kossacki* in his function as "examinateur". Dziękuję, Piotr!

I also would like to thank the director of the Laboratoire National des Champs Magnétiques Intenses (LNCMI) in Grenoble, *Geert Rikken*, his predecessor *Jean-Louis Tholence* and the vice-director *Claude Berthier*.

The prominent part of my acknowledgment is devoted to the supervisor of my thesis, *Duncan Maude*. Thank you for offering me the opportunity to make my PhD at the Grenoble High Magnetic Field Laboratory! The initial proposal was to study the "relativistic charge carriers of graphene". This did not quite work out, since our collaborators - no names revealed here ;) - could not provide us with working graphene samples. Instead we studied "stacked graphene", which is also known as graphite. The work on graphite turned out to be really fascinating. It was spiced up by our colleagues *Igor Luk'yanchuk* and *Yakov Kopelevich* who have a little different viewpoint of graphite and explained the discrepancy by our "improper treatment of experimental results" [79]. Many thanks!
Anyhow... I am not sure if a PhD project on graphene would have been as successful as the one presented here. Danke schön, Duncan, for the support, for your patience in many occasions, for the discussion of various physical problems and sending me abroad to conferences.

I also want to thank sincerely *Marek Potemski* for his great interest in my work and the many discussions we had! I especially remember the evening(!) discussions at ICPS 2008 in Rio de Janeiro (best thing to do there!). This was around the time when we had for the first time the extremely rich low temperature data and did not know how to interpret them. A few weeks later we knew better.

I would like to thank *Milan Orlita*, with whom I shared the office for three years, for his help and inspiring discussions (including eye-opening discussions of the Czech Republic, the "heart of Europe")! At this point thanks to the whole Czech team! Děkuju Vám! Making a Czech list of all its members would be too exhaustive. So, apart from Milan, here are its most prominent members: *Aleš Hrabec*, *Jan Kunc* and *Petr Neugebauer*. Thank you also to the members of the German, Spanish, Polish and French teams, *Matthias Kuhne*, *Steffen Wiedmann*, *Mario Amado*,

Mateusz Goryca, *Przemyslaw Leszczynski*, *Paulina Plochocka* and *Clément Faugeras*.

Many thanks to *Benjamin Piot* and *Ilya Sheikin*, especially for helping me with the de Haas-van Alphen measurements.

I would also like to express many thanks to *Rachel Graziotti*, *Amélie Pic*, *Elisabeth Rochat* and *Cécile Vannier* for solving all my administrative problems, *Sébastien Buisson* and *Thomas Dolmazon* for solving computer problems and the engineers and technicians who were involved in this project.

Thanks to all my colleagues and friends from this lab, in Grenoble and all over the world! I especially would like to thank *Danny Hykel* with whom I studied in Karlsruhe and in France ("ENSPG is like war") and who also ended up making his PhD at CNRS Grenoble, and *Marcelos Peres* who stayed here as a postdoc for one year and became a very good friend since.

I finally want to thank my family for their support. Unfortunately they did not see me a lot in the last few years. Special thanks to my "little" brother Nils to whom this thesis is dedicated! Our mountaineering vacations in the Swiss Alps will always remain in my memories...Nils, I admire your warm-hearted nature, endurance, courage, enthusiasm, and incredible calmness![1]

---

[1] Nils, I would like to see your reaction when you read this for the first time: "Johannes, musste das jetzt echt sein?" :)

“Your mark in this solid state physics exam shows that you do not understand physics.”

Comment to the author of this thesis in a serious conversation with a professor about his “dark” future. The author got 8/20 in a physique du solide exam and barely spoke French.

Abstract

In this thesis, low-temperature magnetotransport ($T \approx 10$ mK) and the de Haas-van Alphen effect of both natural graphite and highly oriented pyrolytic graphite (HOPG) are examined. In the first part, low field magnetotransport up to $B = 11$ T is discussed. A Fourier analysis of the background removed signal shows that the electric transport in graphite is governed by two types of charge carriers, electrons and holes. Their phase and frequency values are in agreement with the predictions of the SWM-model. The SWM-model is confirmed by detailed bandstructure calculations using the magnetic field Hamiltonian of graphite. The movement of the Fermi at $B >$ 2 T is calculated self-consistently assuming that the sum of the electron and hole concentrations is constant.

The second part of the thesis deals with high field magnetotransport of natural graphite in the magnetic field range $0 \leq B \leq 28$ T. Both *spin splitting* of magnetotransport features in tilted field configuration and the onset of the *charge density wave (CDW)* phase for different temperatures with the magnetic field applied normal to the sample plane are discussed. Concerning the Zeeman effect, the SWM calculations including the Fermi energy movement require a g-factor of $g^* = 2.5 \pm 0.1$ to reproduce the spin spilt features. The measurements of the charge density wave state confirm that its onset magnetic field can be described by a Bardeen-Cooper-Schrieffer (BCS)-type formula. The measurements of the de Haas-van Alphen effect are in agreement with the results of the magnetotransport measurements at low field.

Key words: graphite, magnetotransport, SdH effect, dHvA effect, SWM-model

Résumé

Dans cette thèse, le magnétotransport à basse température ($T \approx 10$ mK) et l'effet de Haas-van Alphen sont examinés pour le graphite naturel et le graphite HOPG. Dans la première partie, le magnétotransport pour des champs magnétiques allant jusqu'à $B = 11$ T est présenté. Une analyse de Fourier de ΔR_{xx} (signal après soustraction du fond de magnétorésistance) montre que le transport électrique dans le graphite est dominé par deux types de porteurs avec des fréquences et des phases en accord avec le modèle SWM. Nous confirmons la validité du modèle SWM par des calculs détaillés de la structure de bande sous champ magnétique. Le mouvement de l'énergie de Fermi pour $B > 2$ T est calculé d'une manière auto-cohérente en supposant que la somme des concentrations des électrons et des trous est constante.

Des mesures sous champs magnétiques intenses ($0 \leq B \leq 28$ T) sont employées pour étudier l'effet Zeeman et la phase de l'onde de densité de charge. En ce qui concerne l'effet Zeeman, les calculs SWM incluant le mouvement de l'énergie de Fermi nécessitent un facteur de Lande $g^* = 2.5 \pm 0.1$ pour reproduire la séparation de spin observée dans les données. Les mesures de l'onde de densité de charge confirment que le champ magnétique auquel celle-ci apparait est lié à la température par une formule de type Bardeen-Cooper-Schrieffer (BCS). Les mesures de l'effet de Haas-van Alphen sont en accord avec les résultats obtenus par de magnétotransport à bas champ.

Mots clés: graphite, magnétotransport, effet SdH, effet dHvA, modèle SWM